THE UNIVERSITY OF QUEENSLAND

AUSTRALIA

Quantum Measurement and Control of a Mechanical Parametric Oscillator

Alex Szorkovszky

B.Sc (Hons)

A thesis submitted for the degree of Doctor of Philosophy at

The University of Queensland in 2014

School of Mathematics and Physics

Abstract

Unlike classical systems, the very act of observing quantum systems perturbs their behaviour. This introduces "backaction noise", which imposes limits on the knowledge that can be obtained through measurement. Certain measurement techniques, known generally as quantum non-demolition (QND) measurements, exist to circumvent this noise. An alternative method to evade backaction noise is to amplify the observable of interest above the noise. However, this generally leaves the system in a different state, and is therefore not considered a QND measurement. In this thesis, I examine the benefits of amplification for various kinds of measurement of mechanical harmonic oscillators which, at the micrometre and nanometre scale, comprise an emerging quantum technology. For this prototypical case, modulation of the spring constant, also known as parametric amplification, is a well-studied noiseless amplification technique. Using the theory of trajectories developed in the field of quantum optics, I show that a weak measurement combined with a detuned parametric drive achieves the same ends as strong QND measurement. Namely, it allows backaction-free observation of one quadrature of mechanical motion, and through this, quantum squeezing below the quantum zero-point motion. This equivalence is experimentally confirmed in the classical limit using an optically detected, electrically modulated cantilever. In addition, I analyse similar amplification enhanced techniques for quantum entanglement and quantum tomography. These results are applicable to research in quantum optomechanics and electromechanics, and can be translated to other kinds of quantum harmonic oscillators, such as microwave cavities.

Declaration by author

This thesis is composed of my original work, and contains no material previously published or written by another person except where due reference has been made in the text. I have clearly stated the contribution by others to jointly-authored works that I have included in my thesis.

I have clearly stated the contribution of others to my thesis as a whole, including statistical assistance, survey design, data analysis, significant technical procedures, professional editorial advice, and any other original research work used or reported in my thesis. The content of my thesis is the result of work I have carried out since the commencement of my research higher degree candidature and does not include a substantial part of work that has been submitted to qualify for the award of any other degree or diploma in any university or other tertiary institution. I have clearly stated which parts of my thesis, if any, have been submitted to qualify for another award.

I acknowledge that an electronic copy of my thesis must be lodged with the University Library and, subject to the General Award Rules of The University of Queensland, immediately made available for research and study in accordance with the Copyright Act 1968.

I acknowledge that copyright of all material contained in my thesis resides with the copyright holder(s) of that material. Where appropriate I have obtained copyright permission from the copyright holder to reproduce material in this thesis.

Publications during candidature

1. A. Szorkovszky, G.I. Harris, A.C. Doherty and W.P. Bowen. Mechanical squeezing via parametric amplification and weak measurement. *Physical Review Letters*, **107**, 213603 (2011).

2. M.A. Taylor, A. Szorkovszky, J. Knittel, K.H. Lee, T.G. McRae and W.P. Bowen. Cavity optoelectromechanical regenerative amplification. *Optics Express*, **20**, 12742 (2012).

3. S. Forstner, S. Prams, J. Knittel, E.D. van Ooijen, J.D. Swaim, G.I. Harris, A. Szorkovszky, W.P. Bowen and H. Rubinsztein–Dunlop. Cavity optomechanical magnetometer. *Physical Review Letters*, **108**, 120801 (2012).

4. A.C. Doherty, A. Szorkovszky, G.I. Harris and W.P. Bowen. The quantum trajectory approach to quantum feedback control of an oscillator revisited. *Philosophical Transactions of the Royal Society A*, **370**, 5338–5353 (2012).

5. A. Szorkovszky, G.I. Harris, A.C. Doherty and W.P. Bowen. Position estimation of a parametrically driven optomechanical system. *New Journal of Physics*, **14**, 095026 (2012).

6. A. Szorkovszky, G.A. Brawley, A.C. Doherty and W.P. Bowen. Strong thermomechanical squeezing via weak measurement. *Physical Review Letters*, **110**, 184301 (2013).

7. A. Szorkovszky, A.A. Clerk, A.C. Doherty and W.P. Bowen. Detuned mechanical parametric amplification as a quantum non-demolition measurement. *New Journal of Physics*, **16**, 043023 (2014).

8. A. Szorkovszky, A.A. Clerk, A.C. Doherty and W.P. Bowen. Mechanical entanglement via detuned parametric amplification. *New Journal of Physics*, **16**, 063043 (2014).

Publications included in this thesis

Mechanical squeezing via parametric amplification and weak measurement. Incorporated as Figures 4.1 and 6.3.

Contributor	Contribution
Alex Szorkovszky	Derived results (100%), performed simulations (100%), wrote the paper (100%)
Glen Harris	Provided analysis (25%)
Andrew Doherty	Provided analysis (75%), edited the paper (30%)
Warwick Bowen	Edited the paper (70%)

The quantum trajectory approach to quantum feedback control of an oscillator revisited. Incorporated as Sections 3.2, 3.4 and 3.5.

Contributor	Contribution
Alex Szorkovszky	Provided analysis (25%)
Andrew Doherty	Derived results (100%), wrote the paper (100%)
Glen Harris	Provided analysis (25%)
Warwick Bowen	Provided analysis (50%), edited the paper (100%)

Position estimation of a parametrically driven optomechanical system. Incorporated as Chapter 4, Section 6.2 and Section 6.4.

Contributor	Contribution
Alex Szorkovszky	Derived results (100%), performed simulations (100%), wrote the paper (100%)
Glen Harris	Provided analysis (25%)
Andrew Doherty	Provided analysis (75%), edited the paper (30%)
Warwick Bowen	Edited the paper (70%)

Strong thermomechanical squeezing via weak measurement. Incorporated as Chapter 5.

Contributor	Contribution
Alex Szorkovszky	Performed the experiment (70%), analysed the data (70%), wrote the paper (100%)
George Brawley	Set up the experiment (100%), performed the experiment (30%), analysed the data (30%), created Figure 5.2
Andrew Doherty	Provided analysis (40%)
Warwick Bowen	Provided analysis (60%), edited the paper (100%)

Detuned mechanical parametric amplification as a quantum non-demolition measurement. Incorporated as Section 4.4.1 and Section 6.3.

Contributor	Contribution
Alex Szorkovszky	Derived results (50%), wrote the paper (80%)
Aashish Clerk	Derived results (50%), wrote the paper (20%)
Andrew Doherty	Provided analysis (100%)
Warwick Bowen	Edited the paper (100%)

Mechanical entanglement via detuned parametric amplification. Incorporated as Chapter 7.

Contributor	Contribution
Alex Szorkovszky	Derived results (100%), wrote the paper (100%)
Aashish Clerk	Provided analysis (40%), edited the paper (20%)
Andrew Doherty	Provided analysis (20%)
Warwick Bowen	Provided analysis (40%), edited the paper (80%)

Contributions by others to this thesis

Michael Taylor rendered the 3D schematic in Figure 5.1.

Statement of parts of the thesis submitted to qualify for the award of another degree

None.

Acknowledgements

It is difficult to imagine the things one can do unaided. I would not have thought myself capable of producing a PhD thesis, but I believe few people are inherently capable of such things on their own. Thus the great tradition of the thesis acknowledgement must be upheld. Sleep deprivation and the fact that it is the last hour of Friday afternoon will detract from my coherence, but what better time and state of mind is there for it?

Firstly and with utmost gratitude I would like to thank my principal advisor Warwick Bowen. I could not imagine a more hard-working, considerate, responsible and kind supervisor. Working with him — never in the past four years did it really feel like I was working *under* him — has been only a pleasure, despite all of the times I have been less than pleasant. I feel lucky to have had him as a mentor and friend, and I hope this can continue regardless of where my career takes me. His boundless enthusiasm for his work and mine has never wavered through all of the times that mine has, which is nothing but inspiring.

I must also thank my secondary advisor Andrew Doherty. While the limitations of interstate video conferencing (and daylight savings) have not allowed a similar level of contact, Andrew has been an overwhelmingly patient and accommodating supervisor. Over time, I have humbly come to appreciate the depth and breadth of knowledge that separates his intuition from my guess-work. I owe gratitude also to Aashish Clerk for his interest in my work and his admirable willingness to collaborate with an unknown PhD student. I would also like to thank Joe Kerckhoff for his many helpful comments, corrections and suggestions in regards to this thesis.

My thanks also go out to the entire Queensland Quantum Optics group. To Glen Harris for showing me the ropes in the lab and being a top-notch travelling partner. To George Brawley for his inspiring dedication to quality, and for being good company in the office during the rare times that our sleeping patterns overlapped. Special mentions to Stefan Forstner and Jon Swaim — wherever in the world their adventures have led them to.

Much love is owed to my dear friends Léna Molnar and Luke Rollo, for the consistent support and encouragement throughout these four years, and especially in these past few months. My time in Brisbane would be unimaginable without them, and I hope they can forgive me for leaving so quickly. To Donovan Miller and Innez Tulloch for the relaxed environment to come home to, and for putting up with a slowly disappearing housemate. To my sisters Anna and Natasha for their love and support despite the stresses of work and motherhood. I hope I can be a better, if crazier, uncle now.

Finally, to my parents, Judith and Elemer Szorkovszky, for personally investing so much interest and time into my education, of which this is only nominally the culmination. This is for them.

Keywords

optomechanics, electromechanics, quantum measurement, estimation, parametric amplification, squeezing, entanglement, tomography

Australian and New Zealand Standard Research Classifications (ANZSRC)

ANZSRC code: 020603, Quantum Information, Computation and Communication, 50%

ANZSRC code: 020604, Quantum Optics, 25%

ANZSRC code: 100704, Nanoelectromechanical Systems, 25%

Fields of Research (FoR) Classification

FoR code: 0206, Quantum Physics, 75%

FoR code: 1007, Nanotechnology, 25%

Contents

List of Figures

List of abbreviations used in this thesis

MEMS Micro-electromechanical system(s)

NEMS Nano-electromechanical system(s)

QND Quantum non-demolition

BAE Backaction evasion

DMPA Detuned mechanical parametric amplification

SME Stochastic master equation

SSE Stochastic Schrödinger equation

The bureaucracy is not a closed system; it is this that makes it a world instead of a thing.

David Foster Wallace, *The Pale King*

Chapter 1

Introduction

1.1 Mechanical oscillators

Pendula, diving boards and resonating strings of musical instruments. These objects, due to their ubiquity and their simple repetitive motion, are typical of some of the earliest studied physical systems. The work of Galileo and Huygens explained why a pendulum, for example, would make such an unprecedented time-keeping device. Firstly, to a good approximation, the period of a pendulum's motion depends only on its length and on the strength of gravity, both being constants to a fairly good approximation. Secondly, an oscillation once started will go on for many cycles undisturbed. Since this second property is a good indicator of effectiveness in time-keeping instruments and of purity of sound in musical instruments, the number of cycles before an oscillator's motion is damped substantially is now appropriately known as a "quality factor".

Simple harmonic oscillators, as these objects are now known in physics, can be abstracted as a "mass on a spring" which separates their two properties. The spring provides a restoring force to its resting, or equilibrium, position. The mass provides inertia, or resistance to accelerating forces. The ratio of these two quantities determines the frequency of oscillation. This can be seen by writing the classical equation of motion

$$m_{\text{eff}}\ddot{x} = -kx \tag{1.1}$$

where $\ddot{x}$ is the second time-derivative (or acceleration) of the object at position x, m_{eff} is the effective mass and k is the spring constant. The solution to such a differential equation is a sinusoid with frequency

$$f = \frac{1}{2\pi}\sqrt{k/m_{\text{eff}}} \tag{1.2}$$

or in an equivalent angular frequency

$$\omega_m = 2\pi f = \sqrt{k/m_{\text{eff}}} \tag{1.3}$$

In reality, oscillations do not last forever due to random collisions, for example with air molecules. The average result of this can be well approximated by a deterministic frictional

force, proportional to velocity $F_f = -\gamma m_{\text{eff}} \dot{x}$[1]. On the other hand, the random force from these collisions $F_{\text{T}}(t)$ creates new, stochastic (that is, random in time) fluctuations in the oscillator. The classical relationship between these two forces (i.e. the fluctuation-dissipation theorem) will be covered in section 1.3. Taking these new forces into account, the full equation of motion is

$$m_{\text{eff}} \ddot{x} + \gamma m_{\text{eff}} \dot{x} + kx = F_{\text{T}}(t) \tag{1.4}$$

In general, F_{T} is modelled as a white noise process. Often, such as for a heavy pendulum, these fluctuations are too small to be noticed. In this case, and if $\gamma \ll \omega_m$, the solution to the above equation is approximately

$$x(t) \approx x(0) \cos(\omega_m t)\, e^{-\gamma t} \tag{1.5}$$

The exponential decay becomes appreciable when $t = 2\pi/\gamma$, by which time the number of cycles is $\omega/\gamma = Q$.

These equations and the physical quantities within are well-known to any undergraduate student of physics. A mass-spring system represents the most intuitive form of the simple harmonic oscillator, and is a valuable teaching tool for Newtonian mechanics. However, while bulky mechanical oscillators are valuable for acoustical engineering and time-keeping, they remain relics of a bygone classical world in this age of miniaturisation and speed-of-light communication. This thesis deals with the question: is there a place for the mechanical oscillator in the quantum age?

1.2 Towards the quantum regime

As physics delved into the microscopic world, the ubiquity of simple harmonic oscillators became even more apparent. They are found in the vibrations of molecules and atomic lattices, in electromagnetic waves and in superconducting devices. As these systems all fall within the realm of quantum mechanics, an equivalent *quantum* version of the above mathematics has been well studied. In the case of electromagnetism, this has resulted in the field of quantum optics, from which many useful theoretical tools have emerged.

How does a quantum harmonic oscillator differ from its classical counterpart? There are a few very important distinctions, including:

Quantum oscillators can exist in superpositions and entangled states. These are the standard counter-intuitive quantum-mechanical effects that challenge ideas of locality and of a single objective reality. The field of quantum information exists to exploit these features.

[1] Throughout this thesis, we will use γ to signify the amplitude decay rate, so that the energy decays with rate 2γ.

A perfect measurement of the vibrational energy only allows discrete results. This reflects the fact that the vibrational energy in a harmonic oscillator can be thought of as consisting of an ensemble of indistinguishable particles (or bosons). For an electromagnetic field these particles are photons, while for a vibrational system, they are termed phonons.

A quantum oscillator is never at rest. With no external or thermal excitation, a quantum harmonic oscillator is in what is known as its ground state. The ground state has non-zero energy, consistent with Heisenberg's uncertainty principle applied to position and momentum. This is known as zero-point motion. By default, the mean-square position and momentum noise have equal energies, as is the case for thermal noise.

The oscillator is necessarily influenced by measurement. This influence comes in two forms: conditional and unconditional. The conditional influence is a reduction of the uncertainty in the measured observable. The quantum states prepared by so-called "projective measurements" are ostensibly real as long as the measurement result is kept. The unconditional influence is additional noise in the conjugate observable. This phenomenon is known as quantum backaction and is necessary for the uncertainty principle to hold. Measurement can therefore influence the ground state as described above. With a strong instantaneous position measurement, the conditional position uncertainty can be reduced below the level of the zero-point motion at the expense of increased momentum uncertainty. The resulting state directly after the measurement is known as a *squeezed state*.

A fundamental question surrounding quantum mechanics is whether such features are necessarily restricted to microscopic systems. Many attempts have been made to address why quantum effects do not exist at the scale of everyday experience, the most successful of these being the theory of decoherence[1]. According to this theory, interactions between the observed system and an unobserved environment result in "lost" information. Accounting for this lost information involves the loss of the quantum coherence required for effects such as superposition and entanglement to be observed. However, if interactions with the environment can be limited, macroscopic systems can, in principle, behave quantum-mechanically. This would allow the study of quantum mechanics in new regimes, such as that in which gravity is not negligible[2, 3].

The past three decades have seen much experimental effort in scaling up quantum systems towards the macroscopic level and likewise in scaling down macroscopic systems towards the quantum regime[4]. For example, double-slit interferometry has been recently scaled up to large molecules[5] and matter waves[6]. Similarly, the study of motional quantum states of trapped ions[7, 8] has paved the way for similar experiments with trapped nanoparticles[9, 10]. These last two examples technically fall under the umbrella of mechanical oscillators. Conversely, quantum behaviour of mechanical oscillators can be pursued by scaling down "bulk" oscillators such as beams, strings and cantilevers.

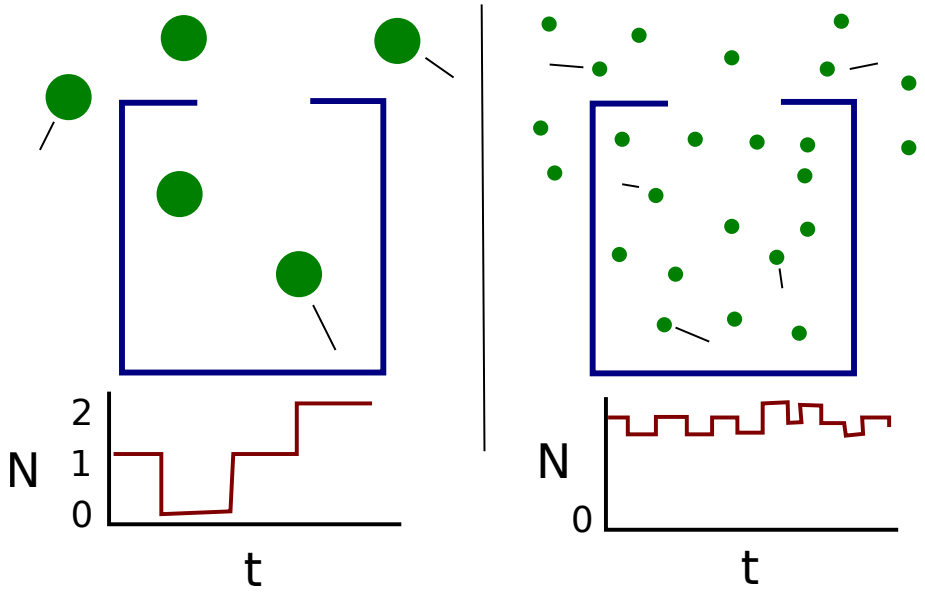

Figure 1.1: Depiction of an oscillator as a box containing either a few large particles or many small particles, with particles randomly exiting to and entering from the environment. If over time the number of the particles in the box can be monitored, the particle-like nature is more apparent in the box with higher-energy bosons. Here, the size of the opening in the box is a useful analogy for the dissipation rate.

A concrete limitation for quantum mechanical behaviour in large mechanical oscillators is set by their relatively low mode frequencies compared to conventional quantum oscillators. Since the energy of a boson is given by $E = hf$, a 1kHz oscillator mode at room temperature contains on the order of $N \approx 10^{10}$ phonons in the form of thermal noise, leading to fast decoherence. This decoherence is illustrated in Figure 1.1, using the analogy of particles entering and exiting a box. As temperature increases or frequency decreases, the mean number of phonons in the oscillator increases. Not only are many phonons more disordered, but they enter and exit the oscillator faster, disturbing the state of the oscillator. Additionally, such low phonon energies make measurement at the single phonon level virtually impossible. In contrast, single photons in the visible spectrum can be easily produced and detected[11].

Under what circumstances, then, can a mechanical oscillator exhibit the above quantum features? This question will be covered in detail in Chapters 2 and 3. As a rough guide, one would desire some combination of the following criteria

High mode frequency. This means smaller oscillators or (for trapped particles) tight confinement.

High quality factor. Damping is a macroscopic phenomenon that arises from noise entering and escaping the oscillator. Reducing the damping rate therefore reduces decoherence.

Low temperature. As for the damping rate, reducing the amount of thermal noise mitigates decoherence.

Quantum-scale position measurement and control. Throughout this thesis, "quantum-scale" refers to approximately the level of the zero-point motion. This is distinct from a backaction-dominating measurement, as will be shown in subsequent chapters.

Miniaturisation of bulk mechanical devices, incorporating piezoelectric and dielectric effects for measurement and control, began in the 1980s. These microelectromechanical systems (MEMS) have since opened up an active area of research devoted to their fabrication and use. Oscillators, such as beams and cantilevers, are used as temperature, force, mass and magnetic field sensors[12]. In particular, micron-scale cantilevers have found widespread use in atomic force microscopy, while MEMS gyroscopes and accelerometers have been critical for the recent revolution in "smart-phone" technology.

Continuing along this path, making use of fabrication technology such as electron beam lithography, oscillators may now be fabricated with feature sizes at the nano-scale[13]. Along with cryogenic refrigeration, this allows the study of high-frequency oscillators with very high quality factors and low thermal noise. Beginning with a classical context, I will discuss approaches to precision measurement, control and noise minimisation in such devices. This will be followed by discussion of amplification techniques, and a summary of recent efforts towards quantum-scale measurement and control.

1.3 Measurement, control and feedback

This thesis primarily concerns the continuous measurement of a noisy system — that is, a thermally excited oscillator. Since the 1950s, engineers have studied very similar problems in developing automated technologies. A thermostat, for example, requires a continuous measurement of the ambient temperature in order to continually adjust the heating and cooling controls in a feedback loop. The field that then developed around continuous feedback became known as control theory. In this section, I will briefly introduce various concepts in control theory with a focus on sensing, which will then be extended to the quantum regime in Chapter 3.

Mechanical oscillator-based sensors can be divided into two main categories. The first type sets up an oscillator to monitor its position, in order to directly sense forces at or near the oscillator frequency. Other influences such as external masses and temperature fluctuations, which affect oscillator parameters, are instead detected by monitoring the frequency of the oscillator. Both of these approaches are limited by measurement noise and by thermal noise. We will focus here on the first kind — that is, on the limitations of position measurement.

When the position of an oscillator is monitored with high sensitivity — such as by optical interferometry — in the absence of a signal to detect, random thermal fluctuations can be picked up. In this case, the mean-square fluctuation $\langle x(t)^2 \rangle$ is determined by the relative strength of the friction F_f and fluctuations F_{T} in equation (1.4). In Einstein's famous paper on Brownian motion, this quantity was derived and found to be proportional to the temperature T. For

an oscillator, these fluctuations will be distributed by frequency ω according to the oscillator's Lorentzian-shaped susceptibility

$$x(\omega) = F_{\mathrm{T}}(\omega)\chi_0(\omega) \tag{1.6}$$

where the susceptibility $\chi_0(\omega)$ is found by transforming Eq. (1.4) into the frequency domain

$$\chi_0(\omega) = \frac{1}{m_{\mathrm{eff}}(\omega_m^2 - \omega^2 + i\gamma\omega)} \tag{1.7}$$

Using the standard assumption that the thermal force F_{T} is white noise (i.e. power is independent of frequency), the power spectral density of the oscillator is then given by[14]

$$\begin{aligned} S_{XX}(\omega) &= 4\gamma k_B T m_{\mathrm{eff}} |\chi_0^2(\omega)| & (1.8)\\ &= \frac{4\gamma k_B T}{m_{\mathrm{eff}}} \frac{1}{(\omega^2 - \omega_m^2)^2 + \gamma^2\omega^2} & (1.9) \end{aligned}$$

where k_B is Boltzmann's constant. Moving away from the resonance frequency, the thermal signal will become weaker and eventually reach the measurement noise floor. In the case of an ideal optical interferometer, this is an evenly distributed shot-noise level.

Imagine now that we want to measure these random thermal forces over time. To do this, we want to continually estimate the oscillator's position, and have this estimate be as precise as possible. Given that the random thermal motion is characteristically different to the random measurement noise (namely, having a different frequency distribution), there exists a filter to optimally estimate the position signal from the time-varying measurement record. This filter is a function of the known noise properties and oscillator parameters. As a result of this filtering out of the noise, the uncertainty can be reduced from that given by the variance of the unfiltered measurement to what is known as the *conditional variance*. This quantity, which depends largely on the relative strength of the signal compared to the noise, represents how well the position is localised by the measurement and is therefore of great significance in quantum mechanics. The optimal filter and conditional variance for a quantum harmonic oscillator will be derived in Chapter 3.

An ideal continuous estimate of an oscillator's position is also useful in classical applications. By converting this estimate an applied feedback force, the oscillator's response can be controlled. Negative feedback, where the aim is to apply a force opposing the oscillator's velocity, reduces the effective susceptibility around the resonance and increases the effective damping rate. This commonly used technique is also termed cold damping (or active cooling) since this decreases the effective Q-factor while also reducing the level of thermal noise[15, 16]. Reversing the sign of negative feedback leads to a decreased damping rate, and ultimately self-sustained oscillation[17]. Both of these effects can be generalised by an effective susceptibility

$$\chi_0(\omega) = \frac{1}{m_{\mathrm{eff}}(\omega_m^2 - \omega^2 + i\omega(\gamma - \gamma_{fb}))} \tag{1.10}$$

where γ_{fb} can be positive or negative, corresponding to positive or negative feedback.

For a linear oscillator, feedback has no bearing on the resolution of a sensor, as the signal and noise are both subject to the same susceptibility[14, 18]. However, negative feedback can be useful to constrain an oscillator to the linear response regime, which generally bounds the dynamic range of transducers[19]. In this case, the minimum noise level achievable with perfect noiseless feedback is equivalent to the conditional variance[20].

1.4 Linear and phase-sensitive amplification

In everyday experience, an amplifier is a device that increases the energy of a signal compared to some noise. Perhaps the most familiar of these are the towers of amplified speakers at large outdoor concerts, necessary for singers and instruments to be audible from far away. For a person deep in the crowd, turning up the amplifiers increases the strength of the musical signal compared to the noise of the surrounding crowd. There is, however, another important signal-to-noise ratio in this situation. The signals first need to be measured by microphones or pickups. These microphones or pickups contain some finite amount of noise, which is also amplified. Therefore, the loudness of the instrument relative to the measurement noise in the pickups sets the ultimate limit to the signal-to-noise ratio as perceived by the distant listener (assuming, as many festival organisers do, that the listener's ears can handle arbitrarily loud volumes).

In the classical limit, our task of monitoring a simple mechanical resonator is no different to the task of recording an instrument with high fidelity. Continuing this analogy, it is reasonable to ask if the resonator can be made louder using some device, so that the measurement noise is weaker in comparison.[2] If a double bass, for example, is played on a floor with the right resonances, the instrument will be "pre-amplified" and made louder by the coupling.

This double bass example is reminiscent of one kind of controllable pre-amplifier. In abstract terms, a harmonic oscillator mode can be pre-amplified by coupling to a second oscillator mode, which must lose a corresponding amount of energy[21]. In the classical limit, this is completely equivalent to improving the measurement sensitivity. However, a quantum-mechanical limit is introduced if the signal is weak enough. Through this coupling the second mode must introduce its zero-point noise to the signal, ultimately limiting the signal resolution. In fact, any form of what is known as a "linear phase-insensitive amplifier" must introduce noise in order to not violate quantum mechanics[22].

An alternative, and simpler, pre-amplification process for an oscillator is parametric amplification. This does not require a second mode, and can be achieved by a simple modulation of the spring constant. The effect of this is for oscillations of a particular phase to be favoured

[2]Here, we run into the question of what constitutes a measurement, and must invoke quantum mechanics. For now, we can use the rule-of-thumb that a coupling a system to more than a few, traceable degrees of freedom is a measurement. For example, when an optical signal reaches a photodetector and becomes embedded in an environment of excited electrons.

over others. A fluctuation, such as from a thermal bath or an applied force, is therefore either amplified or damped depending on its phase with respect to the parametric drive. This amplification is noiseless in principle, and therefore highly suited to quantum applications as a way to circumvent measurement noise[21, 23, 24]. The phase-sensitive nature of parametric amplification causes the thermal noise in an oscillator to become unevenly distributed[25]. Similarly, when applied to the ground state, the noise reduction in one quadrature of motion results in a quantum squeezed state[26]. Parametric amplification is the primary focus of this thesis, and will be covered in depth in Chapter 4.

1.5 State of the art: Optomechanics and electromechanics

Bulk mechanical oscillators couple naturally to a wide variety of quantum systems. Therefore, in addition to fundamental physics, quantum-enabled mechanical oscillators are desirable for use in quantum memories[27, 28, 29] and to interface hybrid quantum information networks[30, 31, 32]. Presently, the pursuit of quantum-scale measurement and control of a mechanical oscillator can be divided among three kinds of architectures: optomechanical, electromechanical, and hybrid systems.

Firstly, in cavity optomechanics, a high-quality mechanical oscillator modulates the effective length of a high-quality optical or microwave cavity. As optical and microwave cavities exist in many sizes, the mechanical elements may range from the kilogram to the picogram scale[33, 34]. The large end of this scale was pioneered in efforts to detect the gravity waves emitted during cosmological events. One promising way of detecting gravity waves is to capture transient length perturbations in kilometer-scale interferometers[35]. The standard quantum limit for position measurement was identified in this context; it is at this limit that quantum backaction prevents further precision from a continuous measurement with increasing optical power. The technique of backaction evasion was subsequently developed by Braginsky et al[35, 36], in order to beat the standard quantum limit. This will be discussed further in Section 3.6.

The typical dispersive optomechanical interaction couples the position of a mechanical mode to the resonance frequency of a optical or microwave cavity mode. This can be achieved with a mechanical mode as one end of a Fabry-Perot cavity[38], as part of a whispering-gallery cavity structure[39] or photonic crystal[40], as a dielectric element[41, 42] or harmonically trapped nano-particle[9] in a cavity, or as the capacitive element of an microwave LC resonator[43], among others. Models incorporating a dissipative effect on the optical mode also exist[44], but will not be covered in this thesis. By driving the cavity on resonance, the position can be read out in the phase of the outgoing light. For smaller, high-frequency mechanical oscillators, the damping of the cavity may occur on a longer timescale than the mechanical period. Known as the "resolved sideband regime", this leads to additional possibilities depending on the strength

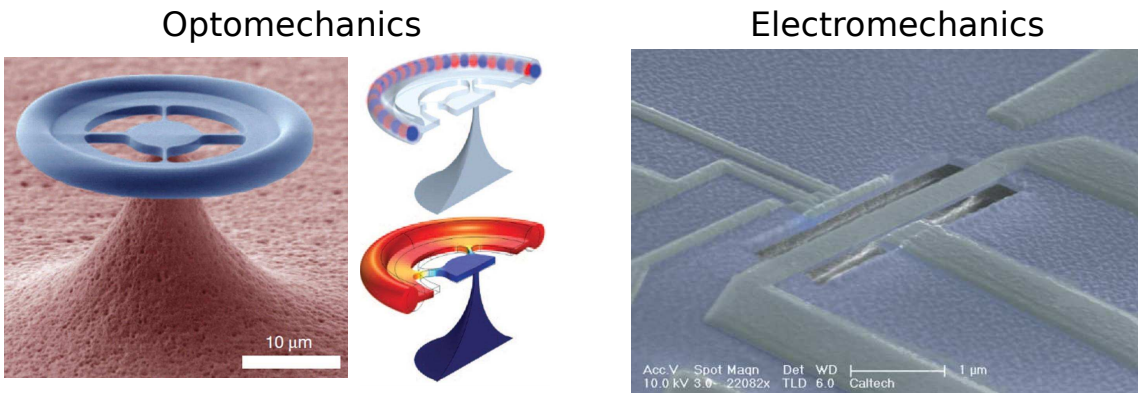

Figure 1.2: A toroidal optomechanical resonator (left) and a nanomechanical resonator coupled to a superconducting qubit (right). Left: the optical mode travels around the silica torus, with a resonance frequency dependent on the outer circumference of the toroid. A mechanical mode in the toroid, such as the radial breathing mode pictured, changes the circumference, thereby modulating the optical resonance. Light coupled in and out via a tapered fibre can then be modulated if tuned near this resonance. Right: A metal-coated silicon nitride beam is suspended over an etched gap. This is coupled to a Cooper pair box (CPB, above in picture) and an electrode. The charging energy of the CPB depends on the capacitance between the CPB and the nanoresonator, which depends on the distance between them. This leads to the oscillator frequency depending on the quantum state of the CPB, as can be confirmed by reflectometry via the electrode. Figures adapted from Verhagen et al. (2012)[27] and LaHaye et al. (2009)[37].

of the coupling. Passive cooling can be achieved by driving off-resonance, so that the optical mode forms a nearly zero-temperature bath for the mechanical mode[40, 43]. Driving on the other side of resonance leads to linear amplification of the mechanical mode and, with high optical power, dynamical instability[45]. A combination of these two drives is a simple method of backaction evasion[46].

Optomechanical systems, due to the versatility of the interaction and the efficiency of coupling, have accounted for the majority of progress in quantum-scale mechanical measurement to date. This progress includes milestones such as ground-state cooling[43, 40], observation of backaction noise[47] and measurement with imprecision below the standard quantum limit[48]. These capabilities are useful for verification of quantum states and for quantum-scale sensing. However, the level of quantum control possible with present-day experimental parameters is limited to the creation of Gaussian states such as squeezed states. More exotic quantum states, such as Schrödinger Cat states and number states are non-Gaussian.[3] While these kinds of states can be created using extended optomechanical techniques[49, 50] and the strong single-photon coupling regime[51], they are beyond present experimental capabilities.

Nanoelectromechanical systems (NEMS), on the other hand, are the conjunction of nano-

[3]Two-mode entanglement is possible with only squeezed Gaussian states, as will be covered in Section 2.4.

scale oscillators with electronic elements. The electronic component may be simply a classically modelled electrode, but can also involve solid-state qubits[52, 37], single-electron transistors[53], quantum point contacts[54, 55] and two-dimensional electron gases[56]. Although position measurement is far less efficient in these devices compared to optomechanics, nonlinearity of coupling allows a greater degree of control[57, 58, 59]. Notably, parametric amplification is very easily achieved using nonlinear capacitive forces[25, 60]. Additionally, the use of quantum electronics allows a wider array of quantum states to be prepared[26]. Significant milestones towards this goal that have been achieved to date include mechanical transduction of two-level quantum systems[37] and parametric amplification using a qubit[24]. Much progress has also been recently made with coupled oscillators in this architecture[61, 62], paving the way for quantum entanglement.

It is also possible to combine the precision measurement of optomechanics with the control capabilities of NEMS. The most notable example of this is using superconducting microwave optomechanics. Here, a coplanar waveguide resonator or a lumped-element LC oscillator forms the microwave cavity, allowing the typical optomechanical interaction[43]. This microwave resonator can then be coherently coupled to quantum electronic elements such as SQUIDs[63] or Cooper pair boxes[64], which share this superconducting architecture. Other proposals for hybrid systems include electrodes added to optical cavities[65, 66, 67, 68] and combined optical-microwave systems[69].

1.6 Outline of thesis

In this thesis, I will be investigating the combination of continuous position measurement and an independent parametric drive applied to a mechanical oscillator. I will show that a parametric drive can allow the kinds of quantum measurement currently possible in optomechanics, but with less reliance on efficient measurement and without the need for backaction evading techniques. Consequently, this finds application in NEMS and hybrid systems in which parametric amplification is possible but quantum-scale measurement is still out of reach, or in systems where control capabilities are otherwise sacrificed in favour of strong measurement.

Chapter 2 introduces the necessary quantum mechanical formalisms for a harmonic oscillator. Chapter 3 covers basic quantum measurement, introducing rotating-wave master equations for continuous position measurement as well as backaction evasion. In Chapter 4, conditional and unconditional dynamics are derived for an oscillator in the presence of a detuned parametric drive. This contains the key result that conditioning due to measurement can be enhanced by detuned parametric amplification. The main results of this chapter are then confirmed experimentally in Chapter 5. Chapter 6 applies this idea to the low-temperature quantum regime, quantifying the amount of quantum squeezing that can be generated, as well as effectiveness as a QND measurement. Similarly, Chapter 7 transports the concept to two-mode schemes and quantifies the quantum entanglement that can be generated. Finally, in Chapter 8, quantum

measurement of an oscillator is subjected to an alternative approach based on linear quantum trajectories. This approach is applied to quantum state tomography in the presence of resonant parametric amplification.

Chapter 2

Quantum states of harmonic oscillators

2.1 The rotating wave approximation and quadrature phase space

The state of a classical oscillator at a particular time can be described entirely by its position and momentum, both of which are exactly defined. If appropriately normalised versions of these two variables are used as axes on a graph, an undisturbed oscillator will trace out circles about the origin. For a quantum harmonic oscillator, the state at a particular time can instead be described by time-dependent probability distributions over position and momentum, now represented as operators $\tilde{x}$ and $\tilde{p}$[1]. For the ground state $|0\rangle$, the distribution is Gaussian with

$$\langle 0|\tilde{x}|0\rangle = \langle 0|\tilde{p}|0\rangle = 0 \tag{2.1}$$

$$m_{\text{eff}}\omega_m\langle 0|\tilde{x}^2|0\rangle = \frac{\langle 0|\tilde{p}^2|0\rangle}{m_{\text{eff}}\omega_m} = \hbar/2 \tag{2.2}$$

$$\langle 0|\tilde{x}\tilde{p}+\tilde{p}\tilde{x}|0\rangle = 0\ . \tag{2.3}$$

The second of these is a result of equipartition of energy and the uncertainty principle, defined by the canonical commutation relation

$$[\tilde{x},\tilde{p}] = \hbar/2 \tag{2.4}$$

which enforces a minimum uncertainty product

$$\Delta\tilde{x}\Delta\tilde{p} \geq \hbar/2\ . \tag{2.5}$$

The time-evolution of the state can be found in terms of the Hamiltonian for a quantum harmonic oscillator, which defines the total energy as the sum of kinetic and potential energies

$$\tilde{H} = \frac{\tilde{p}^2}{2m_{\text{eff}}} + \frac{1}{2}\omega_m\tilde{x}^2 \tag{2.6}$$

[1]Throughout this thesis, the tilde sign ($\sim$) is reserved for operators in the laboratory frame, while the hat sign ($\hat{}$) is reserved for operators in the rotating frame

In the Heisenberg picture, the expected value of an observable $\hat{A}$ evolves as

$$\mathrm{d}\langle\hat{A}\rangle = \frac{i}{\hbar}\langle[\tilde{H},\hat{A}]\rangle\,\mathrm{d}t \tag{2.7}$$

Substituting $\hat{A}=\tilde{x}$ or $\hat{A}=\tilde{p}$ with the above Hamiltonian results in equations of motion similar to those for a classical oscillator. It can also easily be seen that an initial ground state does not evolve with time under this Hamiltonian.

The distributions over $\tilde{x}$ and $\tilde{p}$ above become complicated, however, if the oscillator is excited out of the ground state. If the decay of the oscillator occurs on a much longer timescale than the oscillator period (i.e. high Q), along with all other relevant dynamics, it is much more convenient to use a quadrature phase space. This assumes that the momentum is approximately the same as the position (correctly normalised) a quarter of a cycle earlier. Converting the operators to this new phase space requires transforming to an interaction picture and making the rotating wave approximation. Rewriting $\tilde{x}$ and $\tilde{p}$ in terms of the ladder operators $\tilde{a}$ and $\tilde{a}^\dagger$

$$\sqrt{\frac{m_{\mathrm{eff}}\omega_m}{\hbar}}\,\tilde{x} = (\tilde{a}+\tilde{a}^\dagger)/\sqrt{2} \tag{2.8}$$

$$\sqrt{\frac{1}{\hbar m_{\mathrm{eff}}\omega_m}}\,\tilde{p} = -i(\tilde{a}-\tilde{a}^\dagger)/\sqrt{2} \tag{2.9}$$

such that

$$[\tilde{a},\tilde{a}^\dagger] = -2i[\tilde{x},\tilde{p}]/\hbar = 1\ , \tag{2.10}$$

the stationary-frame Hamiltonian becomes

$$\tilde{H} = \hbar\omega_m(\tilde{a}^\dagger\tilde{a}+1/2) = \tilde{H}_0 \tag{2.11}$$

The transformation to a rotating frame at ω_m is then made by defining the operators

$$\hat{a} = e^{i\tilde{H}_0 t/\hbar}\tilde{a}e^{-i\tilde{H}_0 t/\hbar} \tag{2.12}$$

$$= \tilde{a}e^{i\omega_m t} \tag{2.13}$$

$$\hat{a}^\dagger = e^{i\tilde{H}_0 t/\hbar}\tilde{a}^\dagger e^{-i\tilde{H}_0 t/\hbar} \tag{2.14}$$

$$= \tilde{a}^\dagger e^{-i\omega_m t} \tag{2.15}$$

This transformation also applies to remaining terms in the Hamiltonian, which become known as the interaction Hamiltonian. Terms that evolve on the order of the rotating frame frequency ω_m or faster are discarded, while slower terms are kept. In this case, since there are no other terms, the interaction Hamiltonian is $\hat{H}_I = 0$. In other words, when using this basis, the quantum state is stationary in time.

The position and momentum operators, given in terms of stationary operators by Eqs (2.8-2.9), can now be represented in terms of their rotating-wave equivalents. This leads to a decomposition into slower-evolving degrees of freedom X and Y.

$$\sqrt{\frac{m_{\mathrm{eff}}\omega_m}{\hbar}}\,\tilde{x} = \hat{X}\sin(\omega_m t)+\hat{Y}\cos(\omega_m t) \tag{2.16}$$

$$\sqrt{\frac{1}{\hbar m_{\mathrm{eff}}\omega_m}}\,\tilde{p} = \hat{Y}\sin(\omega_m t)-\hat{X}\cos(\omega_m t) \tag{2.17}$$

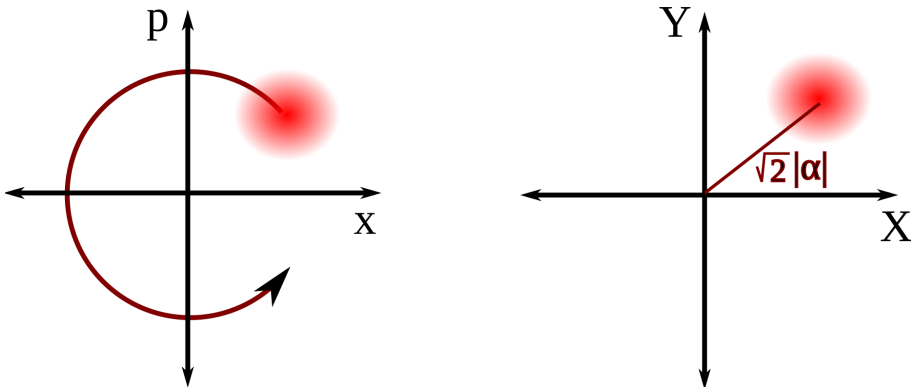

Figure 2.1: Representations of the position-momentum phase space (left) and quadrature phase space (right), which are equivalent in the limit of low damping. In the position-momentum phase space, with appropriate scaling, a coherent oscillation is represented by a state that follows a circular path with time. In quadrature phase-space, the same oscillation is represented as stationary values of X and Y.

where

$$\hat{X} = (\hat{a} + \hat{a}^\dagger)/\sqrt{2} \tag{2.18}$$

$$\hat{Y} = -i(\hat{a} - \hat{a}^\dagger)/\sqrt{2}\,. \tag{2.19}$$

Taking the commutator of each side of the above two equations, we find

$$[\hat{X}, \hat{Y}] = i[\hat{a}, \hat{a}^\dagger] = i \tag{2.20}$$

In this new phase space, the amplitude is given by the distance from the origin and the phase of oscillation is the angle from the X-axis. The total squared amplitude is

$$\frac{m_{\rm eff}\omega_m}{\hbar}\tilde{x}^2 + \frac{1}{\hbar m_{\rm eff}\omega_m}\tilde{p}^2 = \hat{X}^2 + \hat{Y}^2 \tag{2.21}$$

The left hand side has an expectation value of unity. Due to symmetry, the ground state variance for each quadrature is therefore $V_X = V_Y = 1/2$.

Besides its usefulness for describing quantum states, the quadrature picture contains the seeds of backaction evading position measurement. Since position and momentum are dynamically linked, the backaction of a strong position measurement will result in momentum noise, which becomes position noise one quarter of a cycle later. This sets a fundamental limit to the accuracy of a continuous position measurement. However, for a freely evolving oscillator the position quadratures X and Y are not dynamically linked, since in the rotating frame $\hat{H}_I = 0$. Therefore, one quadrature can be continuously measured with arbitrary accuracy, with the backaction noise only affecting the other quadrature.

2.2 Coherent states and the density matrix

In the rotating frame, a pure coherent oscillation is simply a ground state displaced in quadrature phase space, as shown in Figure 2.1. This can be assigned a complex number α, and the

corresponding quantum state can be written $|\alpha\rangle$. This state has the property

$$(\langle\alpha|\hat{X}|\alpha\rangle + i\langle\alpha|\hat{Y}|\alpha\rangle)/\sqrt{2} = \langle\alpha|\hat{a}|\alpha\rangle = \alpha \tag{2.22}$$

In words, the real and imaginary parts of α are the expectation values of $\hat{X}$ and $\hat{Y}$ (up to a factor of $\sqrt{2}$). The amplitude of oscillation is $|\alpha|$ and the phase of oscillation is Arg$[\alpha]$. The ground state is then simply the case $\alpha = 0$.

Coherent states form a complete basis for quantum states of an oscillator. As a simple example, the pure superposition state

$$|\psi\rangle = (|\alpha\rangle + |-\alpha\rangle)/\sqrt{2} \tag{2.23}$$

is known as a cat state. A generalised state can be represented as a density matrix

$$\hat{\rho} = \int P(\alpha)|\alpha\rangle\langle\alpha|\,\mathrm{d}^2\alpha \tag{2.24}$$

which allows for both quantum superpositions and classical mixtures of coherent states. Expectation values of an operator $\hat{A}$ are given by the trace

$$\begin{aligned} \langle\hat{A}\rangle &= \int P(\alpha)\langle\alpha|\hat{A}|\alpha\rangle\,\mathrm{d}^2\alpha & (2.25)\\ &= \mathrm{Tr}(\hat{\rho}\hat{A}) & (2.26) \end{aligned}$$

In the Heisenberg picture, similarly to Eq. (2.7) this expectation value evolves as

$$\mathrm{d}\langle\hat{A}\rangle = \frac{-i}{\hbar}\langle[\hat{H},\hat{A}]\rangle\,\mathrm{d}t \tag{2.27}$$

This thesis will be limited to mixed Gaussian states. For these states, the highest statistical moments are given by

$$\begin{aligned} V_X &= \langle\hat{X}^2\rangle - \langle\hat{X}\rangle^2 & (2.28)\\ V_Y &= \langle\hat{Y}^2\rangle - \langle\hat{Y}\rangle^2 & (2.29)\\ C &= \langle\hat{X}\hat{Y} + \hat{Y}\hat{X}\rangle/2 - \langle\hat{X}\rangle\langle\hat{Y}\rangle\ . & (2.30) \end{aligned}$$

These, along with the means $\langle X\rangle, \langle Y\rangle$ characterise the state. The purity of the state is given by

$$P = \frac{1}{4(V_X V_Y - C^2)} \leq 1 \tag{2.31}$$

which has a maximum of unity for a coherent or squeezed coherent state and is reduced for a mixture. This quantity is important to quantum applications, which rely on quantum rather than classical superpositions. These applications include the production of exotic nonclassical states[70], entanglement between multiple oscillators[71] and continuous variable quantum computing[72].

2.3 Squeezed states

Quantum squeezing occurs when one quadrature has a variance smaller than the ground-state variance. This has to be accompanied by an increase in the orthogonal quadrature in order to preserve the uncertainty principle, given by Eq. (2.5) in the case of position and momentum. Squeezing of the position or momentum is possible by using a strong projective measurement, however this is difficult to sustain due to their dynamic relationship. That is, squeezing the position adds momentum noise, which becomes position noise a quarter of a cycle later. In this section we will consider the slower-evolving position quadratures $\hat{X}$ and $\hat{Y}$. A pure ($P = 1$) squeezed state can be characterised by the variances

$$V_X = \frac{1}{2g}\cos^2(\theta) + \frac{g}{2}\sin^2(\theta) \tag{2.32}$$

$$V_Y = \frac{1}{2g}\sin^2(\theta) + \frac{g}{2}\cos^2(\theta) \tag{2.33}$$

$$C = (\frac{g}{4} - \frac{1}{4g})\sin(2\theta) \tag{2.34}$$

where $g > 1$ determines the magnitude of squeezing. When $\phi = 0, \pi$, the X quadrature is maximally squeezed, and when $\phi = \pi/2, 3\pi/2$ the Y quadrature is maximally squeezed.

As will be shown in the next chapter, single-quadrature measurement can result in a squeezed state by reducing the uncertainty of the measured quadrature at the expense of back-action in the other. Another, unconditional, way to reduce the uncertainty of one quadrature is to modify the way that energy is distributed — that is, to break the symmetry between quadratures. This can be done by modulating the spring constant at twice the resonance frequency ω_m. A sinusoidal force at frequency ω_m will then encounter either a reduced or increased effective spring constant, depending on its phase with respect to the modulation. This process, known as parametric modulation, can be described by the Hamiltonian

$$\tilde{H} = \frac{\tilde{p}^2}{2m} + \frac{\tilde{x}^2}{2}[k_0 - k_r\sin(2\omega_m t + 2\theta)] \tag{2.35}$$

$$= \tilde{H}_0 + \tilde{H}_I \tag{2.36}$$

where the interaction Hamiltonian is

$$\tilde{H}_I = -\frac{\tilde{x}^2}{2}k_r\sin(2\omega_m t + 2\theta) \tag{2.37}$$

To transform into the rotating frame, we can use the substitution $\tilde{a} \to \hat{a}\exp(-i\omega_m t)$. Expanding out x^2 and the sine function, we get

$$\hat{H}_I = \frac{k_r}{8k_0}i\hbar\omega_m(\hat{a}^2e^{-2i\omega t} + \hat{a}^\dagger\hat{a} + \hat{a}\hat{a}^\dagger + \hat{a}^{\dagger 2}e^{2i\omega t})(e^{2i\omega_m t + 2i\theta} - e^{-2i\omega_m t - 2i\theta}) \tag{2.38}$$

Of the eight resulting terms, only two are time-independent. Under the rotating wave approximation, the other terms are discarded, leaving

$$\hat{H}_I = \frac{i\hbar\chi}{2}(\hat{a}^2e^{2i\theta} - \hat{a}^{\dagger 2}e^{-2i\theta}) \tag{2.39}$$

$$= \mathrm{S}[\chi\exp(-i\theta)] \tag{2.40}$$

where

$$\chi = \frac{k_r}{4k_0}\omega_m \tag{2.41}$$

can be interpreted as proportional to the peak-to-peak frequency modulation of ω_m. The rotating wave approximation requires that $\chi \ll \omega_m$, or equivalently that the spring-constant modulation k_r is small compared to the original spring constant k_0. The squeezing operator S is standard in quantum optics. Applying the Heisenberg equation of motion with $\theta = 0$

$$\begin{aligned} \mathrm{d}\langle\hat{X}\rangle &= -\chi\langle\hat{X}\rangle\,\mathrm{d}t & (2.42)\\ \mathrm{d}\langle\hat{Y}\rangle &= \chi\langle\hat{Y}\rangle\,\mathrm{d}t & (2.43)\\ \mathrm{d}\langle\hat{X}^2\rangle &= -2\chi\langle\hat{X}^2\rangle\,\mathrm{d}t & (2.44)\\ \mathrm{d}\langle\hat{Y}^2\rangle &= 2\chi\langle\hat{Y}^2\rangle\,\mathrm{d}t & (2.45) \end{aligned}$$

The parametric drive strength χ here appears as a positive and negative damping rate for the $\hat{X}$ and $\hat{Y}$ quadrature, respectively. When applied to an initial coherent state, the zero-point noise becomes distributed unevenly between quadratures. It is easy to show that the product $V_X V_Y$ remains constant, so the state remains pure. In other words, no additional noise is required to saturate the uncertainty principle, and the amplification is therefore noiseless in principle. This stands in contrast to linear (phase-insensitive) amplification which must necessarily add noise, as discussed in Section 1.4.

After a modulation for time t, the variances are given by Eqs (2.32-2.34), where

$$g = e^{2\chi t} \tag{2.46}$$

In reality, the squeezing is limited by noise and dissipation. The effect of parametric modulation in the presence of thermal noise, dissipation, measurement and detuning will be examined in Chapter 4.

2.4 Entangled Gaussian states

While squeezing of a single mode is useful for sensing due to the reduced quantum noise in one quadrature[35], it has less practical utility than single-mode non-Gaussian quantum states. However, the crucial quantum resource of quantum entanglement can be unlocked when squeezing exists in collective modes. Take as an example two oscillators with positions x_1 and x_2. If by some means the positions can be correlated so that $x_1 - x_2$ has very low uncertainty, while the positions individually have relatively large uncertainty, then a measurement of x_1 will also reduce the uncertainty of x_2. This is true even classically, and does not in itself imply quantum behaviour. This classical kind of entanglement is based on a reality in which x_1 and x_2 have well-defined values but are unknown to the observer. Quantum noise is, however, fundamentally indeterministic. If the uncertainties in x_1 and x_2 are comprised of quantum mechanical noise, a projective measurement of x_1 must therefore *prepare*, rather than verify, the state of

the second oscillator. The implied inseparability of the two ostensibly separated systems due to this instant disturbance is the subject of the EPR paradox[73]. This phenomenon implying "spooky action at a distance" is perhaps the most perplexing feature of quantum mechanics, and has been widely demonstated[74]. It should be noted that in this continuous-variable setting, the EPR paradox can still be resolved by hidden variables, since the joint probability distribution is classical[75]. Nonetheless, entanglement in variables such as position and momentum is believed to be valuable for continuous-variable quantum computation[76] and tests of macroscopic quantum mechanics[2, 6].

Quantitatively, the conditions for quantum entanglement in Gaussian states can be expressed in multiple equivalent ways based on a covariance matrix characterising the system. Simon gives a condition based on single mode variances and their correlations[77], while Duan presents an equivalent condition based on collective mode variances[78]. Duan's form of inseparability, naturally suited to experimental scenarios such as two-mode optical squeezing, will be used here. In the rotating frame, one can define the collective quadratures

$$X_C = (|a|X_1 + \frac{1}{a}X_2)/\sqrt{2} \tag{2.47}$$

$$Y_C = (|a|Y_1 - \frac{1}{a}Y_2)/\sqrt{2} \tag{2.48}$$

where a is any nonzero real number. A sufficient condition for entanglement is then

$$\mathrm{Var}(X_C) + \mathrm{Var}(Y_C) < (a^2 + \frac{1}{a^2})/2 \tag{2.49}$$

Duan then derives a *necessary* and sufficient condition for entanglement by restricting a to a particular value a_0 that depends on the covariance matrix. In the simplest case, the elements of the covariance matrix are given by $V_{X1} = V_{X2} = V_{Y1} = V_{Y2}$, $C_{XX} = -C_{YY}$, and $C_{XY} = C_{YX} = 0$, producing $a_0 = \pm 1$. Letting $a = 1$, and naming the resulting collective quadratures $X_C = X_+$ and $Y_C = Y_-$, the condition becomes

$$S_S = V_{X+} + V_{Y-} < 1 \tag{2.50}$$

That is, the arithmetic mean of the two collective quadrature variances must be below the ground state variance. The sum $S_S < 1$ therefore quantifies the amount of entanglement. This quantity is directly related to the log-negativity[79] by

$$E_N = -\ln(S_S) \tag{2.51}$$

for $S_S < 1$. Notably, $[X_+, Y_-] = 0$, so there is no physical lower bound to S_S due to the uncertainty principle. In other words, V_{X+} and V_{Y-} can be arbitrarily squeezed at the expense of V_{X-} and V_{Y+}, while the individual oscillators have both quadrature variances at or above the zero-point motion. This implies correlations between the oscillators at such a level that measurement of one must disturb the other.

If the two oscillators have different properties, it is possible to modify a_0 to retain a necessary and sufficient condition for entanglement. However, this assumes a certain form for the covariance matrix. A more convenient product form of inseparability has been given by Bowen[80] in the spirit of the product criterion for the EPR paradox proposed by Reid[81]. In this case, the sufficient condition for entanglement is

$$2\sqrt{\mathrm{Var}(X_C)\mathrm{Var}(Y_C)} < (a^2 + \frac{1}{a^2})/2 \tag{2.52}$$

When $\mathrm{Var}(X_C) = \mathrm{Var}(Y_C)$, this reduces to the sum form above. Notably, in this product form the value a_0 that gives the necessary condition is insensitive to certain operations on the covariance matrix. Again setting $a = 1$, we obtain a sufficient condition for entanglement, that is also necessary in the symmetric case

$$S_P = 2\sqrt{V_{X+}V_{Y-}} < 1 \tag{2.53}$$

In this form, the *geometric* mean of the two collective quadratures must be below the ground state variance. Even in the case that $V_{X1} = V_{X2}$, $V_{Y1} = V_{Y2}$ and $C_{XY} = C_{YX} = 0$, this condition remains necessary and sufficient for certain values of C_{XX} and C_{YY}. In other words, for a given value of a_0, the product form places fewer restrictions on the covariance matrix than the sum form. Notably, if $V_{X+} \neq V_{Y-}$ then this condition, even when no longer strictly necessary for entanglement, is more lenient on the larger of the two variances. The quantity S_P will be used for analysis of two-mode entanglement in Chapter 7.

Chapter 3

Quantum measurement of a mechanical oscillator

3.1 Introduction

When continuously monitoring the position of a mechanical oscillator at finite temperature, three regimes inevitably emerge[82]. In the regime in which even the oscillator's Brownian motion cannot be resolved, termed here the *bad measurement* regime, the uncertainty of the position estimate is dominated by thermal noise. In the *classical measurement* regime, the thermal Brownian motion can be resolved but the zero-point motion cannot, and the uncertainty is then dominated by measurement noise. Finally, a measurement strong enough to resolve the zero-point motion results in the *back-action dominated* regime. The border between the second and third regimes, when considering force sensitivity, is usually termed the standard quantum limit (SQL)[35]. It is here that the uncertainty of a continuous position estimate begins to saturate at the ground state variance, provided the measurement is efficient and suitably filtered[82]. On the other hand, a backaction evading measurement will allow one quadrature of motion to be transduced with uncertainty below the zero-point motion. In this chapter, I will use master equation formalisms developed in quantum optics to model thermal noise, backaction noise and measurement conditioning. These master equations will then be used to analyse both continuous measurement and backaction evading measurement of a mechanical oscillator, highlighting these three regimes.

3.2 The master equation for a dissipative oscillator

The Schrödinger equation describes the unitary evolution of a pure quantum state in a closed system. However, we wish to model an open system: an oscillator that is being continuously measured and under the influence of dissipation. Since the state is influenced by noise, it is better to use a statistical description based on the density matrix. The standard way to model

this evolution is using what is known as a master equation[83].

First we will model the influence of the dissipation via the thermal bath, which cannot be directly measured. The thermal noise and dissipation of a mechanical oscillator is treated using the Lindblad master equation. This turns out to be equivalent to the more commonly encountered case of an optical cavity, as shown in Ref. [82]. As it is based on the density matrix, the master equation encapsulates any observable of the system, including mean values and variances. The evolution of a generalised observable $\hat{A}$ is given by

$$\mathrm{d}\langle\hat{A}\rangle = -\frac{i}{\hbar}\langle[\hat{A},\tilde{H}]\rangle\,\mathrm{d}t + [2\gamma N]\langle\mathcal{D}[\hat{a}^\dagger]\hat{A}\rangle\,\mathrm{d}t + [2\gamma(N+1)]\langle\mathcal{D}[\hat{a}]\hat{A}\rangle\,\mathrm{d}t \tag{3.1}$$

where the mean phonon occupation N is governed by the Bose-Einstein distribution

$$N = \frac{1}{\exp(\hbar\omega_m/k_BT)-1}\ . \tag{3.2}$$

The first term in Eq. (3.1) is the unitary evolution in the Heisenberg picture introduced in Section 2.1. The additional terms contain the Lindblad superoperator

$$\mathcal{D}[\hat{a}]\hat{A} = \hat{a}^\dagger\hat{A}\hat{a} - \frac{1}{2}(\hat{a}^\dagger\hat{a}\hat{A} + \hat{A}\hat{a}^\dagger\hat{a})\ ,$$

The Lindblad term for the annihilation operator $\hat{a}$ describes dissipation. This outweighs the $\hat{a}^\dagger$ term, describing noise entering the system, by the energy damping rate 2γ. Consequently, when setting $\hat{H}=0$ and solving for $\hat{A}=\hat{X}$ and $\hat{A}=\hat{Y}$ we obtain a simple decay towards zero in each case

$$\mathrm{d}\langle\hat{X}\rangle = -\gamma\langle\hat{X}\rangle\mathrm{d}t \tag{3.3}$$

$$\mathrm{d}\langle\hat{Y}\rangle = -\gamma\langle\hat{Y}\rangle\mathrm{d}t\ . \tag{3.4}$$

The thermal noise terms proportional to N enter when solving for the variances, the time-derivatives of which are given by

$$\begin{aligned}
\mathrm{d}V_A &= \mathrm{d}[\langle\hat{A}^2\rangle - \langle\hat{A}\rangle^2] \\
&= \mathrm{d}\langle\hat{A}^2\rangle - 2\langle\hat{A}\rangle\mathrm{d}\langle\hat{A}\rangle - (\mathrm{d}\langle\hat{A}\rangle)^2 \\
\mathrm{d}C &= \mathrm{d}[\langle\hat{X}\hat{Y}+\hat{Y}\hat{X}\rangle/2 - \langle\hat{X}\rangle\langle\hat{Y}\rangle] \\
&= \frac{1}{2}\mathrm{d}\langle\hat{X}\hat{Y}+\hat{Y}\hat{X}\rangle - \langle\hat{X}\rangle\mathrm{d}\langle\hat{Y}\rangle - \langle\hat{Y}\rangle\mathrm{d}\langle\hat{X}\rangle - \mathrm{d}\langle\hat{X}\rangle\mathrm{d}\langle\hat{Y}\rangle\ .
\end{aligned} \tag{3.5}$$

The squared differential terms are used to account for stochastic increments, which will be used later. Using the rule $(\mathrm{d}t)^2=0$, these terms disappear for the deterministic evolution here[84]. This leaves

$$\mathrm{d}V_X = -2\gamma V_X\,\mathrm{d}t + \gamma(2N+1)\,\mathrm{d}t \tag{3.6}$$

and similarly for V_Y, while $C=0$. Setting the left hand side to zero gives the steady-state solution $V_X = V_Y = N+1/2$, as expected from our definition of N as the thermal phonon number. If the initial variances of the system differ from this steady-state value, they will relax back to it exponentially with a rate 2γ.

3.3 Continuous measurement and estimation

In order to find the conditional variance, we need to include measurement into the model. A continuous measurement can be treated as a series of measurements separated by a time dt. Since the measurement doesn't extract all of the information about the position at once, the measurement result includes some noise.

Let us call the measurement result at each time d$Q_X(t)$ for some classical variable $X(t)$ that evolves linearly. According to the above description, this should look like

$$\mathrm{d}Q_X(t) = k\langle X(t)\rangle \mathrm{d}t + \mathrm{d}W(t) \tag{3.7}$$

where k is some constant that increases with the fidelity of the measurement. The noise term d$W(t)$ is known as a Wiener increment, with a zero-mean Gaussian probability distribution with constant variance[84]. At each time step, these increments are independent of each other, so that over time $W(t)$, the Wiener process, is a random walk. Eq. (3.7) therefore states that if the entire measurement process is repeated many times, d$Q_X(t)$ should on average be proportional to the expectation value of X at each time. The noise that makes dQ_X differ from X is known as the residual noise, or innovation.

If the mean value were a constant, that is $\langle X(t)\rangle = X_0$ for all times, then every d$Q_X(t)$ would be an independent estimate of X_0, and a simple average of all measurement results would be ideal. A total estimate $X_{\mathrm{est}}(t)$ can then be trivially formed as being proportional to the sum of every result. That is,

$$X_{est}(t) = \int_0^t G\mathrm{d}Q_X(\tau) = GQ_X(t)\ , \tag{3.8}$$

where G is some constant, known as a gain for reasons which will become clear. Substituting in Eq. (3.7) with a constant mean value, we get

$$X_{est}(t) = G(ktX_0 + W(t))\ . \tag{3.9}$$

The conditional variance can be thought of as the minimum mean-square difference between the quadrature amplitude X and the observer's best possible estimate X_{est}, or

$$V_X(t) = \langle (X(t) - X_{\mathrm{est}}(t))^2\rangle\ . \tag{3.10}$$

In this simplified example the optimisation is over the gain paramater G. It is easy to show that in this case the optimum is $G = 1/kt$, leaving

$$V_X(t) = \frac{\langle W^2(t)\rangle}{k^2t^2}\ . \tag{3.11}$$

The Wiener process $W(t)$ is a random walk, so its variance increases with time. More precisely, as defined it has a variance equal to the time t of the walk[84]. This leads finally to

$$V_X(t) = \frac{1}{k^2t} \tag{3.12}$$

That is, the accuracy of the estimate increases with the measurement time and with the parameter k that defines the fidelity of the measurement. This variance is equivalent to the square of a basic standard error, where the result at each time step is treated as an independent trial.

In general, however, the observable to be estimated changes over time due to noise (such as thermal noise) and/or internal dynamics. We are interested in real-time estimation of an observable X, which is useful for control applications such as feedback cooling[85]. In this case, noise in X makes recent measurement results more trustworthy than those further in the past. In addition, estimates need to be updated to reflect the internal dynamics. Both of these concerns can be accounted for by generalising Eq. (3.8)to have a time-dependent gain

$$X_{\text{est}}(t) = \int_0^t G(\tau, t)\mathrm{d}Q_X(\tau) \tag{3.13}$$

$G(\tau, t)$ now defines a filter function for the measurement results. Equivalently, the optimal estimate can be modelled in a differential form as

$$\mathrm{d}X_{\text{est}}(t) = U(t)X_{\text{est}}(t) + K(t)\mathrm{d}W(\tau) \tag{3.14}$$

In this case, all the linear dynamics governing X are given by $U(t)$, while $K(t)$ is known as the Kalman gain. This form is easily generalised to multiple interacting observables, so that $X_{\text{est}}(t)$ and the residual noise $W(t)$ are vectors, and $U(t)$ and $K(t)$ are matrices. In this general case, $K(t)$ is found to be proportional to the conditional covariance matrix[20]. As shown in the next section, this allows the conditional variances and optimal filter to be solved in a straightforward manner.

3.4 The stochastic master equation

In quantum mechanics, it is generally not natural to think of an observable having a "true" value distinct from measurement result. Instead, we think of a wavefunction describing our knowledge which is collapsed to a more localised state by the measurement. Fortunately, the picture of an estimate provided by Equation (3.14) translates very well to the master equation formalism, which describes one's knowledge of a quantum system. The master equation can then be extended so that the change in the density matrix at time t also depends on the measurement outcome at that time, to reflect the new information. If, for instance, a position quadrature is measured, the conditional variance in that quadrature is reduced while the conditional mean is shifted according to the measurement result. Since this measurement is noisy, as explained above, the resulting equation is therefore known as a stochastic master equation. An excellent introduction to the topic in general is provided by Jacobs and Steck[86]. Here, I will explain the formalism briefly, before applying it to a general position measurement in the rotating frame.

First we create a standard definition for a noisy measurement result of a quantum observable X, after Equation (3.7), as

$$\mathrm{d}Q_X(t) = \sqrt{4\eta\mu}\langle\hat{X}(t)\rangle\mathrm{d}t + \mathrm{d}W(t)\ , \tag{3.15}$$

where $\eta \leq 1$ is the quantum efficiency, μ is a parameter defining the strength of the measurement and W is a Wiener process. Since white noise has units of $s^{1/2}$[84], μ has units of Hz. The efficiency is included to allow for a reduced conditioning if some of the backaction-inducing measurement is lost.

The effect of a measurement of $\hat{X}$ on an observable $\hat{A}$ is modelled by adding the following term to the master equation[87]

$$\mathrm{d}\langle\hat{A}\rangle_{\mathrm{meas}} = \sqrt{\eta\mu}\langle\mathcal{H}[\hat{X}]\hat{A}\rangle\,\mathrm{d}W(t) \tag{3.16}$$

The measurement superoperator is

$$\mathcal{H}[\hat{X}]\hat{A} = \hat{X}\hat{A} + \hat{A}\hat{X}^\dagger - \langle\hat{X} + \hat{X}^\dagger\rangle\langle\hat{A}\rangle\ .$$

the expectation value of which is proportional to the covariance of $\hat{A}$ and $\hat{X}$. The interpretation of Eq. (3.16) is then that the observable $\langle\hat{A}\rangle$ is updated according to the measurement noise, scaled by an amount depending on the observable's correlation with $\hat{X}$ at that time. This carries the implicit assumption that the estimate is optimal. The observable $\hat{X}$, for example, evolves as

$$\mathrm{d}\langle\hat{X}\rangle_{\mathrm{meas}} = \sqrt{4\eta\mu}V_X(t)\mathrm{d}W(t) \tag{3.17}$$

This now resembles Equation (3.14), with the conditional variance V_X in the Kalman gain as expected. This simply states that if the conditional variance reduces over time, the observable must be updated with less noise over time. Substituting Equation 3.15, this evolution can be written in terms of the measurement record Q_X as

$$\mathrm{d}\langle\hat{X}\rangle_{\mathrm{meas}} = -4\eta\mu V_X(t)\langle\hat{X}\rangle + \sqrt{4\eta\mu}V_X(t)\mathrm{d}Q_X(t) \tag{3.18}$$

Here, a measurement-induced damping term is added to $U(t)$, the internal dynamics of $\hat{X}$. This accounts for the fact that $\mathrm{d}Q_X$ is distributed about the expected value of $\hat{X}$, as opposed to the residual noise $\mathrm{d}W(t)$ which is distributed about zero.

If the conditional variance $V_X(t)$ is known, Equation (3.18) can be solved to find an optimal filter for the measurement results. This variance can be found from the master equation, using the definition in Equation (3.5). Now the final term in Equation (3.5) becomes relevant, due to the Ito rule $(\mathrm{d}W)^2 = \mathrm{d}t$[84]. This leads to

$$\mathrm{d}V_{X,\mathrm{meas}}(t) = -4\eta\mu V_X^2(t)\mathrm{d}t \tag{3.19}$$

which looks like a nonlinear damping that increases with the measurement strength and efficiency. This is a standard result in control theory[20]. After including the internal dynamics and noise of the system, this variance may then be solved. Where there are no internal dynamics, the above equation has the solution $V_X \propto 1/t$, consistent with the example in Section 3.3.

So far, this still looks like a classical measurement as described in section 3.3. The quantum modification required in this picture is backaction noise, which exists independently of whether

the measurement is used at all. This is modelled by adding a thermal-like noise to the master equation (as in Section 3.2) proportional to the measurement rate μ. Putting together the backaction terms, dissipative terms and conditioning terms, we can now model the entire system for the specific cases of continuous position measurement and for backaction evasion.

3.5 Continuous position measurement of an oscillator

In this section and in following chapters, we assume a generalised position measurement that does not affect the mechanical susceptibility. We will, however, use cavity optomechanics as a simple prototypical system. In this case, a generalised position measurement is achieved by driving the cavity on resonance rather than on the red or blue sidebands. On resonance, the amplitude of the optical or microwave field is not modulated by small changes in the path length. Instead, it is here that the phase of the field is most sensitive. A sensitive phase measurement, such as a homodyne, can therefore be used to read out position fluctuations while not affecting the mechanical susceptibility.

If the optical decay is faster than the mechanical dissipation ($\kappa \gg \gamma$, where κ is the cavity linewidth), we can define the measurement rate μ as[46]

$$\mu = \frac{8g^2}{\kappa} , \tag{3.20}$$

where g is the optomechanical coupling rate. This is given by

$$g = Gx_{zpf}\sqrt{\bar{n}} \tag{3.21}$$

where G is the single-photon optomechanical coupling in Hz/m, $\bar{n} \gg 1$ is the mean photon number and $x_{zpf} = \sqrt{\hbar/m\omega_m}$ is the RMS position due to zero-point motion. This parameter μ can be interpreted as a coupling rate to a zero-temperature measurement bath, which can be compared with the coupling rate to the thermal bath γ. The ratio μ/γ is generally referred to as the co-operativity[88] which in addition to the temperature will be used to define the various measurement regimes, as will be discussed in the next section.

This kind of position measurement can be decomposed into quadratures. We will refer to the quadrature outputs (for example, from a lock-in amplifier with the position measurement as input) as $I_X(t)$ and $I_Y(t)$. We will limit our analysis to the regime $\mu \ll \omega_m$ in keeping with the rotating wave approximation. The resulting master equation then resembles the well-studied model of heterodyne detection used in optical and microwave systems[82]. Additionally, we assume the measurement signal has no thermal fluctuations. An observer's expected knowledge of the observable A then evolves as[87]

$$\begin{aligned} \mathrm{d}\langle\hat{A}\rangle = -\frac{i}{\hbar}\langle[\hat{A},\tilde{H}]\rangle\,\mathrm{d}t + [2\gamma N+\mu]\langle\mathcal{D}[\hat{a}^\dagger]\hat{A}\rangle\,\mathrm{d}t + [2\gamma(N+1)+\mu]\langle\mathcal{D}[\hat{a}]\hat{A}\rangle\,\mathrm{d}t \\ +\sqrt{\eta\mu}\langle\mathcal{H}[\hat{X}]\hat{A}\rangle\,\mathrm{d}W_1 + \sqrt{\eta\mu}\langle\mathcal{H}[\hat{Y}]\hat{A}\rangle\,\mathrm{d}W_2 \, . \end{aligned} \tag{3.22}$$

where $\mathrm{d}W_1$ and $\mathrm{d}W_2$ are uncorrelated Wiener increments. These correspond to the residual noise given the measurement results $dQ_X = I_X\,dt$ and $dQ_Y + I_Y\,dt$ so that[87]

$$\mathrm{d}W_1 = \mathrm{d}Q_X - \sqrt{4\eta\mu}\langle\hat{X}\rangle\mathrm{d}t \tag{3.23}$$

$$\mathrm{d}W_2 = \mathrm{d}Q_Y - \sqrt{4\eta\mu}\langle\hat{Y}\rangle\mathrm{d}t\ . \tag{3.24}$$

The backaction Lindblad terms in Eq. (3.22) take the form of an increased temperature, which can be written as an additional mean phonon occupation

$$N_{\mathrm{BA}} = \frac{\mu}{2\gamma} \tag{3.25}$$

For $\hat{H} = 0$, both quadratures behave identically. The conditional mean value equation now has additional terms representing the residual noise

$$\mathrm{d}\langle\hat{X}\rangle = -\gamma\langle\hat{X}\rangle\,\mathrm{d}t + \sqrt{4\eta\mu}V_X\,\mathrm{d}W_1 + \sqrt{4\eta\mu}C\,\mathrm{d}W_2 \tag{3.26}$$

$$\mathrm{d}\langle\hat{Y}\rangle = -\gamma\langle\hat{Y}\rangle\,\mathrm{d}t + \sqrt{4\eta\mu}V_Y\,\mathrm{d}W_2 + \sqrt{4\eta\mu}C\,\mathrm{d}W_1\ . \tag{3.27}$$

Notice that both equations contain both Wiener increments in the case of nonzero covariance C.

The equations for the conditional variances are found again using Equations (3.5-3.5), making use of the Ito rule to obtain

$$\frac{d}{dt}V_X = -2\gamma V_X + 2\gamma(N + 1/2 + N_{\mathrm{BA}}) - 4\eta\mu(V_X^2 + C^2) \tag{3.28}$$

$$\frac{d}{dt}V_Y = -2\gamma V_Y + 2\gamma(N + 1/2 + N_{\mathrm{BA}}) - 4\eta\mu(V_Y^2 + C^2) \tag{3.29}$$

$$\frac{d}{dt}C = -2\gamma C - 4\eta\mu C(V_X + V_Y)\ , \tag{3.30}$$

If the covariance is initially zero, it will remain so, simplifying the above to

$$\frac{d}{dt}V_X = -2\gamma V_X + 2\gamma(N + 1/2 + N_{\mathrm{BA}}) - 4\eta\mu V_X^2 \tag{3.31}$$

and similarly for Y. The effect of the measurement is therefore a backaction term proportional to μ, and a conditioning term in the form of a nonlinear damping of the variance. This is a well-known equation in classical control theory[20]. The backaction term here is the only modification required for validity in the quantum regime.

Initially — that is, when measurement begins — the conditional variances depend on an assumption about the system. In most cases, this will be that the system is in thermal equilibrium. Once measurement is turned on, the conditioning should reduce the variances until a new equilibrium is reached. Taking the steady-state condition $\mathrm{d}V_X = \mathrm{d}V_Y = 0$ and solving the resulting quadratic equations, we get $V_X = V_Y = V_0$ where

$$V_0 = \frac{-\gamma + \sqrt{\gamma^2 + 4\gamma\eta\mu(2N + 1 + N_{\mathrm{BA}})}}{4\eta\mu} \tag{3.32}$$

This is a monotonically decreasing function of μ, as expected. In other words, a stronger measurement conditionally cools the oscillator to a lower effective temperature, even when backaction is taken into account. Here we can define a ratio of mechanical signal to measurement shot-noise

$$\mathrm{SNR} = 2V_T\eta\mu/\gamma \tag{3.33}$$

where the unconditional variance V_T quantifies the unfiltered thermal noise and backaction

$$V_T = N + N_{\mathrm{BA}} + 1/2 \tag{3.34}$$

In the classical regime of large N, the SNR can be thought of as the ratio of mean-square thermal displacement $(\delta x_T)^2$ to $(\delta x_\gamma)^2$ the square of the minimum distance resolvable over a time $\Delta t \approx 1/(4\gamma)$[82]. For a shot-noise limited measurement, the SNR is therefore proportional to the factor by which the mechanical peak exceeds the white noise floor, as is easily measured by a spectrum analyser.

Eq. (3.32) can now be rewritten as

$$\frac{V_0}{V_T} = \frac{\sqrt{1+4\mathrm{SNR}}-1}{2\mathrm{SNR}} \tag{3.35}$$

Taking the limit $\mathrm{SNR} \ll 1$ in Eq. (3.35) produces the bad measurement regime, which can be due to either weak coupling or inefficient detection of the signal post-interaction. In this limit, V_0 reduces to the unconditional variance V_T as expected.

As SNR increases past unity so that $1/(2\eta V_T) < \mu/\gamma < 2V_T$, the thermal noise can be well resolved and the conditional variance reduces towards the ground state. When $\mu/\gamma \gg 2V_T$, the back-action in SNR (proportional to $(\mu/\gamma)^2$) dominates and the strong measurement limit is approached

$$V_0(\mathrm{SNR} \to \infty) = 1/(2\sqrt{\eta}) \tag{3.36}$$

So for perfect efficiency, backaction prevents a conditional variance below the ground state variance of 1/2, as expected. Note that when $2V_T = \eta = 1$, the second regime (i.e. classical measurement) disappears entirely.

3.5.1 Optimal filter

The conditional variances derived above characterise the error in the optimal estimate of the position as a function of the measurement and thermal noises. If the optimal estimate is used for feedback cooling, these variances would characterise the actual noise in the oscillator, which can be confirmed by an independent measurement[67]. When using the proper stochastic master equation, this principle is general to quantum and classical systems[89]. Even without feedback, the conditional variances quantify an observer's subjective knowledge of the position, which holds significance in quantum mechanics. Namely, in the limit that the conditional variance of $\hat{X}$ approaches zero, the effect of the measurement alone according to an observer is to project the oscillator into an eigenstate of $\hat{X}$.

In any practical setting, the conditional variance is meaningless without being able to calculate this estimate from the measurement record. For example, feedback cooling requires an estimate to be generated in real time to control a proportional force. In the case of continuous position measurement of a high-Q oscillator, the estimate takes on a simple form. In the limit of a perfect measurement, the optimal estimate at time t would simply be identical to the measurement record at time t. If there is measurement noise, however, a filter must be applied to make use of previous results and the memory of the oscillator. This filter is identical for both quadratures of motion.

The X quadrature estimate X_{est} can be found by rewriting the expectation value $\langle \hat{X} \rangle$ in terms of the measurement record $Q_X(t)$. Substituting the white noise residual, given by Eq. (3.23) into the mean value evolution, given by Eq. (3.26) with $C = 0$

$$\mathrm{d}\langle \hat{X} \rangle(t) = -(\gamma + 4\eta\mu V_X)\langle \hat{X} \rangle(t)\,\mathrm{d}t + \sqrt{4\eta\mu} V_X\,\mathrm{d}Q_X(t) \tag{3.37}$$

Here, the evolution of the expectation value of $X(t)$ is given in terms of the evolution of the measurement record $Q_X(t)$, rather than the white noise residual $W_1(t)$. This is compensated by adding an effective damping term to the expectation value. Substituting the solution Eq. (3.32) for V_X into its first instance leads to the simple result

$$\mathrm{d}\langle \hat{X} \rangle(t) = -\gamma\sqrt{1 + 4\mathrm{SNR}}\langle \hat{X} \rangle(t)\,\mathrm{d}t + \sqrt{4\eta\mu} V_X\,\mathrm{d}Q_X(t) \tag{3.38}$$

The above is a simple updating rule for the expectation value of X over one time increment. The damping term, which increases with SNR, has the effect of erasing previous measurement results after some amount of time that decreases with SNR. The current estimate at time t in terms of the current and previous increments can be found by solving this differential equation. This results in a filter of the same form as Eq. (3.13), namely

$$\langle X_{est}(t) \rangle = \sqrt{4\eta\mu} V_X \int_0^t e^{-\Gamma(t-\tau)} \mathrm{d}Q_X(\tau)\ . \tag{3.39}$$

where

$$\Gamma = \gamma\sqrt{1 + 4\mathrm{SNR}} \tag{3.40}$$

is the filter bandwidth. This matches the oscillator linewidth for low SNR, making full use of the memory of the oscillator. The filter begins to widen as SNR approaches unity, where the thermal noise is resolved above the measurement noise.

As expected, the filter makes the most use of recent measurements and drops off exponentially for previous results. Alternatively, this filter can be written as a convolution

$$\langle X_{est}(t) \rangle = \sqrt{4\eta\mu} V_X (Q_X(t) * e^{-\Gamma t})\ , \tag{3.41}$$

Notably, at zero temperature and with perfect efficiency the bandwidth simplifies to

$$\Gamma = \gamma + 2\mu\ . \tag{3.42}$$

3.6 Backaction evasion

The most common backaction evading techniques involve making position measurements that are essentially periodic. In an optomechanical system, this can be achieved in the good-cavity limit where $\omega_m \gg \kappa$ by sideband driving on both sides of the resonance. This technique effectively modulates the intensity at $2\omega_m$ and hence produces a stroboscopic interaction with one position quadrature. Using this method, by which the backaction only heats the unmeasured quadrature, it follows that an arbitrarily sensitive measurement of the measured quadrature is possible. This technique, first theoretically developed by Braginsky et al.[36], is the prototypical quantum non-demolition (QND) measurement of an oscillator — since joined by QND protocols for energy[41] and atomic spin[90].

The conditional variances of a mechanical oscillator under backaction evasion have been recently studied using a master equation formalism[46]. Here, we will reproduce this theory using the same parameters as defined above for a continuous position measurement. This will then allow a direct comparison between parametric amplification and backaction evasion in Chapter 6.

The master equation can be written

$$\begin{aligned} \mathrm{d}\langle\hat{A}\rangle = &-\frac{i}{\hbar}\langle[\hat{A},\tilde{H}]\rangle\,\mathrm{d}t + 2\gamma\mathcal{D}[\hat{a}]\hat{A}\rangle\,\mathrm{d}t + \sqrt{\eta\mu}\langle\mathcal{H}[\hat{X}]\hat{A}\rangle\,\mathrm{d}W_1 \\ &+2\gamma(N+N_{\mathrm{BA}})\langle\mathcal{D}[\hat{X}]\hat{A}\rangle\,\mathrm{d}t + 2\gamma(N+N_{\mathrm{bad}})\langle\mathcal{D}[\hat{Y}]\hat{A}\rangle\,\mathrm{d}t\ , \end{aligned} \tag{3.43}$$

where N_{BA} is defined as above, and $N_{\mathrm{bad}} < N_{\mathrm{BA}}$ is the spurious backaction heating of the $\hat{X}$ quadrature due to imperfect QND measurement. This is a function of the cavity linewidth κ and the measurement strength. In the resolved sideband regime, where $\kappa \ll \omega_m$, this is approximated to first order as[46]

$$N_{\mathrm{bad}} = \frac{N_{\mathrm{BA}}}{32}\left(\frac{\kappa}{\omega_m}\right)^2\ . \tag{3.44}$$

In the ideal good-cavity limit, $N_{\mathrm{bad}} = 0$ and there is no backaction heating of the measured $\hat{X}$ quadrature.

Computing the variance equations from the master equation gives

$$\frac{d}{dt}V_X = -2\gamma V_X + 2\gamma(N+1/2+N_{\mathrm{bad}}) - 4\eta\mu V_X^2 \tag{3.45}$$

$$\frac{d}{dt}V_Y = -2\gamma V_Y + 2\gamma(N+1/2+N_{\mathrm{BA}}) - 4\eta\mu C^2 \tag{3.46}$$

$$\frac{d}{dt}C = -2\gamma C - 4\eta\mu V_X C\ , \tag{3.47}$$

One can easily verify from Eq. (3.47) that the stationary conditional state has $C = 0$. The solutions for the conditional variances are then

$$V_X = \frac{-\gamma + \sqrt{\gamma^2 + 4\gamma\eta\mu(2N+2N_{\mathrm{bad}}+1)}}{4\eta\mu} \tag{3.48}$$

$$V_Y = N + N_{\mathrm{BA}} + 1/2 = V_T \tag{3.49}$$

The solution for V_X is the same as Eq. (3.32) describing a continuous measurement, but with a reduced backaction term. This allows V_X to be squeezed below the ground-state variance at the expense of extra noise in V_Y, which is unconditioned and hence increases monotonically with μ.

Since $N_{\rm bad}$ is (like $N_{\rm BA}$) a linearly increasing function of μ, this term sets the lower limit to V_X in the strong measurement limit

$$V_X(\mu \to \infty) = \frac{\sqrt{N_{\rm bad}/N_{\rm BA}}}{2\eta} \tag{3.50}$$

Therefore, quantum squeezing is possible for an efficient and strong backaction-evading measurement in the good-cavity regime. Achieving all of these requirements at once is still experimentally difficult, owing primarily to measurement-induced instability as a limit to the measurement rateμ[91]. The next chapter will introduce an alternative to backaction evasion, while Chapter 6 will examine the possibility of quantum squeezing using only a weak measurement.

Chapter 4

Detuned mechanical parametric amplification with classical measurement

4.1 Introduction

Until now we have only considered one way in which oscillators can be excited. That is, by applying direct, external forces. For example, a mother can excite a swing (and accordingly, her child) by pushing her feet against the ground, accelerating the child's mass into the air. However, as every child knows, the mass can take over after one initial push. How can this happen without needing to make contact with the ground?

The motions of a child aiming to go higher on a swing are, despite their intuitive simplicity, a performance of nonlinear mechanics. The energy does not enter the system from a direct force, but from the upward and downward shifting of the centre of the mass. Such a *parametric modulation* can be used to increase the harmonic restoring force when it aids the existing oscillation (that is, when moving toward the midpoint) and to decrease it when it does not (when moving away). This modulation at twice the resonance frequency is the first-order method of parametric amplification.

This technique is general to any harmonic oscillator. Notably, it has found widespread practical use in quantum optics[92, 93] before it did in mechanical systems, where until recently it had remained a curiosity. In optics, the time-dependent parameter is generally the polarisability of a dielectric crystal, modulated by a strong "pump" laser of twice the frequency of the output signal beams. This kind of amplification can be applied to intracavity modes or to the non-equilibrium case of travelling waves, the former being more analogous to the damped mechanical oscillators we are studying.

A landmark paper by Rugar and Grütter[25] introduced parametric amplification to MEMS oscillators by using a highly nonuniform electric field, a method which is still widely imple-

mented in dielectric resonators[94, 95, 60]. In this case, an effective spring constant arises due to the spatial dependence of the force F_{ext} from the electric field.

$$k_{\text{eff}} = k_0 + dF_{\text{ext}}/dx \tag{4.1}$$

Modulating this force at twice the resonance frequency will not excite a high-Q oscillator directly due to the low susceptibility at this frequency. Instead, due to the nonzero dF_{ext}/dx, this provides the required modulation of the spring constant for self-amplification. Other common parametric techniques in MEMS and NEMS involve piezoelectric strain[56], dispersive coupling to charge qubits[24] and Duffing nonlinearities[57]. In the context of electromechanics, this amplification is generally used to circumvent measurement noise.

Parametric amplification has also seen recent application in superconducting microwave resonators, where the nonlinear inductance of Josephson junctions[23, 96] or the resonators themselves[97] can be used to modulate the resonance frequency. Such methods are useful to amplify quantum signals above substantial thermal and measurement noises, which are problematic at microwave frequencies.

4.2 Amplification, squeezing and threshold

Returning to the child-on-a-swing analogy, the amplification we described requires the modulation to have the correct timing with respect to the motion. If the modulation were to be reversed (i.e. the restoring force is increased when moving out from the centre), there would instead be a damping of motion. In other words, the amplification is phase-sensitive. In the presence of random fluctuations, a resonant parametric drive decreases the damping of fluctuations that are in-phase with the drive, and increases the damping for those that are out-of-phase.

In Section 2.3, resonant parametric modulation was shown to break the quadrature symmetry of the zero-point motion, resulting in a squeezed state. This chapter will deal with the similar effect on the thermal noise described in Section 3.2. Adding the influence of the parametric drive given by Eqs (2.42-2.43) to the intrinsic decay and adding input noise X_{in} and Y_{in} results in Langevin equations

$$\mathrm{d}X = -(\gamma + \chi)X\,\mathrm{d}t + \sqrt{2\gamma}\mathrm{d}X_{\text{in}}(t) \tag{4.2}$$

$$\mathrm{d}Y = -(\gamma - \chi)Y\,\mathrm{d}t + \sqrt{2\gamma}\mathrm{d}Y_{\text{in}}(t) \tag{4.3}$$

where χ, as defined in Section 2.3, characterises the strength of the parametric drive. For $\chi < \gamma$, there is an increased effective damping rate for X and a decreased rate for Y. When visualised in quadrature phase space, the resulting equilibrium probability distribution is elliptical, which we will call a "classically squeezed" distribution. This prediction was confirmed experimentally by Rugar and Grütter for the thermal noise of a MEMS cantilever[25].

If the drive strength χ is increased, the squeezing becomes more pronounced, ultimately reaching a threshold where the amplified quadrature's damping becomes negative ($\chi > \gamma$)

and the oscillator becomes unstable. Specifically, the amplitude grows exponentially before encountering an intrinsic limiting nonlinearity. This non-equilibrium phenomenon, known as parametric resonance, exhibits interesting features such as bistability[94]. Just below threshold, the damping of the orthogonal quadrature is double its original value, limiting steady-state squeezing of the variance to 3dB for a time-domain average.

For $\chi < \gamma$, these quadrature equations of motion can then be transformed to the frequency domain and squared, giving the power spectral density as a Lorentzian filter of the input noises

$$\langle X^2(\omega)\rangle = \frac{2\gamma\langle X_{\rm in}^2(\omega)\rangle}{(\gamma+\chi)^2+\omega^2} \tag{4.4}$$

$$\langle Y^2(\omega)\rangle = \frac{2\gamma\langle Y_{\rm in}^2(\omega)\rangle}{(\gamma-\chi)^2+\omega^2} \tag{4.5}$$

Clearly, as the drive strength approaches threshold ($\chi \to \gamma$) the spectral density of the X quadrature at resonance is reduced by a factor of four compared to with the drive off. Steady-state squeezing close to this amount has been reported in the MEMS literature[25, 24] and in intracavity optical parametric amplifiers[98], since in all cases this squeezing was measured using only frequency components of the motion near the resonance. We will be working in the time domain, for which the variance is effectively an integral over all frequency components. Assuming the input noise is white, this is simply proportional to the integral of the Lorentzian susceptibility. However, since this integral scales linearly with the effective linewidth $\gamma + \chi$, this time-domain variance only sees a maximum steady-state squeezing by a factor of two.

By virtue of the squeezing effect, parametric amplification has been used for preparation of quantum squeezed states in atomic traps[7] and proposed for mechanical oscillators[26]. However, for squeezing below the quantum level to be possible in the steady-state, the 3dB limit requires the thermal occupation to be less than the zero-point motion, implying that the mean phonon occupation $N < 1/2$. To date, this condition has only been achieved using very high frequency oscillators[99] or by using state-of-the-art optomechanical cooling techniques[43, 40]. Furthermore, since cooling to below the bath temperature decreases the effective Q-factor, a stronger parametric drive would be required to reach threshold in most cases.

In the context of steady-state parametric amplification, recent work published after the work in this thesis has shown that the 3dB limit can be surpassed by using active[100] or passive[101] cooling to stabilise the amplified quadrature. Even in these cases, work to date on parametric amplification has generally focused on the resonant modulation at $2\omega_m$ shown above. Resonant parametric modulation is typically considered useful for either amplification or squeezing in isolation, for the purposes of enhanced measurement or state preparation respectively. In the remainder of this chapter, we will focus on the intersection of these two ideas. That is, using the increased measurement fidelity of the amplified quadrature in order to enhance the squeezing of the other without the use of a stabilisation technique. For this, we will need to derive a full model that includes detuning of the parametric drive away from resonance. While the detuned regime has been treated in optics, where non-equilibrium squeezing is applied to travelling

waves[102], the work in this chapter is the first known analysis for a damped and monitored oscillator in the steady-state.

4.3 Hamiltonian

The Hamiltonian for a resonant parametric drive (that is, at twice the frequency ω_m) is given by Eq. (2.35), which is followed by a transformation into the rotating frame. Only a simple modification is required to add detuning to this model. Suppose that the spring constant is modulated at a frequency $2\omega_d$, where $\omega_d = \omega_m - \Delta$. The full Hamiltonian is then

$$\begin{aligned} \tilde{H} &= \frac{\tilde{p}^2}{2m} + \frac{\tilde{x}^2}{2}[k_0 - k_r \sin(\omega_d t + 2\theta)] && (4.6) \\ &= \hbar\omega_m(\tilde{a}^\dagger\tilde{a} + 1/2) - \hbar\chi(\tilde{a} + \tilde{a}^\dagger)^2 \sin(2\omega_d t + 2\theta) && (4.7) \end{aligned}$$

where as before $\chi = \omega_m k_r/(4k_0)$ is approximately the peak-to-peak frequency modulation. Note that this modulation is completely classical and noiseless, assuming technical noise can be neglected. This differs from coupled harmonic modes, for example, where quantum noise is introduced by the second mode.

For a high-Q oscillator, we can instead use as co-ordinates the quadratures $\hat{X}$ and $\hat{Y}$. In contrast to equation (2.16), we will make the rotating wave approximation at the frequency ω_d, so that the squeezing operation is stationary. This is done by separating the Hamiltonian into parts $\tilde{H}_0$ and $\tilde{H}_I$ where

$$\tilde{H}_0 = \hbar\omega_d(\tilde{a}^\dagger\tilde{a} + 1/2) \tag{4.8}$$

and

$$\tilde{H}_I = \hbar\Delta(\tilde{a}^\dagger\tilde{a} + 1/2) - \hbar\chi(\tilde{a} + \tilde{a}^\dagger)^2 \sin(\omega_d t + 2\theta) \tag{4.9}$$

In this case, the interaction Hamiltonian is transformed by making the substitution

$$\tilde{a} \to \hat{a}\exp(-i\omega_d t) \tag{4.10}$$

This has no effect on the term proportional to Δ, and transforms the modulation term into a squeezing operator. The Hamiltonian can then be written

$$\hat{H} = \hbar\Delta\hat{a}^\dagger\hat{a} + i\hbar\frac{\chi}{2}(e^{2i\theta}\hat{a}^2 - e^{-2i\theta}\hat{a}^{\dagger 2}) \, . \tag{4.11}$$

Since we chose a rotating frame with respect to the parametric drive, this Hamiltonian looks like a resonance at Δ with a stationary squeezing operator. Now in addition to χ, the detuning Δ must also be much less than ω_d for the rotating wave approximation to hold. Note that the phase θ has no effect on the system dynamics but defines the squeezing axes with respect to the chosen quadratures.

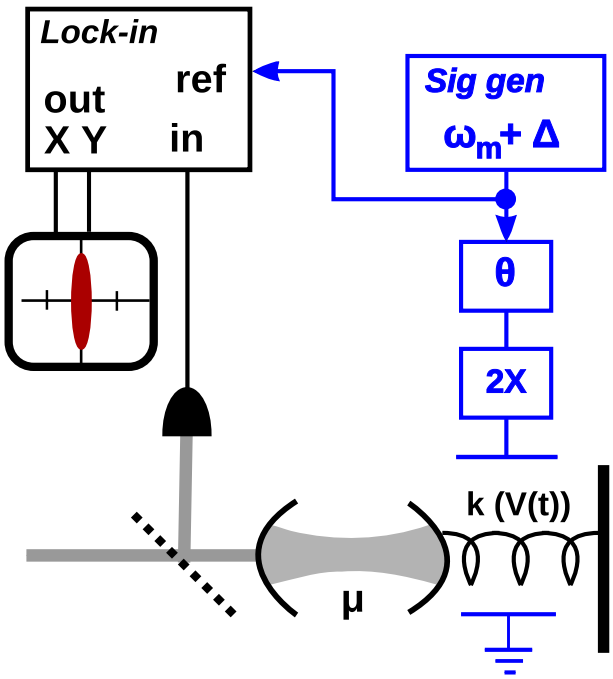

Figure 4.1: Idealised schematic of a parametric drive applied to an optomechanical system. The quadratures analysed in this chapter can be obtained by feeding a continuous position measurement into a lock-in amplifier with reference frequency ω_d.

4.4 Evolution of observables

Applying the master equation for continuous measurement introduced in Section 3.5 to the quadratures X and Y with the above Hamiltonian gives the time domain evolution of the expectation values

$$\mathrm{d}\langle\hat{X}\rangle = [-(\gamma+\chi\cos 2\theta)\langle\hat{X}\rangle-(\Delta-\chi\sin 2\theta)\langle\hat{Y}\rangle]\mathrm{d}t+\sqrt{4\eta\mu}V_X\,\mathrm{d}W_1+\sqrt{4\eta\mu}C\,\mathrm{d}W_2 \quad (4.12)$$

$$\mathrm{d}\langle\hat{Y}\rangle = [-(\gamma-\chi\cos 2\theta)\langle\hat{Y}\rangle+(\Delta+\chi\sin 2\theta)\langle\hat{X}\rangle]\mathrm{d}t+\sqrt{4\eta\mu}C\,\mathrm{d}W_1+\sqrt{4\eta\mu}V_Y\,\mathrm{d}W_2 \quad (4.13)$$

Let us for now assume that the position is not localised through filtering the measurement results by setting $\mu = 0$. Additionally setting $\Delta = \theta = 0$, this reproduces Eqs (4.2-4.3) describing the familiar resonant parametric amplification. That is, an additional damping in X and reduced damping in Y, both proportional to the drive strength χ.

The resonant case is restricted by the threshold requirement $\chi < \gamma$. In general, however, the system is stable if χ is below a threshold value

$$\chi_{th} = \sqrt{\Delta^2+\gamma^2}\,. \quad (4.14)$$

This shows that by introducing a dynamical coupling between amplified and damped quadratures, the detuning enables a stronger parametric drive without self-oscillation. For $|\chi| < |\Delta|$,

the oscillator's trajectories through X-Y phase space are elliptical

$$\langle \hat{X}(t) \rangle = \left[X(0)\cos(\omega_e t) + Y(0)\sqrt{\frac{\Delta-\chi}{\Delta+\chi}}\sin(\omega_e t) \right] e^{-\gamma t} \tag{4.15}$$

$$\langle \hat{Y}(t) \rangle = \left[Y(0)\cos(\omega_e t) - X(0)\sqrt{\frac{\Delta+\chi}{\Delta-\chi}}\sin(\omega_e t) \right] e^{-\gamma t} \tag{4.16}$$

with frequency

$$\omega_e = \sqrt{\Delta^2 - \chi^2}\,. \tag{4.17}$$

4.4.1 QND-like evolution

Detuning closer to threshold, the elliptical trajectories become slower and the amplification becomes more pronounced. In the case that $\chi_{th} > |\chi| > |\Delta|$, the frequency ω_e becomes imaginary and the above trajectories are given by damped hyperbolic functions. The intermediate special case $|\Delta| = |\chi|$ is notable, since here one quadrature is unaffected by the drive. For example, when $\Delta = -\chi$ and $\theta = \pi/4$, the equations of motion are

$$\mathrm{d}\langle \hat{X} \rangle = -\gamma \langle \hat{X} \rangle \mathrm{d}t \tag{4.18}$$

$$\mathrm{d}\langle \hat{Y} \rangle = [-\gamma \langle \hat{Y} \rangle + 2\chi \langle \hat{X} \rangle]\mathrm{d}t \tag{4.19}$$

In this case, the squeezing and rotation operations conspire to produce simple coherent dynamics analogous to that of a free particle: similar to momentum, the $\hat{X}$ quadrature is a constant of the motion, while similar to position, $\hat{Y}$ grows at a rate determined by $\hat{X}$. That is, in the absence of external influences, $(d/dt)\hat{Y} = \chi\hat{X}$. It follows trivially that while the $\hat{X}$ quadrature is unaffected by the parametric driving, at long times (or low frequencies) the $\hat{Y}$ quadrature becomes an amplified version of $\hat{X}$. This can be seen from the quantum Langevin equations, which take the form

$$\begin{bmatrix} \mathrm{d}\hat{X} \\ \mathrm{d}\hat{Y} \end{bmatrix} = \begin{bmatrix} -\gamma & 0 \\ \chi & -\gamma \end{bmatrix} \begin{bmatrix} \hat{X} \\ \hat{Y} \end{bmatrix} \mathrm{d}t + \sqrt{2\gamma} \begin{bmatrix} \mathrm{d}\hat{X}_{\mathrm{in}} \\ \mathrm{d}\hat{Y}_{\mathrm{in}} \end{bmatrix}\,, \tag{4.20}$$

where $X_{\mathrm{in}}, Y_{\mathrm{in}}$ describe the input noise from the mechanical bath. The above is easily solved in the frequency domain as

$$\hat{X}(\omega) = \hat{X}_0(\omega) \tag{4.21}$$

$$\hat{Y}(\omega) = \hat{Y}_0(\omega) + \frac{2\chi}{\gamma - i\omega}\hat{X}_0(\omega)\,, \tag{4.22}$$

where

$$\hat{X}_0(\omega) = \frac{\hat{X}_{\mathrm{in}}}{\gamma - i\omega} \tag{4.23}$$

$$\hat{Y}_0(\omega) = \frac{\hat{Y}_{\mathrm{in}}}{\gamma - i\omega} \tag{4.24}$$

are the mechanical quadratures when $\chi = 0$.

For low frequencies and large χ/γ, the detuned parametric drive causes $\hat{Y}$ to become an amplified version of $\hat{X}$, whereas $\hat{X}$ is completely unaffected by the parametric driving. The situation is reminiscent of a quantum non-demolition measurement: the mechanical $\hat{Y}$ quadrature "measures" the $\hat{X}$ quadrature, without any backaction disturbance. This concept will be examined further in Section 6.3.

4.5 Unconditional steady-state

It has already been shown that in the presence of a below-threshold detuned parametric drive, a coherent excitation of an oscillator will follow an asymmetric trajectory to the origin in our chosen quadrature phase space. This influence applies in a similar way to the thermal noise. That is, the unconditional covariance matrix will evolve towards an asymmetric steady-state. The differential equations for these variances can be found from the master equation with the condition $\mu = 0$, producing

$$\frac{d}{dt}V_X = -2(\gamma+\chi\cos(2\theta))V_X - 2(\Delta-\chi\sin(2\theta))C + 2\gamma V_T \tag{4.25}$$

$$\frac{d}{dt}V_Y = -2(\gamma-\chi\cos(2\theta))V_Y + 2(\Delta+\chi\sin(2\theta))C + 2\gamma V_T \tag{4.26}$$

$$\frac{d}{dt}C = -2\gamma C - \Delta(V_Y-V_X) + \chi\sin(2\theta)(V_X+V_Y)\,. \tag{4.27}$$

where $V_T = N + 1/2$. We will solve these equations in both the steady-state case where the variances are stationary and in the case of a step response to the parametric drive.

Setting the left hand sides of Eqs (4.25-4.27) to zero results in the unconditional steady-state variance, which would be inferred from a spectrum analysis over a time much longer than any time scales in the dynamics. Applying detuning shifts the angle of the squeezing axes significantly compared to the resonant case. In anticipation of this we set $\theta = \pi/4$, which without detuning will amplify fluctuations maximally along an axis rotated through an angle $\pi/4$ from the Y quadrature (Note: this will henceforth be called the *antisqueezing angle*). Solving Eqs (4.25-4.27) with these conditions results in

$$V_{Xss} = \left(1 - \frac{\chi(\Delta-\chi)}{\gamma^2+\Delta^2-\chi^2}\right) V_T \tag{4.28}$$

$$V_{Yss} = \left(1 + \frac{\chi(\Delta+\chi)}{\gamma^2+\Delta^2-\chi^2}\right) V_T \tag{4.29}$$

$$C_{ss} = \frac{\chi\gamma}{\gamma^2+\Delta^2-\chi^2}\, V_T\,. \tag{4.30}$$

Interestingly, by going to the near-threshold detuning $\Delta = \chi \gg \gamma$, the antisqueezing axis is close to Y as it would be for $\theta = \Delta = 0$, while the X variance is unaffected.

The exact squeezing is characterized by finding the quadrature in the $X-Y$ plane with the smallest variance. Defining an arbitrary quadrature

$$\hat{X}_\alpha = \hat{X}\cos\alpha - \hat{Y}\sin\alpha \tag{4.31}$$

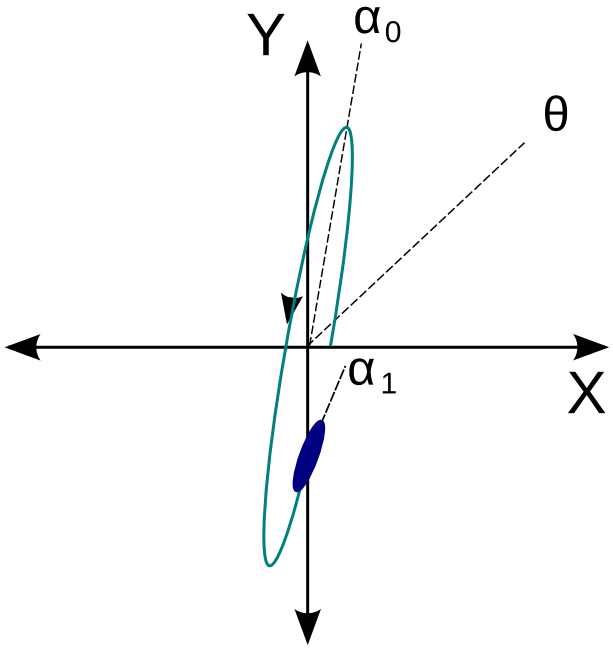

Figure 4.2: Illustration of an unconditional trajectory in X-Y phase space with a conditional uncertainty at a given time based on previous measurements (shaded ellipse). The angles $\theta = \pi/4$, α_0 and α_1 are defined between the Y axis and respective dotted lines.

so that

$$V_{X\alpha} = V_X \cos^2\alpha + V_Y \sin^2\alpha - 2C\cos\alpha\sin\alpha\ . \tag{4.32}$$

the maximally squeezed variance and its angle can be found by differentiating V_α with respect to α. As long as $V_Y > V_X$, the maximally squeezed and antisqueezed quadratures (V_- and V_+ respectively) become

$$V_- = \frac{1}{2}[(V_X + V_Y) - (V_Y - V_X)\sec(2\alpha_0)] \tag{4.33}$$

$$V_+ = \frac{1}{2}[(V_X + V_Y) + (V_Y - V_X)\sec(2\alpha_0)] \tag{4.34}$$

where

$$\alpha_0 = \frac{1}{2}\tan^{-1}\left(\frac{2C(t)}{V_Y(t) - V_X(t)}\right)\ , \tag{4.35}$$

is the antisqueezing angle (see Figure 4.2). Applying this to the steady-state solutions given by Eqs (4.28-4.30) results in

$$V_{\mathrm{ss}-} = \frac{V_T}{1 + \chi/\chi_{\mathrm{th}}} \tag{4.36}$$

$$V_{\mathrm{ss}+} = \frac{V_T}{1 - \chi/\chi_{\mathrm{th}}} \tag{4.37}$$

$$\alpha_{0ss} = \frac{1}{2}\tan^{-1}(\frac{\gamma}{\Delta})\ , \tag{4.38}$$

where the threshold value χ_{th}, given by Eq. (4.14) defines the maximum drive strength before the system self-oscillates. Therefore, for both detuned and resonant drives, a maximum unconditional squeezing V_-/V_T of -3dB can be achieved in the time-domain.

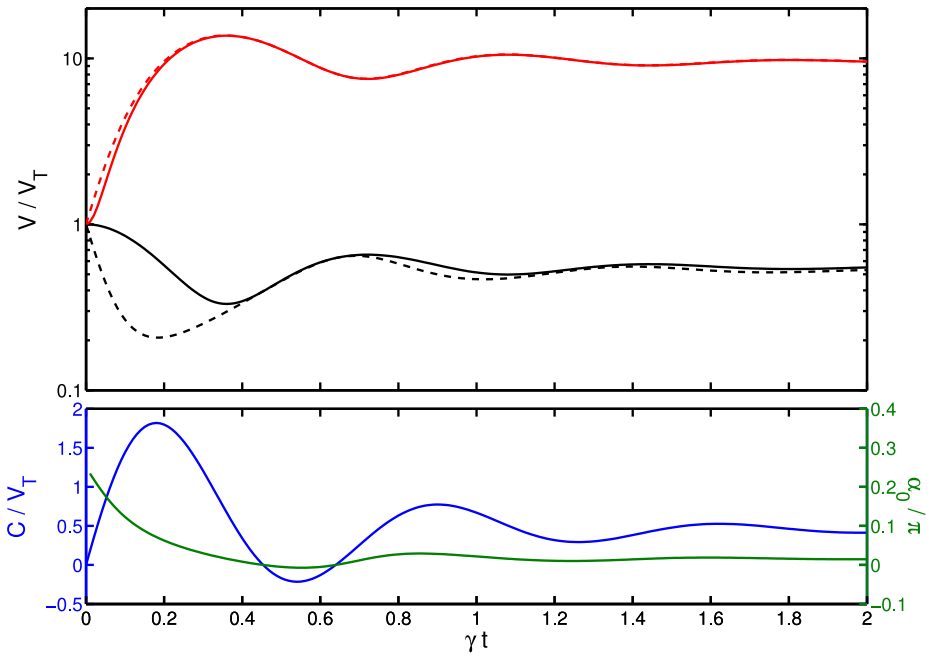

Figure 4.3: Step response of unconditional variances for $\Delta' = 10$ and $\chi' = 9$, where the pump is switched on at $t = 0$. Above: Normalised variances for the X and Y quadratures (solid) and actual squeezed and antisqueezed quadratures (dotted) vs time. Below: Covariance and squeezing angle vs time.

It is interesting to note that the parameter χ/χ_{th} in general defines the amount of squeezing and antisqueezing. Unlike the resonant case where $\chi_{\text{th}} = \gamma$, in the highly detuned case $\chi_{\text{th}} \approx \Delta$. Therefore, when near threshold in the detuned case, the antisqueezed variance becomes extremely sensitive to the frequency difference between the oscillator and the drive. For this reason, detuned parametric amplification has been investigated in the context of precision frequency sensing[103].

4.6 Unconditional transient variance

We can also consider the transient evolution of the variance from a symmetric thermal state to the asymmetric steady-state value after a sudden turn-on of the parametric drive. In an experiment, this time-evolution can be found by repeating the drive turn-on from the same condition and calculating the variance $V(t)$ over many runs for each time t. Differentiating both sides of Eq. (4.27) with respect to time for $\eta = 0$ and $\theta = \pi/4$ leads to a second-order equation similar to Eq. (1.4) describing a damped harmonic oscillator with a constant applied force

$$\frac{\partial^2 C}{\partial t^2} + 4\gamma \frac{\partial C}{\partial t} + 4(\Delta^2 + \gamma^2 - \chi^2)C = 4\chi\gamma V_T \tag{4.39}$$

If the pump is turned on at $t = 0$ (where $C = 0$ for $t < 0$), the analytic solution to Eq.

(4.39) is

$$C(t) = C_{ss}\left(1 - \frac{\cos(2\omega_p t + \phi)}{\cos(\phi)} e^{-2\gamma t}\right) \tag{4.40}$$

where

$$\phi = \left|\cos^{-1}\left(\frac{\gamma}{\sqrt{\Delta^2 + \gamma^2 - \chi^2}}\right)\right| . \tag{4.41}$$

In the regime $\Delta > \chi > \gamma$, the covariance takes the form of an underdamped step response with characteristic overshoot, as shown in Fig. 4.3. Substituting this solution into the X and Y variance equations, the time-dependent variances are:

$$V_X(t) = V_{Xss} + (V_T - V_{Xss})\frac{\sin(2\omega_p t + \phi)}{\sin(\phi)} e^{-2\gamma t} \tag{4.42}$$

$$V_Y(t) = V_{Yss} + (V_T - V_{Yss})\frac{\sin(2\omega_p t + \phi)}{\sin(\phi)} e^{-2\gamma t} \tag{4.43}$$

This results in a simple expression for the squeezing angle α_0 as time evolves

$$\alpha_0(t) = \frac{1}{2}\tan^{-1}\ \frac{\gamma(1 - \frac{\cos(2\omega_p t+\phi)}{\cos\phi} e^{-2\gamma t})}{\Delta(1 - \frac{\sin(2\omega_p t+\phi)}{\sin\phi} e^{-2\gamma t})} \tag{4.44}$$

This begins at $\pi/4$, oscillates periodically about $\tan^{-1}(\gamma/\Delta)/2 = \alpha_{ss}$ and approaches the latter in the steady-state. As can be seen from Fig. 4.3, when following the maximally squeezed quadrature, the squeezing ratio easily surpasses the steady-state limit of one half in the early stage of the step response. At such short times, before the detuning takes effect, this behaviour resembles the exponentially growing and shrinking variances produced by an above-threshold resonant parametric drive. The difference in this case is that the variances are automatically constrained by the detuning at long times to their steady-state values.

4.7 Conditional steady-state

Now it will be demonstrated that if $\mu > 0$, unlike in the unconditional case, using a detuned parametric drive enables a much greater degree of squeezing in the steady-state compared to a resonant drive. This is because the squeezed quadrature can be inferred from previous measurements of the amplified quadrature. In order to generalise this idea to the classical and quantum regimes, the squeezing will first be examined relative to the bare conditional variance, as given in terms of SNR by Eq. (3.35). The defining feature of the quantum regime is the backaction term in the unconditional variance V_T, which is negligible when $\mu/\gamma \ll 2N+1$. The absolute variance in the quantum regime, where the backaction term needs to be taken into account, will be examined in Chapter 6. The full variance equations are

$$\frac{d}{dt}V_X = -2(\gamma+\chi\cos(2\theta))V_X - 2(\Delta-\chi\sin(2\theta))C + 2\gamma V_T - 4\eta\mu(V_X^2 + C^2) \tag{4.45}$$

$$\frac{d}{dt}V_Y = -2(\gamma-\chi\cos(2\theta))V_Y + 2(\Delta+\chi\sin(2\theta))C + 2\gamma V_T - 4\eta\mu(V_Y^2 + C^2) \tag{4.46}$$

$$\frac{d}{dt}C = -2\gamma C - \Delta(V_Y - V_X) + \chi\sin(2\theta)(V_X + V_Y) - 4\eta\mu C(V_X + V_Y) . \tag{4.47}$$

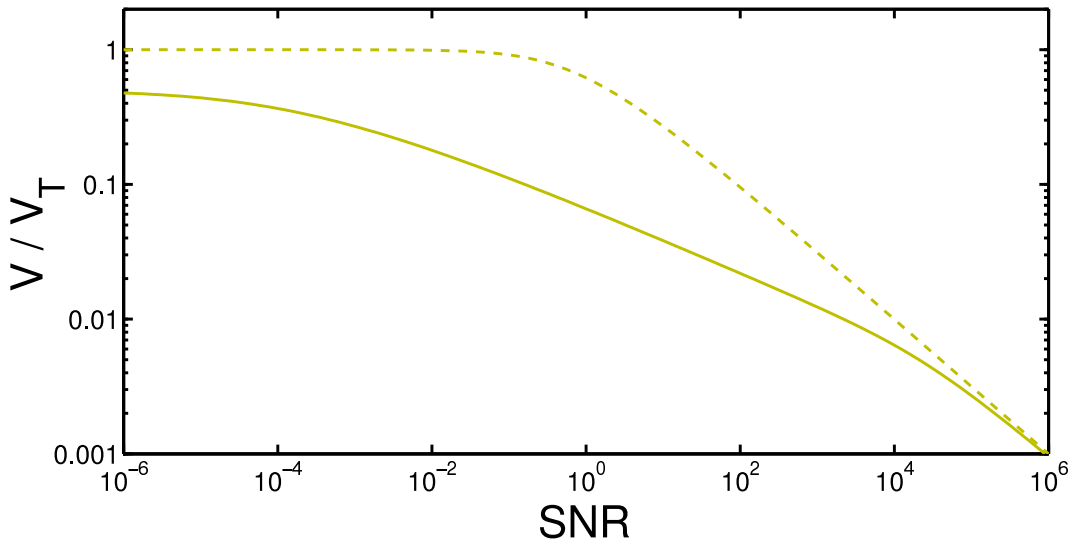

Figure 4.4: Conditional variance normalised to thermal variance for $N \gg 1$, for a quadrature with no parametric drive (V_0, dotted line) and in the squeezed quadrature with the drive $\chi = 100\gamma$ and detuning at threshold ($V_{X\alpha}$, solid line). In this high temperature regime, the conditioning is not limited by backaction when SNR $\gg 1$

When performing position estimation, a detuned parametric drive results in an elliptical Gaussian uncertainty. However, the antisqueezing angle of this distribution does not in general correspond to α_0, which defines the axis of the average elliptical trajectory. Figure 4.2 illustrates this difference, where a parametric drive phase of $\pi/4$ results in an antisqueezing angle α_1 for the conditional variance.

In order to solve the variances for the maximally squeezed and antisqueezed quadratures, it is convenient to define the pump phase θ as a function of SNR and pump parameters so that the X quadrature is always maximally squeezed and the covariance vanishes. In order to work in terms of the equivalent antisqueezing angle, we make the replacement $\theta = \pi/4 - \alpha_1$ and set $C = 0$, simplifying the equations above.[1] Applying the steady-state condition and solving gives

$$V_{X\alpha} = \frac{\sqrt{(\gamma + \chi\sin(2\alpha_1))^2 + 4\gamma^2\mathrm{SNR}} - \gamma - \chi\sin(2\alpha_1)}{4\eta\mu} \tag{4.48}$$

$$V_{Y\alpha} = \frac{\sqrt{(\gamma - \chi\sin(2\alpha_1))^2 + 4\gamma^2\mathrm{SNR}} - \gamma + \chi\sin(2\alpha_1)}{4\eta\mu} \tag{4.49}$$

$$\cos(2\alpha_1) = \frac{\Delta(V_Y - V_X)}{\chi(V_Y + V_X)}\,. \tag{4.50}$$

We can see that setting $\Delta = 0$ reproduces the resonant case where $\alpha_1 = \pi/4$ and the drive strength χ appears as modifications to the damping rate. The conditional variances may be solved exactly by finding the antisqueezing angle α_1 in terms of system parameters. The

[1] In an experimental situation, the pump phase would be kept constant, while the squeezing angle would be found in post-processing. In keeping with this we call these optimal variances $V_{X\alpha}$ and $V_{Y\alpha}$.

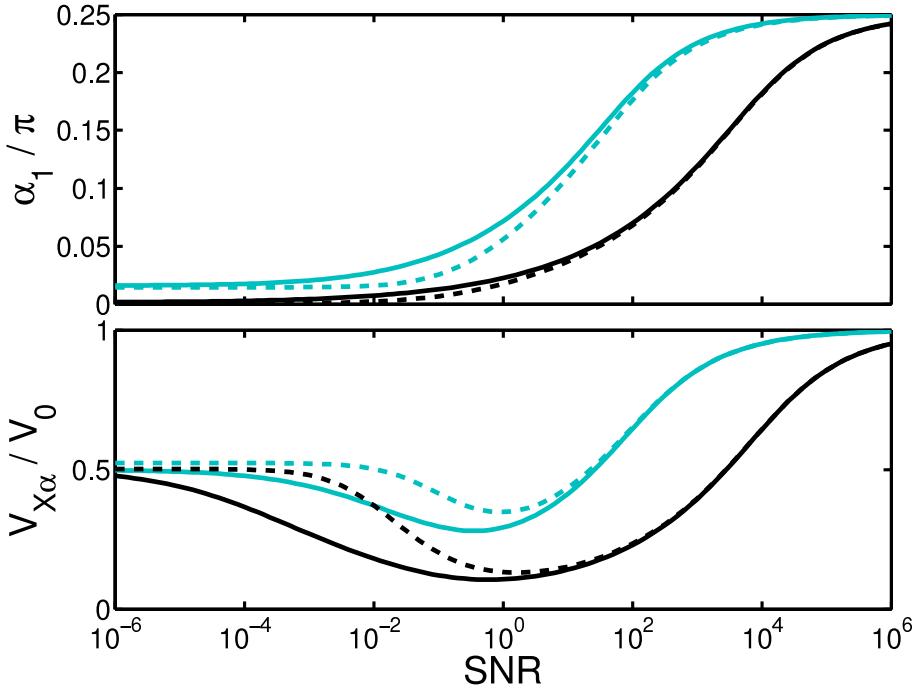

Figure 4.5: (Above) Antisqueezing angle α_1 and (below) squeezing ratio $V_{X\alpha}/V_0$ vs SNR. Light curves are for a drive strength $\chi = 10\gamma$ while dark curves are for $\chi = 100\gamma$. Solid lines are for the pump detuning on threshold, while dashed lines indicate detuning away from threshold by γ. Note that the squeezing disappears altogether in the strong measurement limit.

antisqueezing angle (derived in Appendix A) satisfies

$$\cos 2\alpha_1 = \frac{\Delta}{\chi_{th}} \left(\frac{\chi_{th}^2 + \chi^2 + 4\gamma^2 \mathrm{SNR} - \sqrt{(\chi_{th}^2 - \chi^2)^2 + 8(\chi_{th}^2 + \chi^2)\gamma^2 \mathrm{SNR} + 16\gamma^4 \mathrm{SNR}^2}}{2\chi^2} \right)^{\frac{1}{2}} \tag{4.51}$$

Inserting this into Eqs (4.48-4.49) gives the squeezed and antisqueezed steady-state variances. The squeezed variance, normalised by the thermal variance, is plotted in Fig. 4.4 along with the undriven conditional variance V_0 in the high temperature limit where backaction is negligible. Here it can be seen that in comparison to the undriven case, the conditioning due to measurement in the driven case begins at a lower SNR.

The ratio $V_{X\alpha}/V_0$ illustrates the improvement in conditioning due to a detuned parametric drive as a function of SNR. Notably, since α_1 does not depend on N, η and μ separately but on their combined form SNR, this ratio has the same property. In other words, the ratio $V_{X\alpha}/V_0$ is temperature-independent. This *conditional squeezing* ratio starts at the unconditional squeezing ($\approx 1/2$), drops to a minimum near SNR ≈ 1, and approaches unity in the strong measurement limit.

The degradation of the conditional squeezing for strong measurement occurs even in this classical regime where backaction heating may be negligible. This can be seen by the squeezed and antisqueezed variances given by Eqs (4.48-4.49) becoming independent of the parametric drive as SNR $\to \infty$. The effect of the parametric drive on the squeezed quadrature can be inter-

preted as a signal boost due to the amplified quadrature, which is correlated by the detuning. This is of greatest benefit near SNR ≈ 1 where the mechanical signal and measurement noises are comparable and the conditional variance V_0 is most sensitive to SNR. In other words, it is here that conditioning the squeezed quadrature via the well-transduced amplified quadrature is more efficient than direct conditioning. This is the key result of the thesis, and will be shown in subsequent chapters to have significant implications for quantum measurement.

At threshold, Eq. (4.51) reduces to

$$\cos(2\alpha_1) = \frac{\sqrt{\chi^2-\gamma^2}}{\chi^2}\left(\sqrt{\chi^2+\gamma^2\mathrm{SNR}}-\gamma\sqrt{\mathrm{SNR}}\right) . \tag{4.52}$$

In the limit $\chi \gg \gamma$ and SNR $= 1$, the following approximation can then be made

$$\chi\sin(2\alpha_1) \approx \gamma\sqrt{2\chi/\gamma} . \tag{4.53}$$

The amount of squeezing achievable relative to the undriven conditional variance V_0 in this limit is similarly proportional to $\sqrt{\chi/\gamma}$. For the rotating wave approximation to remain valid, as assumed by our theory, χ/γ must be less than the oscillator Q factor (i.e. $\chi \ll \omega_m$).

4.8 Optimal filter

The conditional variances quantify the error of an optimal estimate filtered from the measurement record. As done for a simple damped oscillator in Section 3.5.1, these filter can be derived from the mean value equations. Unlike this previous derivation, the two quadrature estimates in the presence of a parametric drive will require different filter parameters. The first step is to rewrite the mean value equations (4.12-4.13) in terms of the measurement records $Q_{X\alpha}$ and $Q_{Y\alpha}$ rather than the white noise residuals $\mathrm{d}W_1$ and $\mathrm{d}W_2$. This results in additional damping terms proportional to the measurement rate $\eta\mu$. As in the previous section, we will choose a pump phase $\theta = \pi/4 - \alpha_1$ and set $C = 0$. Substituting these values, Fourier transforming and solving for $\langle X_{est}(\omega)\rangle$ gives

$$\langle X_{\alpha\mathrm{est}}(\omega)\rangle = \sqrt{4\eta\mu}\frac{(\gamma_Y-\chi\sin(2\alpha_1)+i\omega)V_{X\alpha}Q_{X\alpha}(\omega)-(\Delta-\chi\cos(2\alpha_0))V_{Y\alpha}Q_{Y\alpha}(\omega)}{\Delta^2-\chi^2+\gamma_X\gamma_Y+\chi\sin(2\alpha_1)(\gamma_Y-\gamma_X)-\omega^2+i\omega(\gamma_X+\gamma_Y)} \tag{4.54}$$

where the intrinsic and measurement-induced damping rates of the X and Y quadratures are respectively combined as

$$\gamma_X = \gamma + 4\eta\mu V_{X\alpha} \tag{4.55}$$

$$\gamma_Y = \gamma + 4\eta\mu V_{Y\alpha} . \tag{4.56}$$

Increasing μ causes the optimal filters to widen as the ratio of mechanical signal to measurement noise increases. These two bandwidths are equal in the bad measurement limit (where $\eta\mu \to 0$) as well as the strong measurement limit (where $V_{X\alpha} \approx V_{Y\alpha}$), but vastly different near SNR ≈ 1

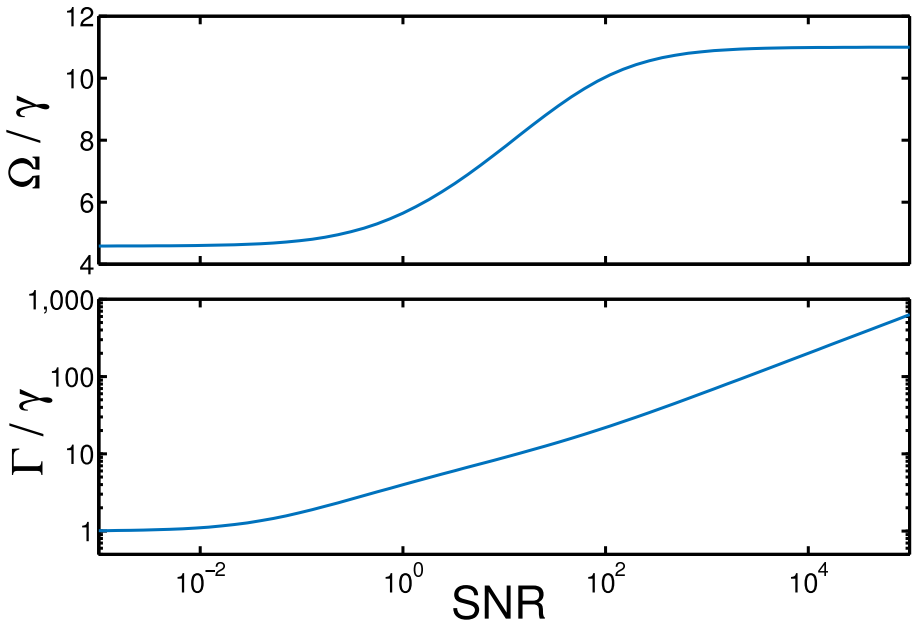

Figure 4.6: (Above) Filter convolution frequency Ω and (below) filter bandwidth Γ, both normalised to the intrinsic linewidth, plotted against SNR. The parametric drive parameters are $\chi/\gamma = 10$ and $\Delta/\gamma = 11$.

if driven near threshold. We will limit ourselves to the regime $\Delta^2 > \chi^2$, where the general form of the above solution in the time domain is

$$\langle X_{\alpha est}(t)\rangle = g_{XX}Q_{X\alpha}(t) * \left[\cos(\Omega t + \phi)e^{-\Gamma t}\right] + g_{XY}Q_{Y\alpha}(t) * \left[\sin(\Omega t)e^{-\Gamma t}\right] \ , \tag{4.57}$$

and similarly for the Y estimate

$$\langle Y_{\alpha\text{est}}(t)\rangle = g_{YY}Q_{Y\alpha}(t) * \left[\cos(\Omega t - \phi)e^{-\Gamma t}\right] + g_{YX}Q_{X\alpha}(t) * \left[\sin(\Omega t)e^{-\Gamma t}\right] \ . \tag{4.58}$$

The parameters are obtained from Eq. (4.54) and simplified in terms of α_1 using relations (4.50) and (A.2)

$$\begin{aligned}
\Omega &= \sqrt{\Delta^2 - \chi^2\cos^2(2\alpha_1)(1+\gamma^2/\Delta^2)} && (4.59)\\
\Gamma &= \frac{1}{2}(\gamma_X + \gamma_Y) \\
&= \Delta\tan(2\alpha_1) && (4.60)\\
\phi &= \tan^{-1}\frac{\chi\gamma\cos(2\alpha_1)}{\Delta\Omega} && (4.61)\\
g_{XX} &= \sec\phi\sqrt{4\eta\mu}V_{X\alpha} && (4.62)\\
g_{XY} &= \frac{\Delta - \chi\cos(2\alpha_1)}{\Omega}\sqrt{4\eta\mu}V_{Y\alpha} && (4.63)\\
g_{YY} &= \sec\phi\sqrt{4\eta\mu}V_{Y\alpha} && (4.64)\\
g_{YX} &= \frac{\Delta + \chi\cos(2\alpha_1)}{\Omega}\sqrt{4\eta\mu}V_{X\alpha}\ . && (4.65)
\end{aligned}$$

These expressions simplify in the SNR = 0 limit (where $\cos(2\alpha_1) = \Delta/\chi_{th}$) to expected values (e.g. $\Omega = \omega_e$ and $\Gamma = \gamma$). In the high SNR limit (where $\cos(2\alpha_1) = 0$) the optimal filter has

infinite bandwidth and is independent of the parametric drive, while the convolution frequency is equal to the detuning. These limits are shown in Figure 4.6.

The measurement records for X and Y, upon applying these Lorentzian filters, form an optimal estimate of the oscillator's current position in phase space. In other words, the amplitudes of the in-phase and out-of-phase fluctuations are known to within uncertainties defined by $V_{X\alpha}$ and $V_{Y\alpha}$. By mixing the estimate back up to ω_d and with the correct phase shift, an appropriate feedback cooling signal is obtained. In this way, conditional squeezing is turned into real squeezing[89].

Chapter 5

Demonstration of enhanced theromomechanical squeezing

5.1 Introduction

In the previous chapter, it was shown that a detuned parametric drive can improve the effective steady-state localisation of one quadrature, as quantified by the conditional variance. This improvement is, in principle, unlimited. This stands in contrast to the unconditional variance, for which the single-quadrature improvement cannot exceed 3dB in the steady-state. The role of the detuning is to induce correlations between the amplified and squeezed motional quadratures while keeping the oscillator below threshold. Information encoded on the amplified quadrature then allows the squeezed quadrature to be estimated with enhanced precision. The improvement is optimised when the oscillator signal is comparable to the measurement noise.

This chapter summarises an experimental demonstration of the above idea using a conventional AFM cantilever, monitored at room temperature by a fiber interferometer. Optimal control techniques and parametric modulation were used to both break the 3dB limit for the first time and achieve mechanical localisation exceeding the measurement sensitivity of the interferometer by 6.2dB. These experiments were performed at room temperature, and as such are far from the quantum regime. The enhanced localisation possible through such "thermomechanical squeezing" can, however, be useful in force measurement; for instance, by increasing the dynamic range when signal distortion is introduced at large amplitudes[19, 104]; by broadening the bandwidth in the squeezed quadrature[105]; and by enhancing the sensitivity to pulsed forces with known timing[106, 107]. Furthermore, since the technique demonstrated here applies equally to quantum zero-point noise, it provides a path towards precise quantum control and robust quantum squeezing of mechanical oscillators at attainable temperatures and in the absence of strong measurement.

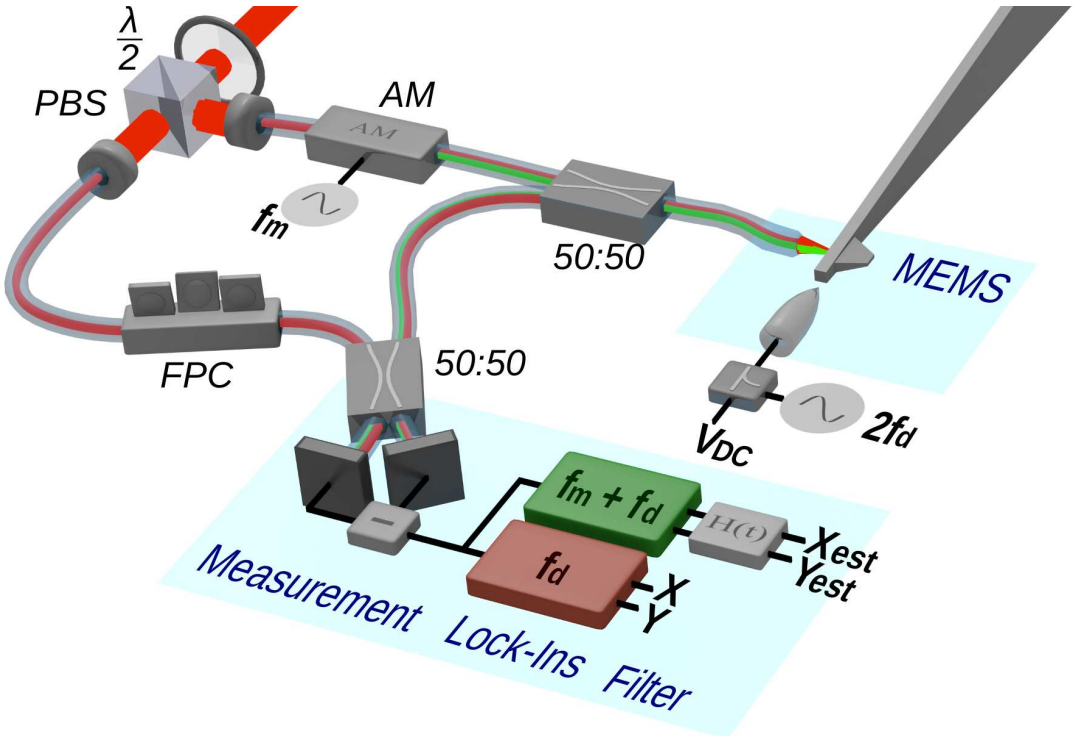

Figure 5.1: Simplified schematic of the experimental setup. The red path in the fiber-based interferometer denotes the high-fidelity carrier signal while the green path denotes the low-fidelity signal created by amplitude modulation (AM). PBS: polarising beam-splitter; FPC: fiber polarisation controller. 3D rendering by Michael Taylor.

5.2 Experimental setup

The experimental setup, a simplified version of which is shown in Fig. 5.1, is based on a commonly used optical measurement of the mechanical element in a typical MEMS. The position of a gold-coated AFM cantilever was monitored using a Mach-Zender interferometer in a balanced homodyne configuration, with a fiber tip used to focus the optical field onto the cantilever. This allowed a high-fidelity measurement of the thermal noise in the fundamental mode of the cantilever, which was used to characterise its motion and the accuracy of our estimation procedure. A weak sideband was also created using an intensity modulation of the bright field, providing a low-fidelity measurement with independent shot-noise characteristics which was used to perform position estimation. The fidelity of this measurement could be varied, allowing the study of estimation techniques in the important regime where the signal level is comparable to the measurement noise floor, i.e. where the signal-to-noise ratio SNR $= V_T/V_{\text{shot}} \approx 1$. Both high and low-fidelity position measurements were fed into lock-in amplifiers along with frequency references from signal generators. The mixed-down quadrature outputs were then fed into data acquisition units for post-processing.

The cantilever was glued onto a piezoelectric transducer for direct excitation, and the lensed fibre tip was mounted on a piezoelectric controller for accurate positioning with respect to the cantilever. These were mounted inside a vacuum chamber kept at $0.01 - 0.02$mbar throughout

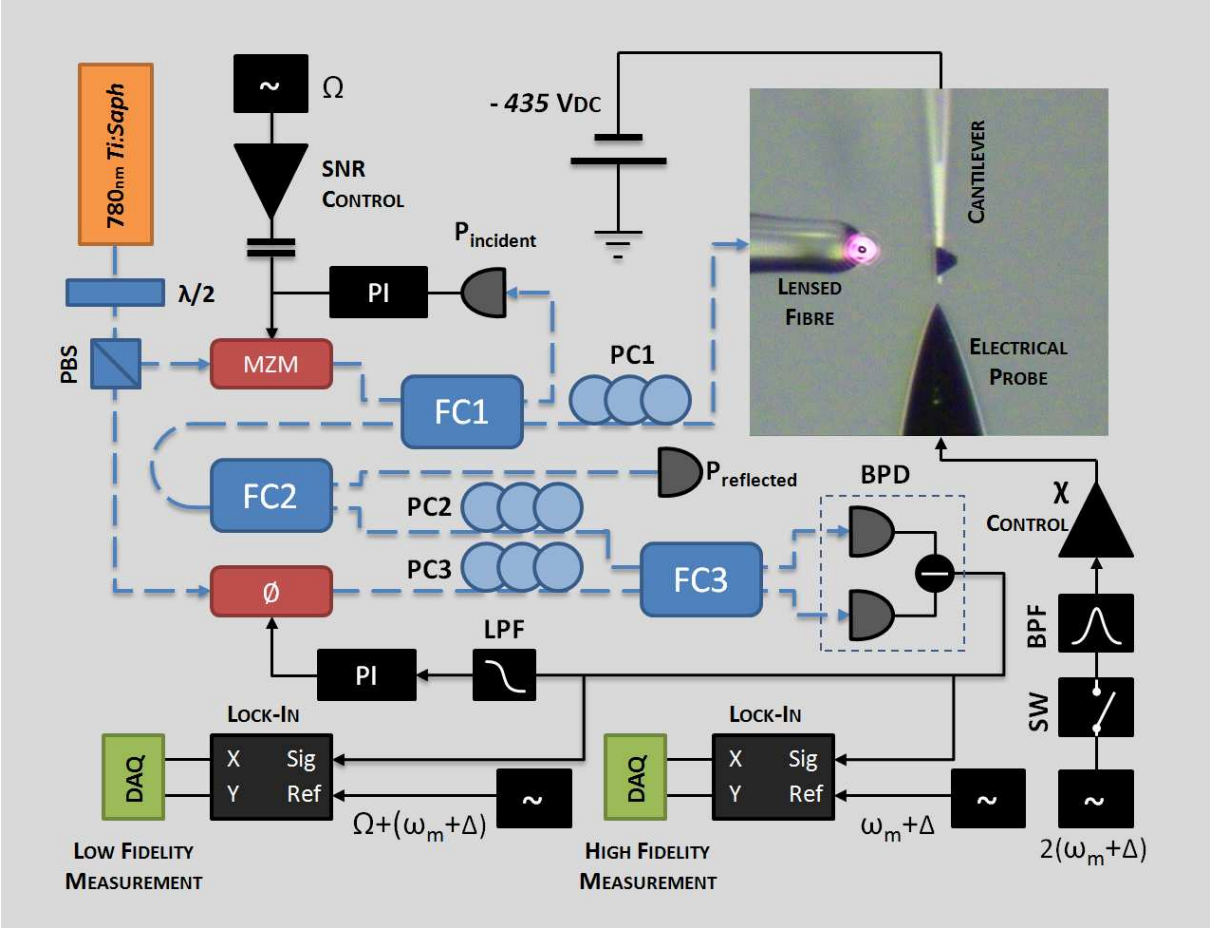

Figure 5.2: Full schematic of the experiment. The inset is a photograph of the cantilever with the fiber and electrode in operational positions. FC: fiber coupler (50%), MZM: Mach-Zender Modulator, PBS: polarising beam-splitter, DAQ: data acquisition unit, BPF: band pass filter, LPF: low pass filter, BPD: balanced photodetector, PC: polarisation controller, PI: proportional-integral controller. Schematic courtesy of George Brawley.

the experiment. The low pressure reduced the damping of the resonator and mitigated spurious electrostatic effects. The final element of the experimental apparatus consisted of a sharp electrode, used to electrostatically modify the spring constant of the cantilever. This was used to both tune the resonance frequency via a DC voltage, and to apply the parametric drive using an additional sinusoidal voltage. The signal generators, switches and data acquisition units were synchronised using LabView software. The next two sections will detail the optical and electromechanical components of the experiment, respectively.

5.2.1 Fiber interferometer

A Mach-Zender interferometer measures the relative phase shift between two optical paths — generally, a signal path and a local oscillator (LO). This technique is widely used for position measurement[108, 109], since the position of a mirror determines the phase of reflected light at a fixed point in the optical path. As such, mirrors mounted on piezoelectric crystals are a

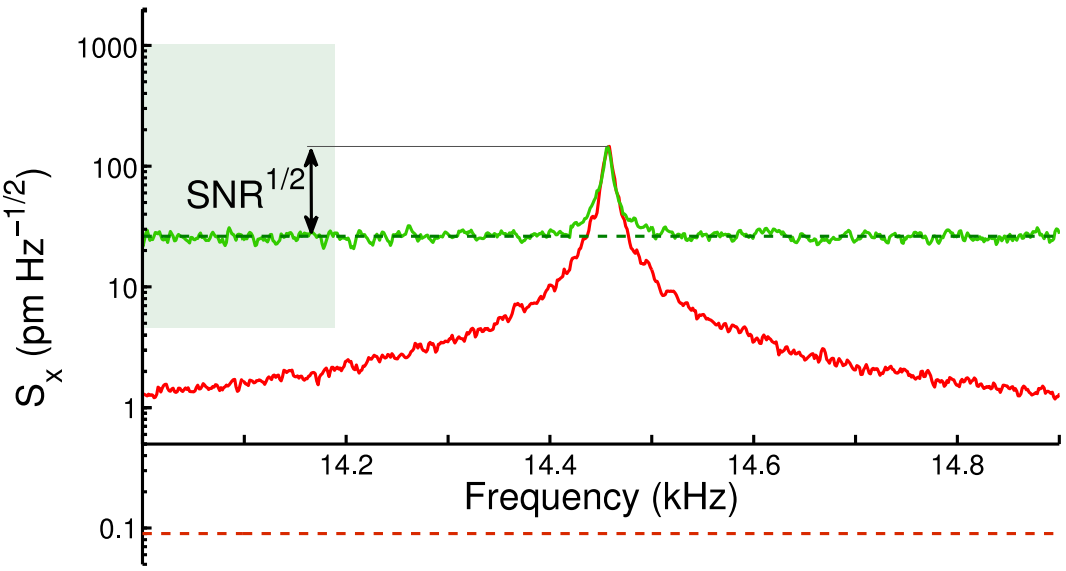

Figure 5.3: Displacement noise spectrum around the fundamental cantilever resonance measured by the laser carrier (red) and by the sideband created with a $1V_{pp}$ modulation (green). Dotted lines represent the respective shot-noise limited sensitivities of the measurements, while the green band corresponds to the range of sensitivity available from the utilised sideband intensities.

common way of achieving low-frequency phase modulation of light. When the signal path and local oscillator are spatially mixed, the outgoing light intensity depends on the strengths and relative phases of the two beams.

Balanced homodyne measurement is an optimal way to measure a single quadrature of light — in this case, the phase quadrature — with minimal classical noise. This is done by making the local oscillator beam much more intense than the signal beam, detecting both outputs of the beam-splitter, and subtracting the outputs of the two detectors. This subtraction cancels the constant amplitude quadrature, as well as the classical noise, of the local oscillator. Ideally, the remaining noise is the white-noise of the quantum fluctuations of the light field, known as shot-noise. By modifying the polarisation on each arm of the interferometer, the influence of the signal phase on the outgoing phase quadrature can be maximised.

A shot-noise limited 780nm Titanium-Sapphire laser was used to perform the measurements. The interferometer was implemented in-fibre using fibre-based couplers and polarisation controllers. A lensed tip was used to focus the light onto the cantilever and to collimate the reflected light. The position of the fiber tip with respect to the cantilever was optimised using a piezoelectric controller to maximise the intensity of reflected light. The phase of the local oscillator was stabilised using a proportional-integral (PI) controller. Typical local oscillator power was 170μW per side at the homodyne detector, while typical reflected signal power was 0.5μW per side.

A weak sideband was created using a Mach-Zender amplitude modulator, providing the independent low-fidelity measurement. This was achieved by using a DC voltage to set the

intensity in the linear region of the sinusoidal response and adding a radio-frequency signal to the input. To eliminate drift of the intensity of the outgoing fundamental mode, a PI controller was used as the DC input. A 10 MHz modulation signal was used to create the sideband and the amplitude of the modulation signal was used to set the intensity (and thus sensitivity) of the sideband. This frequency was within the photodetector bandwidth of 100 MHz. The high-fidelity position quadrature measurements were created by feeding the homodyne output into a lock-in detector set to the reference frequency f_d, so that it captured the fluctuations around the fundamental laser mode. The low-fidelity quadrature measurements were created using a separate lock-in amplifier set to $f_d + 10\text{MHz}$, so that it captured the same fluctuations in the weak sideband.

During the measurements, the sensitivity S_x of the interferometer was $90\text{fm}/\sqrt{\text{Hz}}$, as shown in Fig. 5.3. This value was found by reading off the height of a spectral peak from adding a sinusoidal voltage to the interferometer's phase shifter. This known phase shift is then related to displacement by the laser wavelength. The measurement shot-noise for this signal $V_{\text{shot}} = 4\gamma S_x^2$, where γ is the mode's decay rate, was 60dB below the thermally-induced variance V_T. The sensitivity of the low-fidelity measurement could be varied between 25 and $1000\text{pm}/\sqrt{\text{Hz}}$ by adjusting the optical modulation depth, as illustrated in Fig. 5.3. At room temperature, the thermal noise signal lay within this region.

5.2.2 Capacitive parametric tuning and modulation

A dielectric inside a capacitor can experience a force if the surrounding electric field is nonuniform. If motion of the dielectric along a position axis x increases the stored energy E of the capacitor, the force in this direction will be

$$F_x = \frac{\mathrm{d}E}{\mathrm{d}x} \tag{5.1}$$

$$= \frac{1}{2}\frac{\mathrm{d}C}{\mathrm{d}x}V^2 \tag{5.2}$$

where C is the capacitance and V is the voltage across the plates. This is due to conservation of energy. In the same fashion, a dielectric can experience a change in spring constant if the electric field is highly nonuniform.

$$k_r = \frac{\mathrm{d}F_x}{\mathrm{d}x} \tag{5.3}$$

$$= \frac{1}{2}\frac{\mathrm{d}^2C}{\mathrm{d}x^2}V^2 \tag{5.4}$$

Therefore, the intrinsic spring constant of an oscillator can be enhanced or reduced, depending on geometry, by applying a voltage. This effect is commonly used for parametric modulation in MEMS and NEMS systems[25, 60]. Separating this voltage into a large constant part V_{DC} and a smaller time-dependent part $V_{\text{AC}}(t)$, the approximation can be made

$$V^2(t) = (V_{\text{DC}} + V_{\text{AC}}(t))^2 \tag{5.5}$$

$$\approx V_{\text{DC}}^2 + 2V_{\text{DC}}V_{\text{AC}}(t) \tag{5.6}$$

so that the additional spring constant varies linearly with the time-dependent voltage. A large DC voltage also has the advantage of amplifying the effect of the time-dependent signal.

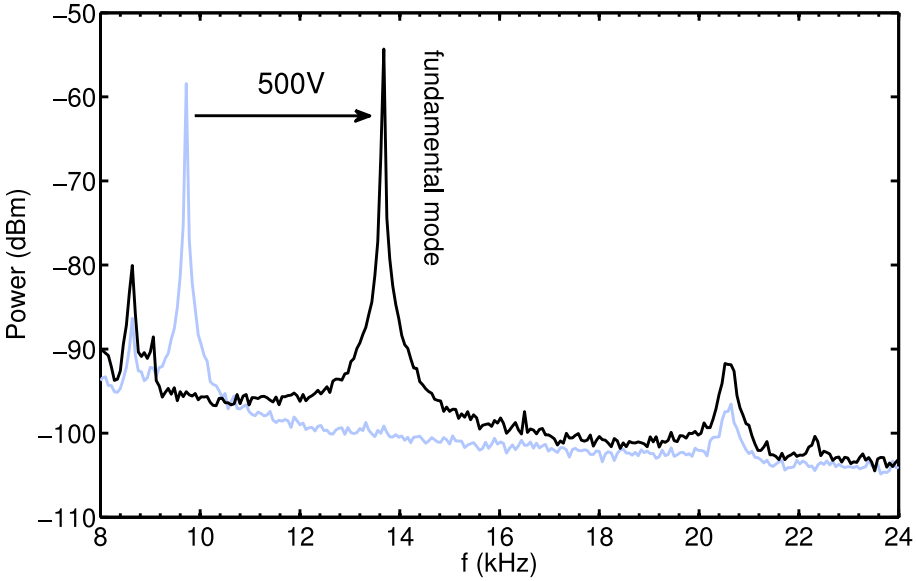

Figure 5.4: Spectrum of photodetector output with 0V (light) and 500V (dark) applied to the electrode, with no direct excitation of the cantilever. The nonlinear capacitance causes a shift of around 4kHz in the fundamental mode with little noticeable change in linewidth. The operating frequency of the cantilever ($12.5 - 14.5$kHz) is far from the other peaks in the spectrum, which are due to laser noise. Apart from these technical peaks, the spectrum is dominated by the thermal excitation of the mechanical mode.

A conventional acupuncture tip was used as an electrode to create a highly non-uniform electric field near the free end of the AFM cantilever. The electrode tip was positioned around 20 microns from the cantilever end using a piezoelectric controller and fixed in place with non-conductive epoxy resin to the same metal block as the cantilever. This mounting setup was essential to minimise frequency fluctuations in the cantilever, which were extremely sensitive to the distance between cantilever and electrode tip. For the same reason, a low-noise turbo-molecular vacuum system was used in addition to the vibration-isolating optical bench. To minimise frequency fluctuations due to electrical noise, band-pass filters and attenuators were used for the AC parametric drive and piezoelectric mount.

A high voltage was applied to the cantilever with a stiffening effect on a majority of mechanical modes. Figures 5.4 and 5.5 show the effect of the DC voltage on the frequency and Q-factor of the fundamental flexural mode used in the experiment. The damping rate of the fundamental mode was around 2Hz in the absence of tuning, giving a Q-factor of approximately 5000. This Q-factor was maintained at all operating frequencies for the duration of the experiment. At low voltages, the change in frequency is quadratic, since here the electrostatically

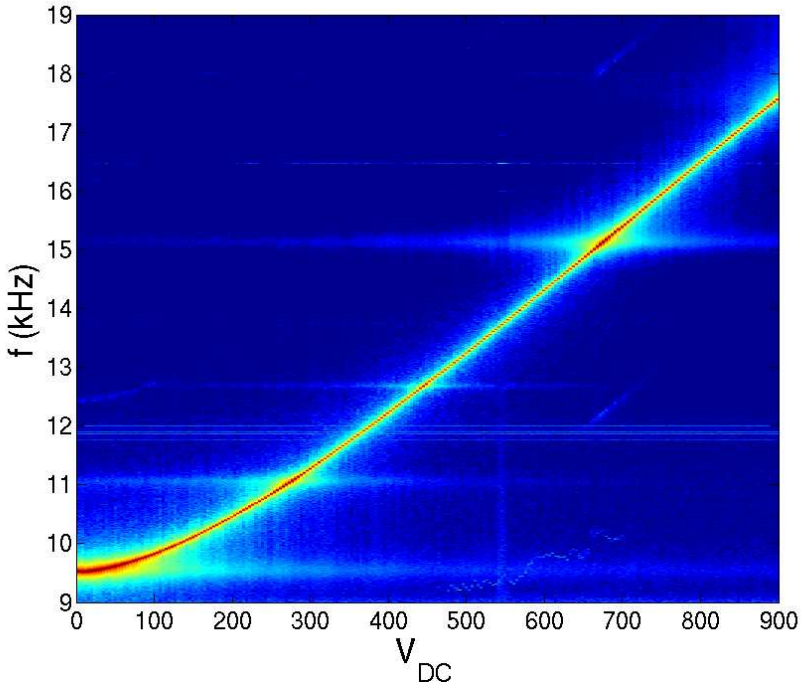

Figure 5.5: Spectrum of fundamental flexural mechanical mode as a function of applied DC voltage. At each voltage, a square pulse was applied to the piezo mount, exciting the oscillator at all frequencies. The colour in each vertical strip corresponds to the Fourier transform of the subsequent position measurement.

induced spring constant k_r is small compared to the intrinsic spring constant $k_0 \approx 0.06\mathrm{N/m}$, so

$$\begin{aligned} f_m &= \sqrt{(k_0 + k_r)/m_{\mathrm{eff}}} && (5.7) \\ &\approx f_0(1 + k_r/2k_0) && (5.8) \\ &\approx f_0\left(1 + \frac{1}{4}\frac{\mathrm{d}^2C}{\mathrm{d}x^2}V_{\mathrm{DC}}^2/k_0\right) && (5.9) \end{aligned}$$

while at higher voltages, k_r is the dominant term and hence the frequency varies linearly with V_{DC}. The frequency-voltage dependence in Fig. 5.5 fits a value of $\mathrm{d}^2C/\mathrm{d}x^2 \approx 4.2{\times}10^{-7}\mathrm{Nm}^{-1}\mathrm{V}^{-2}$ for the geometric nonlinearity. This is about a factor of 50 smaller than that obtained by Rugar and Grütter[25] with a similar geometry, most likely due to a slight mis-alignment in one axis.

In the experiments detailed here, the spring constant of the fundamental flexural mode was increased well above its intrinsic value k_0 by applying between 450 and 650 volts to the cantilever. A sinusoidal AC voltage from a signal generator was then applied to the electrode to provide a parametric drive near $2f_m$. The effect of a resonant parametric drive on a coherent excitation can be seen in Figure 5.6. The relative phase between a direct piezoelectric excitation at f_m and a parametric drive at $2f_m$ was adjusted at various parametric drive amplitudes. The gain shown is the ratio of the lock-in output with the parametric drive on to the amplitude with the drive off, in the quadrature of the direct excitation. The maximum and minimum gains are shown, corresponding to piezoelectric drive phases separated by 90 degrees. Threshold is

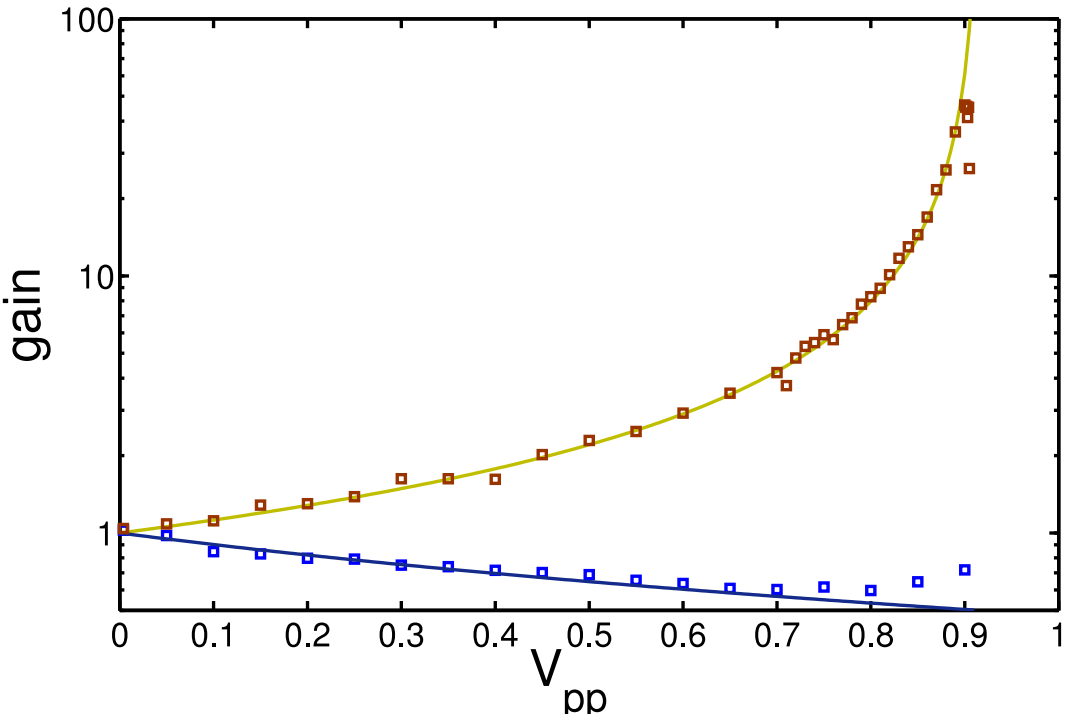

Figure 5.6: Gain measurements taken with the cantilever tuned to 14.5kHz and a relative drive phase of zero (red squares) and 90 degrees (blue squares). Solid lines are fits to a threshold voltage of 0.92V. Deviation near threshold is due to very high sensitivity to cantilever frequency and drive phase.

reached at 0.92V, close to the theoretical value of 1.2V expected from the geometric nonlinearity and Q-factor.

5.3 Unconditional results

Initially, the results of Section 4.6 were reproduced by analysing the unconditional step-response of the thermal noise in the cantilever to a parametric drive. To avoid any direct forces near f_m due to the sudden turn-on, the drive signal was fed through a band-pass filter near $2f_m$. This increased the turn-on time from zero to approximately 2.5ms. The position measurement was fed into a lock-in amplifier with a bandwidth much wider than the mechanical decay rate γ, allowing the position dynamics around f_m to be observed in a rotating frame at a nearby reference frequency $f_d = f_m + \Delta$. Here, the DC voltage was set to 450V, shifting the fundamental mode frequency from $f_0 = 9.6$kHz to $f_m = 12.5$kHz.

When driven on resonance ($\Delta = 0$), and with a strength above the instability threshold ($\chi > \gamma$), thermomechanical squeezing can surpass 3dB while the orthogonal quadrature is amplified indefinitely. Figure 5.7a shows the time-evolution of the maximally squeezed and antisqueezed quadrature variances measured in this regime, with $\chi = 22.5$Hz and $\gamma = 2$Hz. Good agreement with theory is observed at short times (<20ms) with exponential growth of the amplified quadrature and thermomechanical squeezing approaching 11dB in the orthogonal

quadrature. However, the amplified quadrature saturates after approximately 35ms, where the amplitude approaches the optical quarter-wavelength of 195nm and oscillations are no longer confined to the linear portion of the interference fringe. Crucially, a side-effect of this measurement nonlinearity is a severe degradation in observed squeezing well before saturation is apparent. Such limits to dynamic range therefore preclude the generation of all but transient squeezing above threshold. Nonetheless the strong squeezing observed reproduces the nonequilibrium squeezing observed in trapped ions[7] for the first time in a micromechanical oscillator, albeit in the classical regime. Transient squeezing of this kind could be useful in applications where operation outside of equilibrium is acceptable, such as stroboscopic sensing[106].

By detuning the parametric drive off resonance, the oscillator phase undergoes a net rotation with respect to the amplification axis, increasing the instability threshold according to Eq. (4.14). Consequently for the drive strength used here ($\chi = 22.5$Hz), the oscillator is unstable for detunings below $\Delta = 22.4$Hz. When the detuning is increased further so that $\Delta > \chi$, the phase-space trajectories form stable elliptical orbits. The variances initially mirror this oscillatory behaviour before relaxing to steady-state values in the long time limit, in quantitative agreement with Eqs (4.40-4.44). The effect of increasing detuning on the transient statistics can be seen in Fig. 5.7b, where a dramatic change from monotonic behaviour to clear oscillations in the variance occurs at the threshold detuning. Notably, transient squeezing below 3dB is still possible below threshold, owing to the rapid drive turn-on. The final steady-state variances agree with Eqs (4.36-4.38), where the steady-state squeezed variance is fundamentally limited to $V_T/2$.

5.4 Conditional results

From the above observations, the benefit of a parametrically driven system in equilibrium would appear to be limited to enhanced readout in one quadrature and 3dB reduced variance in the other. However, as shown in Section 4.7, these phenomena can be combined to enhance localisation using a weak measurement and optimal estimation. For an oscillator detuned so that $\Delta > \chi$ and which has relaxed to the steady-state, the thermally excited oscillations will alternate between amplified and squeezed quadratures before decaying. Since the dynamics of the system are well known, a measurement of the amplified quadrature will provide some capacity to estimate the squeezed quadrature at a later time. The squeezed quadrature therefore obtains an effective sensitivity enhancement without amplifying its mechanical fluctuations. This is useful for localising an oscillator where conditions such as cold environment, poor measurement sensitivity or high oscillator frequency limit the SNR.

Steady-state estimation was performed with the cantilever tuned to 14.5kHz by a 650V bias and with a variable sideband intensity to tune the SNR of the low-fidelity measurement. At each SNR, simultaneous 45-second traces of the lock-in outputs $X, Y, \tilde{X}, \tilde{Y}$ were recorded using a data acquisition unit (700 samples/sec) with no parametric drive applied to the cantilever.

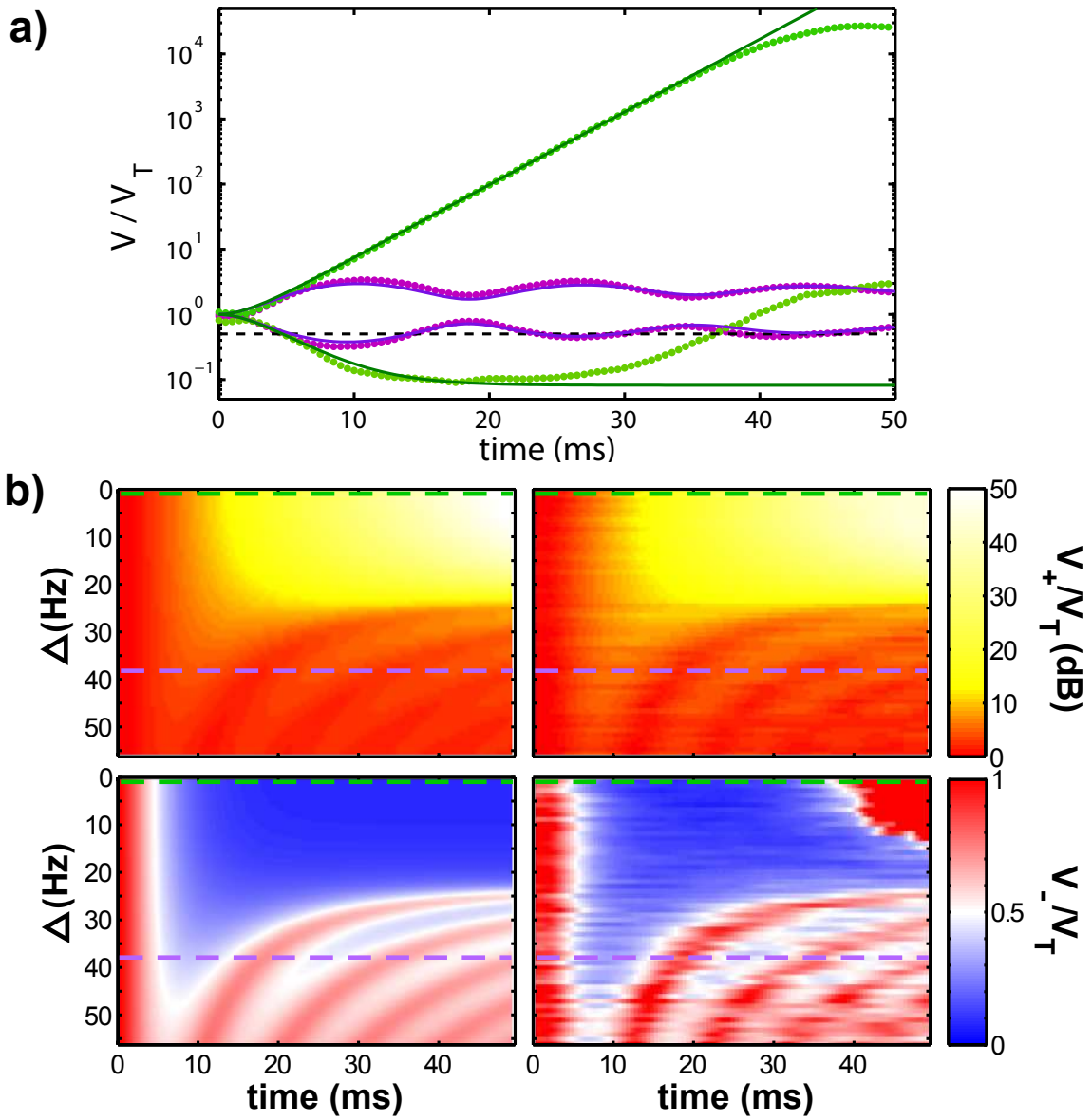

Figure 5.7: Evolution of the squeezed and antisqueezed quadratures with a continuous parametric drive of strength $\chi = 22.5$Hz turned on at t = 0 and $f_0 = 12.5$kHz. a) Normalised quadrature variances vs time for an on-resonance drive (green) and for a below-threshold detuned drive with $\Delta = 38$Hz (violet). Solid lines are theoretical fits, while points show experimental statistics generated from 200 iterations of the drive turn-on. The dotted line represents the -3dB steady-state squeezing limit. At each point in time, the quadratures are rotated so that the covariance $\langle XY\rangle - \langle X\rangle\langle Y\rangle \approx 0$ over all iterations. A ring-up time of 2.5ms is chosen for the parametric drive to minimise impulse forces on the cantilever. b) Theoretical (left) and experimental (right) variances as a function of detuning and time. Blue areas indicate squeezing below 3dB.

Throughout the experiment, during these thermal measurements the oscillator resonance f_0 was kept within 5Hz of the lock-in reference frequency. Data acquisition was then repeated using parametric drives of various detunings at the same SNR. This drive strength was $\chi = 57$Hz and the detuning Δ was varied between approximately 62 and 64Hz. The lock-in reference

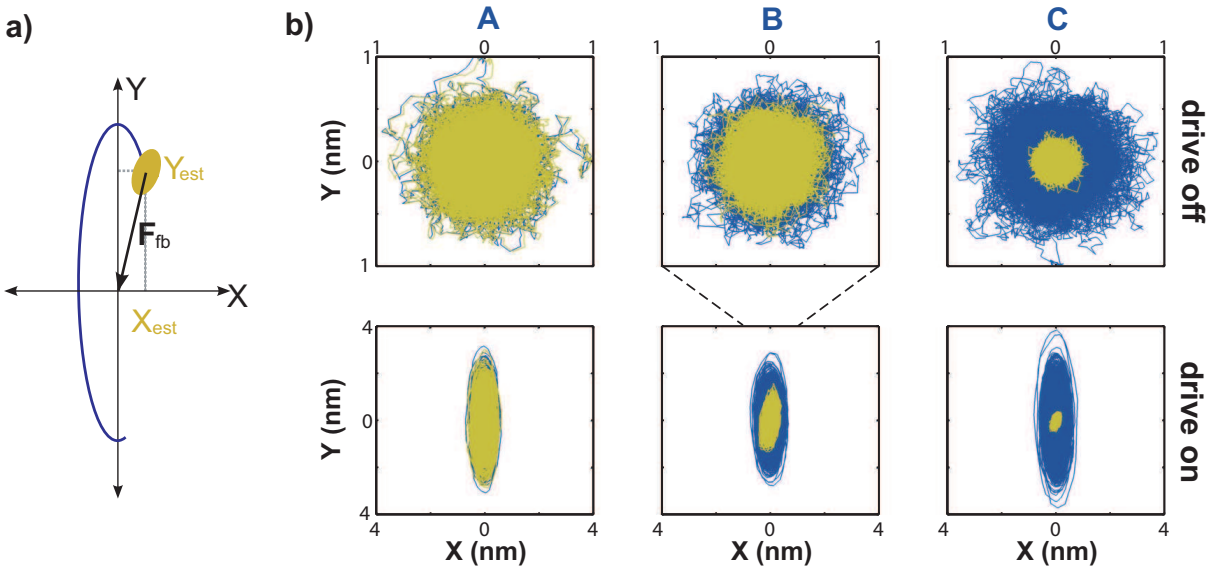

Figure 5.8: Reducing variance via estimation. a) Typical phase-space trajectory over a short time with a detuned parametric drive applied to the oscillator. The estimates $\{X_{est}, Y_{est}\}$ at a given time are calculated by filtering the low-fidelity data, agreeing with a high-fidelity measurement (blue curve) to within an uncertainty given by the yellow ellipse and localising the oscillator to this phase space region. A feedback force F_{fb} confining the oscillator to near the origin can be modelled by subtracting the estimates from the high-fidelity data. b) Quadrature phase-space trajectories for 22.5 second samples obtained from high-fidelity measurement (blue) and the residual after subtracting the estimate (yellow). The upper panels show the random-walk pattern in the undriven case mixed down at the resonance frequency $f_0 = 14.5$kHz for weak (A), intermediate (B) and strong measurement (C). The lower panels show the elliptical trajectories and residual noise for a parametric drive strength of $\chi = 57$Hz detuned close to threshold and using the same SNR as above.

frequency — now shifted by the parametric drive detuning Δ — was kept phase-locked to the drive voltage. A lock-in time constant of $\tau_c = 300\mu$s was used so that the output oscillations (limited in frequency to Δ) were contained within the output bandwidth. In order to keep the mechanical frequency constant to within a 5Hz range, the DC voltage was adjusted slightly at intervals of approximately ten minutes. This was required to compensate for gradual structural deformation, most likely due to temperature and pressure changes.

In both driven and undriven cases, optimal estimates of the time series $X_{\alpha\text{est}}(t)$ and $Y_{\alpha\text{est}}(t)$ were generated in post-processing by minimizing the respective conditional variances over the filter parameters. The estimates were produced by convolving the low-fidelity quadrature measurements with a filter function (truncated to 22.5 seconds), and the conditional variances $V_{X\alpha} = \langle (X_\alpha - X_{\alpha\text{est}})^2 \rangle$ and $V_{Y\alpha} = \langle (Y_\alpha - Y_{\alpha\text{est}})^2 \rangle$ were then calculated over the second half of the data. The optimum conditional variances were then found by minimising computationally over all filter parameters. This optimisation process is detailed in Appendix B.

The filter function in both driven and undriven cases, using Eqs (4.57-4.58), has the general

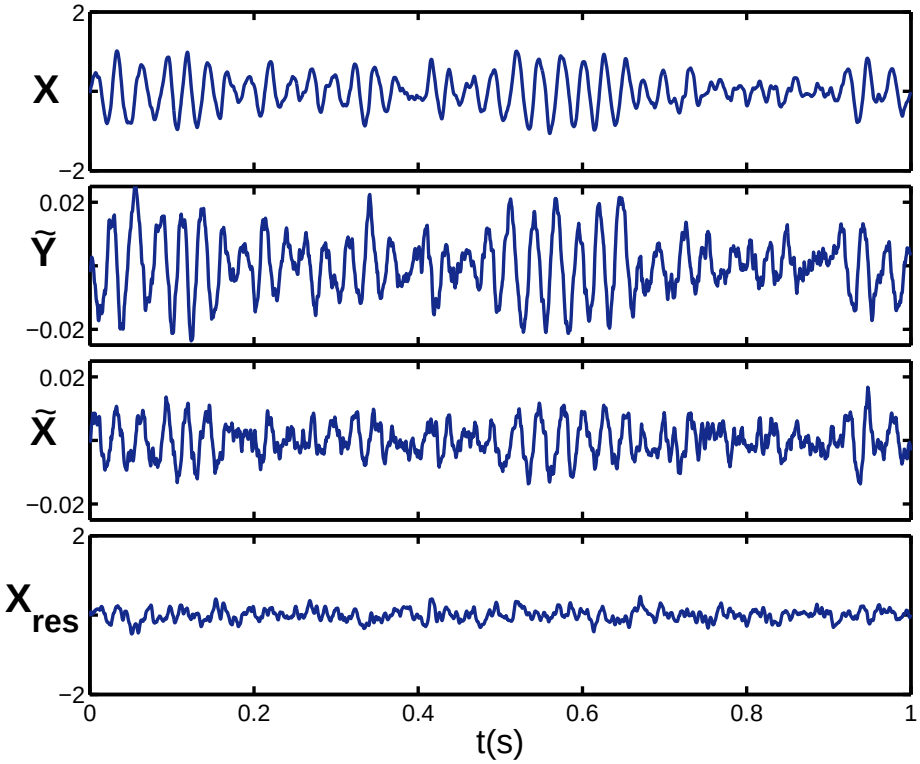

Figure 5.9: Typical time-traces of three lock-in outputs with a detuned parametric drive, and an optimal residual $X_{\rm res}$ after subtracting the optimal estimate from the high-fidelity measurement X. This optimal estimate is calculated from both low-fidelity measurements $\tilde{X}$ and $\tilde{Y}$, corresponding to the squeezed and amplified quadratures, respectively. Notably, the two quadratures are highly correlated, and the amplified quadrature is less prone to measurement noise.

form

$$\begin{bmatrix} X_{\alpha,est} \\ Y_{\alpha,est} \end{bmatrix} = \mathbf{H}(t) * \begin{bmatrix} \tilde{X}_\alpha(t) \\ \tilde{Y}_\alpha(t) \end{bmatrix} , \tag{5.10}$$

with the optimal filter matrix $\mathbf{H}(t)$ taking the general form

$$\mathbf{H}(t) = \begin{bmatrix} g_1 \cos(\Omega t - \phi) & g_2 \sin(\Omega t) \\ g_3 \sin(\Omega t) & g_4 \cos(\Omega t + \phi) \end{bmatrix} e^{-\Gamma t} . \tag{5.11}$$

where g_n, Ω, and ϕ are positive real numbers. This filter function, in the parametrically driven case, assumes that $\chi < \Delta$ and that the quadratures are rotated by an angle α such that $X_\alpha - X_{\alpha\rm est}$ is maximally squeezed.

In the undriven case, the filter is simplified by the restrictions $g_n = g_0$ (for all n), and $\alpha = \phi = 0$. Here, the rotation frequency Ω_0 is kept to account for drifts in f_0. The remaining parameters Γ and g_0 are functions of SNR.

Phase-space Brownian trajectories $\{X, Y\}$ determined from the high-fidelity measurement are plotted in Fig. 5.8b, along with corresponding residual noise $\{X–X_{\rm est}, Y–Y_{\rm est}\}$ after applying the optimised filter to the low-fidelity measurements in the low, intermediate and high SNR

regimes. As expected, when no parametric drive is applied, the quadratures of motion have equal uncertainty, determined by the optimal conditional variance i.e. $V_X = V_Y = V_0$. As the thermal signal increases towards the noise floor (SNR approaches 1) the conditional variances drop sharply as expected. At maximum sideband intensity, the RMS uncertainty in both quadratures is reduced from the thermal value of 240pm to 60pm, corresponding to an effective temperature decrease from 300K to 19K. The dependence of this conditional variance on SNR fits theory well, as shown in Figure 5.10.

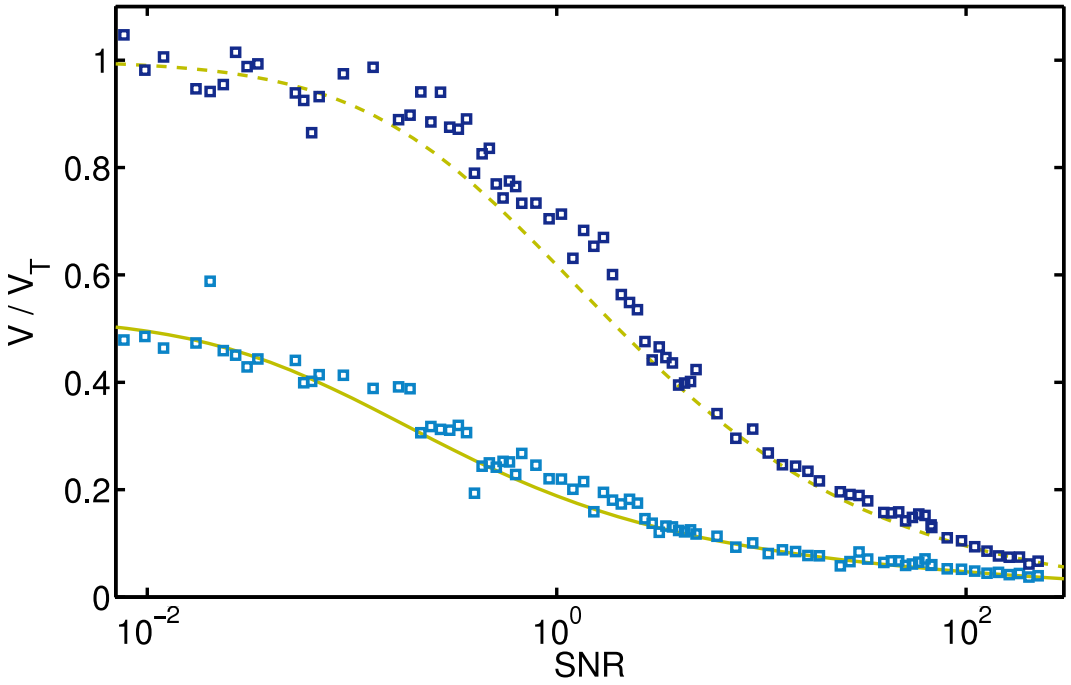

Figure 5.10: Conditional variance V_0 (dark squares) and conditional squeezed variance V_α (light squares), normalised to the thermal variance V_T, as a function of SNR.

With the drive turned on, the high-fidelity measurement shows unconditional thermomechanical squeezing close to, but not surpassing, the 3dB limit. Critically, elliptical trajectories can be observed, establishing the correlations required for our estimation protocol between squeezed and antisqueezed quadratures. These correlations can also be clearly seen in Figure 5.9. After subtracting the optimal estimate, the residual noise is maximally squeezed at an angle α that increases with SNR. The variance $V_{X\alpha}$ of this quadrature decreases monotonically as the measurement improves, and is shown in Figure 5.10. As expected, the conditional variance drops earlier than for the undriven case. Eventually, in the high SNR limit, the measurement bandwidth is greater than the rate of any coherent dynamics and the residual noise becomes independent of amplification.

The squeezing ratio $V_{X\alpha}/V_0$ determined from this analysis is shown in Fig. 5.11 as a function of SNR, agreeing well with theory. As expected, the variances reproduce the unconditional squeezing in the weak measurement limit and the parametric drive has no effect in the strong measurement limit. However, in the intermediate regime where SNR ≈ 1 there is a distinct

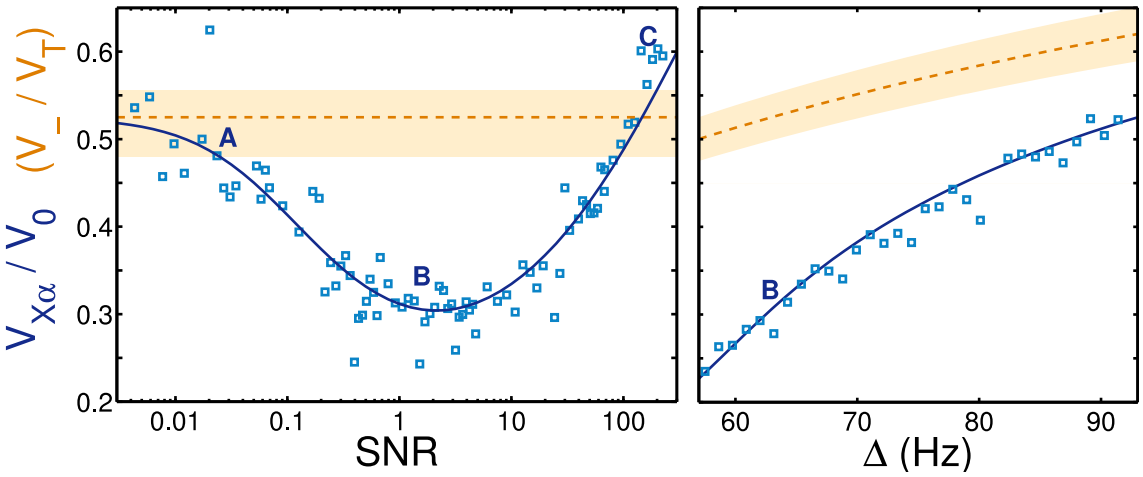

Figure 5.11: Steady-state squeezing using optimal estimation. Squeezing ratios are plotted against SNR for $\Delta = 63$Hz (left) and against detuning for SNR ≈ 1 (right). Blue points show the squeezing ratio, with theoretical fits shown as solid lines. Dotted red curves are fits to the squeezing without estimation, limited to 1/2, with shaded bands to represent the experimental error margin. Labels A-C indicate the datapoints used to generate the trajectories in Figure 5.8.

minimum, allowing enhanced localisation and breaking the 3dB limit by a significant factor. As can be seen in Fig. 5.11 (right), the squeezing can be improved further by adjusting the detuning closer to threshold, with a maximum thermomechanical squeezing of 6.2dB achieved. These results can be understood by the fact that the effective increased sensitivity due to the parametric drive is of greatest benefit near the noise floor and with maximal amplification of the orthogonal quadrature. Since the maximum squeezing is proportional to $\sqrt{\chi/\gamma}$, it can be enhanced by increasing the parametric drive strength, subject to the condition $\chi \ll f_0$. In principle, this allows arbitrary suppression of one quadrature of motion, exceeding the usual limit for control systems defined by the measurement precision.

5.5 Discussion

A significant practical challenge in using a very strong parametric drive was presented by the frequency drift of the cantilever. Since a very large DC voltage was used to maximise the parametric drive, the mechanical frequency became extremely dependent on the relative positions of the cantilever and electrode. As shown in Appendix B, this led to a need for constant manual fine-tuning of the DC voltage over experimental runs. However, modern MEMS and NEMS are generally fabricated with electrodes defined on the same chip as the oscillator[60, 110, 56, 24]. In these devices, however, a challenge is presented in choosing a geometry so that a DC voltage does not degrade the oscillator Q[111].

For applications requiring confinement in addition to localisation, optimal estimates must be calculated in real-time in order to be fed back as a damping force. This can be achieved

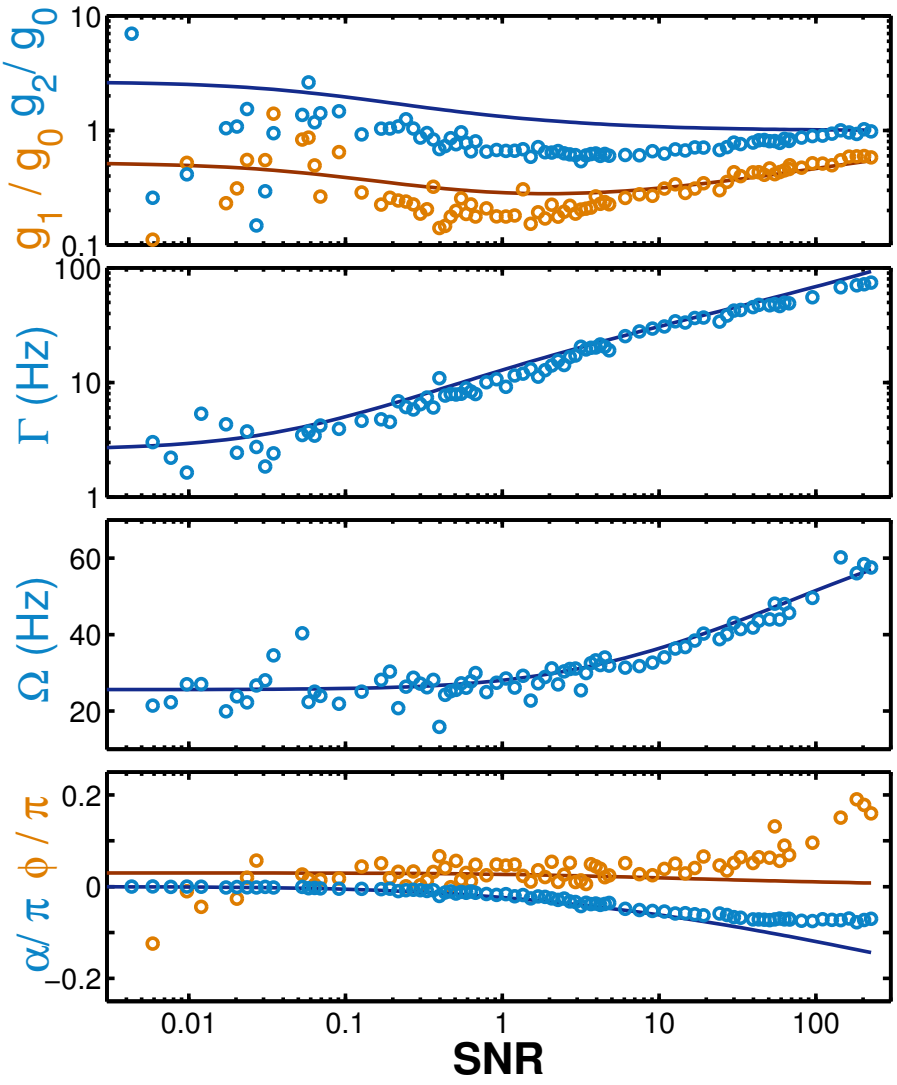

Figure 5.12: Optimal filter parameters. Solid lines indicate theoretical parameters for $\chi = 57\text{Hz}$,$\gamma = 2.6\text{Hz}$ and $\Delta = 63\text{Hz}$. Circles indicate parameters obtained from post-processing.

by using the well-defined filter parameters in Section 4.8. The filter parameters obtained by experimental optimisation, shown in Figure 5.12, agree reasonably well with these theoretical estimates, yet are more likely to converge to consistent values in the higher-fidelity regime. While the rotation frequency Ω and bandwidth Γ agree well with theory, there is an unknown systematic error in the optimal gains. The error in the optimal squeezing angle α at high SNR can be attributed to a very shallow minimum in this regime.

Although demonstrated with thermal fluctuations, our technique applies in the same manner to the zero-point motion of an oscillator, with the maximum reduction in conditional variance $V_{X\alpha}/V_0$ independent of temperature. The effect of the quantum modification at low temperatures—known as backaction noise—is instead to limit the initial conditional variance V_0 to be no lower than the ground state variance. Therefore our approach could enable strong quantum squeezing and ultra-precise quantum control[89]. Experiments with sensitivity near the standard quantum limit (where SNR ≈ 1 at zero temperature) have been recently performed

with mechanical oscillators[91, 39]. While purely measurement-based schemes exist to create mechanical squeezed states[46], significant squeezing requires high measurement strength and efficiency such that SNR $\gg (2N_{th}+1)^2$. This regime is yet to be demonstrated in mechanical oscillators.

In principle, the technique we have demonstrated can be easily ported to state-of-the-art mechanical devices. Nanoelectromechanical systems are commonly integrated with a parametric drive and can be pre-cooled to near the ground state[112]. Such emerging systems are therefore good candidates for quantum squeezing below the zero-point motion using our technique, even without significant advances in transduction.

We have observed parametric thermomechanical squeezing of a micromechanical oscillator exceeding 3dB for the first time, both transient and in equilibrium, with the latter breaking a well-known limit for parametrically driven systems. This result demonstrates that the 3dB limit to steady-state parametric squeezing is not fundamental, and facilitates the wider use of thermomechanical squeezing in control and sensing applications. The combination of parametric driving, measurement and estimation sheds light on the important interface between quantum measurement and control that is being approached most notably in opto- and electromechanical systems. The techniques introduced, if applied in conjunction with state-of-the-art readout techniques and high quality oscillators, also open the door for the engineering of nonclassical states of mesoscopic mechanical systems. More broadly, our results demonstrate that combining oscillator nonlinearity with control can both overcome fundamental limitations on parametric processes, as well as localise mechanical motion beyond constraints imposed by the measurement sensitivity.

Chapter 6

QND measurement and quantum squeezing via parametric amplification

6.1 Introduction

Unlike classical systems, the strength of any continuous measurement of a quantum system plays an important role in its dynamics, with the optimal strength depending on the application. Many uses are being found for weak measurement[77], while quantum non-demolition (QND) techniques such as back-action evasion work best in the strong measurement limit[46, 49]. In other cases, such as gravity-wave detectors, measurement strength near the standard quantum limit is preferred[35].

For preparation and measurement of quantum states, backaction evasion in the strong measurement regime is a widely sought-after goal[46, 91, 113, 114]. The purpose of backaction evasion is to provide better resolution in a quantum measurement without adding noise to the observable being measured. If the conditional variance is below that of the zero-point motion, a squeezed state can be created. While parametric amplification is also widely known as a means to improve resolution, this generally comes at the cost of disturbing the measured observable.

In the previous two chapters, it was shown and demonstrated experimentally that detuned mechanical parametric amplification may improve the effective resolution of a quadrature of motion without increasing its variance. In general, this is due to a mutual dynamical coupling between the amplified and squeezed quadratures. In this chapter, this scheme will be examined in the regime of low temperature and measurement sensitivity near the level of the zero-point motion, such that backaction noise becomes important. The in-principle unlimited improvement in conditional variance of a quadrature, shown in Chapters 4 and 5, may then result in a squeezed state.

Notably, the special case encountered in Section 4.4.1, where one quadrature is not disturbed at all by the parametric drive, becomes significant in a quantum context. In this case, the undisturbed quadrature can be considered a QND observable. Therefore, it can be shown

that it is possible to equate a weak measurement of the oscillator to a strong but imperfect backaction evading measurement. This allows us to quantify the effectiveness of DMPA as a QND measurement, and hence directly compare DMPA to one-mode backaction evading protocols as used in cavity optomechanics[46, 115, 48], as well as a more recently studied two-mode version[114].

In this chapter, an effective measurement strength is derived in the QND case, aiding the comparison between parametric QND scheme and backaction evading measurement. It is then shown that in the regime where the oscillator is localised well below the zero-point motion, the effective measurement strength scales linearly with the parametric drive strength. Hence, conditional quantum squeezing of the mechanical state with weak or inefficient measurement, or in the optomechanical bad cavity regime, is made possible with parametric driving. In addition it is shown that, in contrast to backaction evasion, approaching the limit of perfect squeezing does not degrade the purity. Furthermore, the purity scales more favourably with the measurement efficiency and is therefore more robust to measurement loss.

Finally, since quantum squeezing is ultimately limited by the temperature of the oscillator, it is natural to ask whether combining DMPA with resolved sideband cooling allows an increased amount of squeezing. To that end, a master equation that includes resolved sideband cooling is introduced and the potential of this system for producing squeezed states in the good cavity limit is examined in Section 6.4.

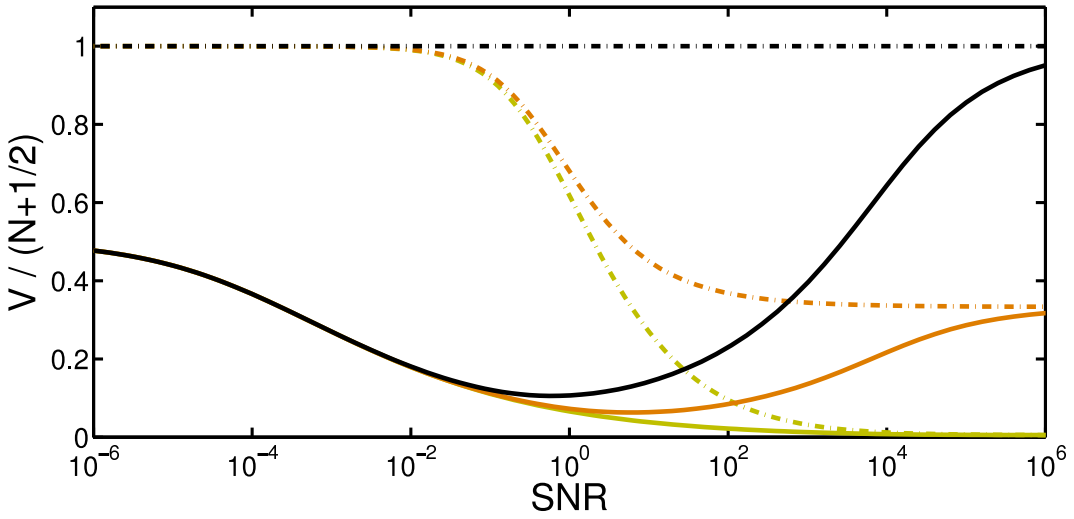

Figure 6.1: Conditional variance normalised to thermal variance $N+1/2$, for a quadrature with no parametric drive (V_0, dotted lines) and in the squeezed quadrature with the drive $\chi = 100\gamma$ and detuning at threshold ($V_{X\alpha}$, solid lines). Initial phonon numbers are $N = 100$ (light), $N = 1$ (medium) and $N = 0$ (dark). Perfect efficiency is assumed. The increase in squeezed variance at high SNR and low temperature demonstrates the effect of back-action on quantum squeezing.

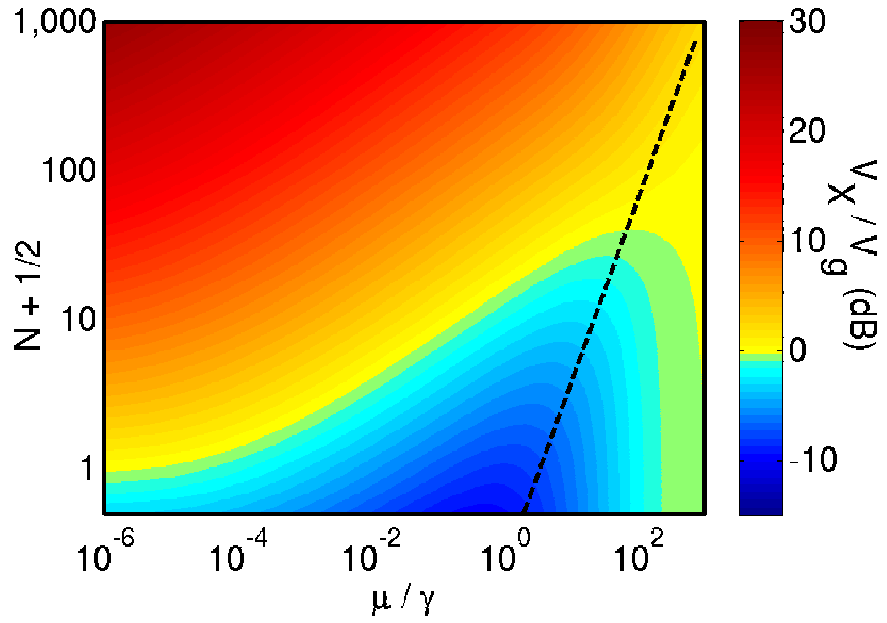

Figure 6.2: Colour plot of the ratio of squeezed variance to ground-state variance for $\chi = \Delta = 100\gamma$ and $\eta = 1$. A ratio less than unity indicates quantum squeezing. The dashed line indicates $\mu/\gamma = N + 1/2$, beyond which back-action is dominant.

6.2 Quantum squeezing

Firstly, the results of Chapter 4 are transported to the quantum regime by simply considering the absolute variance, rather than the variance relative to the undriven conditional variance V_0. In this case, backaction needs to be taken into account. Figure 6.1 shows the variance normalised to the thermal variance $N + 1/2$ for three values of N, with a detuned parametric drive at threshold. In the weak measurement limit, the limiting 3dB of relative squeezing is produced.

As the SNR approaches the intermediate measurement regime, the squeezed conditional variance $V_{X\alpha}$ starts to significantly reduce at a lower SNR than the bare conditional variance V_0, justifying a description of an enhanced effective measurement strength. Finally, in the high SNR limit, the conditional variance in each case asymptotes to the ground state level due to backaction. At high temperatures, the backaction is negligible and the limit of this ratio is essentially zero as in Fig. 4.4. However, at low temperatures, the backaction makes up a significant part of V_T and the ground-state limit is noticeable. Notably, this ground-state limit is clearly approached from below in the parametrically driven case. Note that the strong measurement limit is also where the undriven conditional variance V_0 "catches up" to the driven conditional variance. However, as discussed previously, this is unrelated to backaction. This can be seen by the ratio $V_{X\alpha}/V_0$ considered in Chapters 4-5, which even without backaction approaches unity in the strong measurement limit.

At an initial ground state, the optimal regime SNR ≈ 1 is only on the cusp of the back-

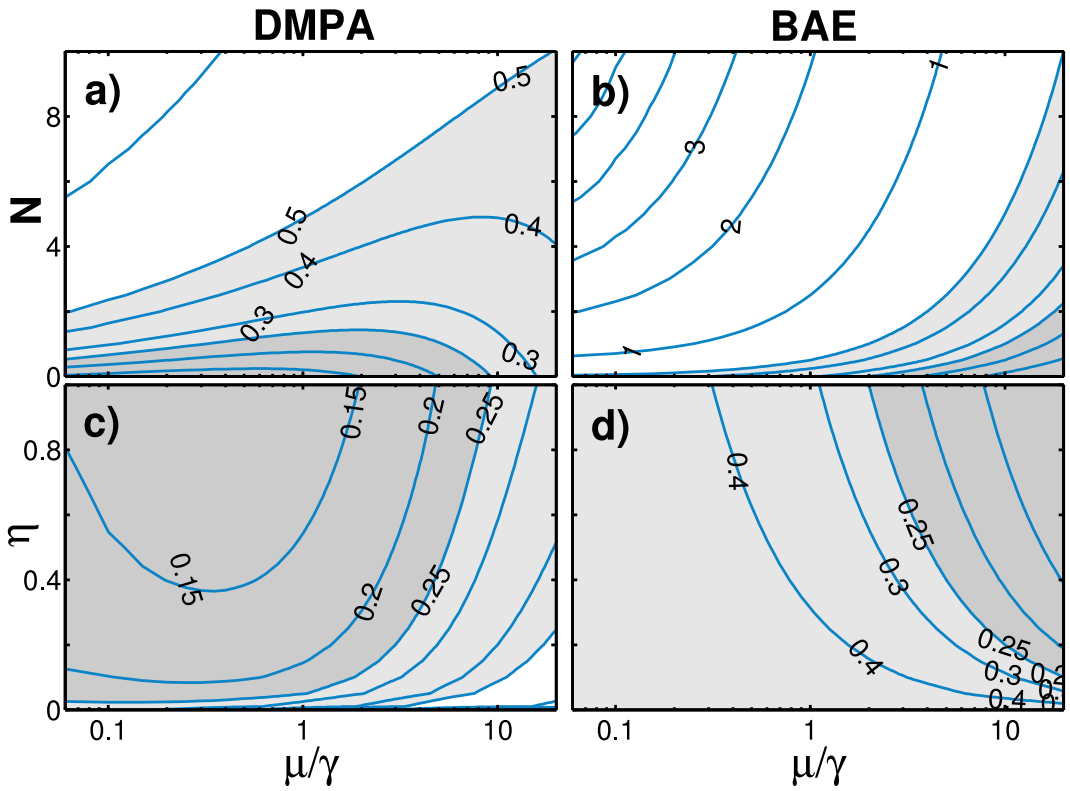

Figure 6.3: Optimal quantum squeezing generated by DMPA with $\chi/\gamma = 50$ (a,c) and by BAE (b,d). $V_{X\alpha}$ is shown as a function of μ/γ and N in (a,b) for $\eta = 1$, and as a function of μ/γ and η in (c,d) for $N = 0$. Shaded areas denote squeezing below the zero-point motion (light) and the standard 3dB MPA limit (dark).

action dominated regime (assuming the efficiency is near unity). To fully illustrate the effect of the parametric drive and estimation at low temperature, $V_{X\alpha}$ is plotted for various μ and low values of N in Figure 6.2. Squeezing of the conditional variance below the zero-point motion is achieved when $V_{X\alpha} < V_g = 0.5$, which is possible even from relatively high initial temperatures or with inefficient detection. The appearance of an optimum measurement strength μ at low temperature is in stark contrast with the best possible squeezing using a resonant drive, which degrades steadily from a minimum $0.5V_g$ at $\mu = 0$ to $0.73V_g$ at $\mu = \gamma$.

Even more notably, this scheme vastly outperforms back-action evasion in this parameter regime. The absolute variance $V_{X\alpha}$ is shown in Fig. 6.3 for $\chi/\gamma = 50$, compared to that achievable by ideal BAE (where $N_{\rm bad} = 0$ [46]). For this drive strength, the DMPA method produces squeezing for $N < 5$ at $\mu/\gamma \approx 1$. At this measurement strength, a BAE scheme would require $N < 0.5$. The dependence on efficiency η is similar to that for backaction evasion, as in both cases decreasing η has a similar effect to decreasing μ. Importantly, by choosing DMPA over BAE, the need for an often impractical modulation of the measurement strength is eliminated.

Unconditional squeezing can be achieved by using a linear feedback force (e.g. from a separate electrode) to stabilize the mean values[89]. This relies on high mechanical Q so that the

delay in converting momentum feedback into physical displacement can be neglected. While DMPA with feedback is more complicated than squeezing by above-threshold resonant parametric driving and feedback stabilisation[100], verification of squeezing can take place on a much shorter timescale. In this sense, DMPA is similar in essence to backaction evasion, as will now be discussed in detail.

6.3 QND measurement via parametric driving

As shown above, the squeezing due to DMPA is maximised at the instability threshold $|\Delta_{\rm th}| = \sqrt{\chi^2 - \gamma^2}$, where the quadratures are mutually coupled in hyperbolic trajectories. In Section 4.4.1, it was shown that near this threshold is a case where one quadrature is unaffected by the parametric drive. For example, one obtains extremely simple dynamics in the case where $\Delta = -\chi$, as the Hamiltonian takes the form

$$\tilde{H} = -\frac{\hbar\chi}{2}\left(\hat{X}^2 + 1\right) . \tag{6.1}$$

Since $\hat{X}$ commutes with the Hamiltonian, it is a constant of motion (but is subject to damping and noise from the bath). The $\hat{Y}$ quadrature, on the other hand, evolves with a time-derivative proportional to $\chi\hat{X}$. As shown by Eqs (4.21-4.22), $\hat{Y}$ approaches an amplified, but filtered, version of $\hat{X}$ for a large value of χ. This means that a standard continuous position measurement effectively becomes an efficient QND measurement of $\hat{X}$. Since this special case resembles backaction evasion, an analogous effective measurement strength can be defined. Due to the simplified dynamics, simple analytic solutions for the conditional variances and purity can also be obtained. Later, the respective roles of the parametric drive and measurement are clarified using the general solution for the effective measurement strength.

6.3.1 Effective measurement strength

Inserting the Hamiltonian given by Eq. (6.1) into the master equation (3.22), the conditional variances undergo a somewhat simplified evolution

$$\frac{d}{dt}V_X = -2\gamma V_X + 2\gamma(N + 1/2 + N_{BA}) - 4\eta\mu(V_X^2 + C^2) \tag{6.2}$$

$$\frac{d}{dt}V_Y = -2\gamma V_Y + 4\chi C + 2\gamma(N + 1/2 + N_{BA}) - 4\eta\mu(V_Y^2 + C^2) \tag{6.3}$$

$$\frac{d}{dt}C = -2\gamma C + 2\chi V_X - 4\eta\mu C(V_X + V_Y) , \tag{6.4}$$

Note that in this section, we are interested in the undisturbed quadrature X rather than the maximally squeezed quadrature X_α. Therefore we do not make any rotations, keeping the covariance C at a finite value. Solving for the stationary value of the covariance, we obtain

$$C = \frac{\chi}{\gamma + 2\eta\mu(V_X + V_Y)}V_X \equiv gV_X . \tag{6.5}$$

Unlike the BAE case, here the stationary value of C is non-zero. We now use this result to eliminate C from the steady-state equation of motion for V_X, obtaining

$$0 = -2\gamma V_X + 2\gamma(N + 1/2 + N_{\mathrm{bad,eff}}) - 4\eta\mu_{\mathrm{eff}}(V_X, V_Y)V_X^2 \ , \tag{6.6}$$

where we have described the effective measurement strength:

$$\mu_{\mathrm{eff}}(V_X, V_Y) = \mu\left(1 + \frac{C^2}{V_X^2}\right) \tag{6.7}$$

$$= \mu(1 + g^2) \ , \tag{6.8}$$

and introduced an effective bad-cavity parameter

$$N_{\mathrm{bad,eff}} = \mu/(2\gamma) \ . \tag{6.9}$$

Comparing against Eq. (3.45) describing backaction evasion, we see that Eq. (6.6) is now of the same form. For a large measurement enhancement ($g \gg 1$), there is a strong similarity to a near-ideal QND measurement of the X quadrature in that the measurement conditioning parameter μ_{eff} is enhanced far above μ without a coinciding increase in the backaction heating $N_{\mathrm{bad,eff}}$, which is independent of g. When $g \gg 1$, detuned parametric amplification in the bad cavity regime is therefore equivalent to a strong back-action evading measurement in the resolved sideband regime $\kappa < \omega_m$. In this case, the spurious heating of the meaurement given by Eq. (6.9) can be written

$$N_{\mathrm{bad,eff}} = \frac{N_{\mathrm{BA,eff}}}{1 + g^2} \ . \tag{6.10}$$

where $N_{\mathrm{BA,eff}} = \mu_{\mathrm{eff}}/(2\gamma)$. Equating this to the BAE spurious heating given by Eq. (3.44) produces an equivalent cavity linewidth

$$\kappa = \frac{4\sqrt{2}\omega_m}{\sqrt{g^2 + 1}} \tag{6.11}$$

Therefore the limit $g \gg 1$ is equivalent to the good cavity limit, and the equivalent linewidth here scales inversely to g.

Equation (6.5), while not an explicit solution, provides some insight into the behaviour of $g = C/V_X$ in various regimes. In the complete absence of measurement ($\mu = 0$), the coherent amplification alone determines the covariance so that $g = \chi'$ (where from here onward χ' denotes the dimensionless ratio χ/γ, equalling unity at the self-oscillation threshold of a non-detuned parametric amplifier). The measurement strength is therefore simply enhanced by a factor of $1 + \chi'^2$, which is the ratio of unconditional Y and X variances. As the measurement strength is increased, the ratio g is attenuated by the conditioning of the quadratures. This can be seen in Eq. (6.5), where even though increasing μ reduces V_X and V_Y, the product $\mu(V_X + V_Y)$ is a monotonically increasing function of μ. This attenuation of g reflects the fact that the damping effect of the position measurement on the covariance counteracts the coherent amplification due

to the parametric drive. In the limit of a perfect measurement ($\mu/\gamma \to \infty$), g approaches zero and the parametric drive becomes irrelevant.

A bandwidth picture provides a useful heuristic explanation for the form of Eq. (6.5), as follows. The measurement conditioning terms $\eta\mu V_X$ and $\eta\mu V_Y$ in this equation also appear in Eqs (6.2) and (6.3), where they may be understood as damping rates in addition to the intrinsic rate γ. Accordingly, the conditioning associated with a position measurement makes use of information gathered over time-scales $1/(\eta\mu V_X)$ and $1/(\eta\mu V_Y)$. However, the effective amplification dynamics are only significant on timescales longer than the mechanical decay time, given by $1/\gamma$. This is shown by Eq. (4.21), where the additional term in $\hat{Y}(\omega)$ decays for $|\omega| \gg \gamma$. Therefore, for sufficiently short measurement timescales the amplification is effectively frozen out and plays no role in the conditioning.[1] This explains the appearance of the rates $\eta\mu V_X$ and $\eta\mu V_Y$ as attenuating terms in the measurement gain given by Eq. (6.5).

6.3.2 Strong driving limit

Since Eq. (6.5) is an implicit equation, the net effect of the parametric drive and measurement in the regime where the measurement is significant ($2\eta\mu(V_Y + V_X) \gg \gamma$) is not immediately clear. For instance, increasing χ' will further increase the amplified variance V_Y, while increasing the measurement strength μ will condition V_Y to a smaller value. The situation simplifies in the case of a strong parametric drive ($\chi' \gg 1$), such that the squeezing is strong and $V_Y \gg V_X$. The net heating of V_Y is then found by keeping only the μV_Y term in the denominator of Eq. (6.5) so that

$$C \approx \chi V_X / 2\eta\mu V_Y \ , \tag{6.12}$$

and substituting this into Eq. (6.3). A cubic equation is then obtained for V_Y in the steady-state, with the solution

$$V_Y \approx \left(\frac{\chi}{\eta\mu}\right)^{2/3} \left(\frac{V_X}{2}\right)^{1/3} \ . \tag{6.13}$$

Inserting this back into Eq. (6.12), and then into Eq. (6.2) using the steady-state condition gives an equation for V_X that can be solved

$$0 = -2\gamma V_X + 2\gamma(N + 1/2 + N_{BA}) - 4\eta\mu V_X^2 - (4\chi^2\eta\mu)^{1/3} V_X^{4/3} \ . \tag{6.14}$$

We can see that the extra conditioning term due to the covariance is now proportional to $V_X^{4/3}$. That is, in the regime where the measurement and parametric drive are both significant, the overall effect of the conditioning via the Y quadrature lies between that of damping (linear in V_X) and that of direct conditioning (quadratic in V_X).

[1] A rigorous approach to this argument is given in Appendix C.2 by the filter width parameter used to obtain the optimal position estimate from the measurement results.

In the strong driving limit, V_X becomes small enough that the terms proportional to V_X and V_X^2 in Eq. (6.14) can be neglected, yielding the simple solution

$$V_X \approx \left[\frac{(2N + 2N_{\mathrm{BA}} + 1)^3}{4\chi'^2\eta\mu/\gamma}\right]^{1/4} . \tag{6.15}$$

Since N_{BA} is proportional to the measurement strength μ, there is clearly an optimum value of μ that minimises V_X, located around where this backaction term becomes important. Differentiating to find the optimal measurement strength in this limit yields

$$\mu_{\mathrm{opt}}(\chi' \to \infty) = \gamma(N + 1/2) , \tag{6.16}$$

which corresponds to the backaction noise equalling half of the original noise in the oscillator. This trade-off between conditioning and backaction is in contrast to backaction evasion, where the conditional variance of the measured quadrature decreases monotonically with μ, even with spurious heating. Interestingly, this trade-off resembles that encountered in ultra-sensitive force measurement, with the standard quantum limit residing in the same measurement regime.

Substituting this optimal measurement strength back into Eq. (6.15) leaves

$$V_X \approx \frac{3^{3/4}}{2\eta^{1/4}}\sqrt{\frac{2N+1}{\chi'}} , \tag{6.17}$$

Therefore, arbitrarily strong quantum squeezing of the X quadrature is possible if $\chi' \gg 2N+1$. In this limit, the X quadrature is closely aligned with the optimally squeezed quadrature considered in section 6.2. This can be compared with the variance obtained for backaction evasion in the strong measurement regime (where $\mu/\gamma \gg 1$)

$$V_X \approx \frac{1}{\eta^{1/2}}\sqrt{\frac{2N+1}{\mu/\gamma}} . \tag{6.18}$$

Notably, the DMPA scheme is clearly more suited to a sub-optimal efficiency η, consistent with the numerical analysis in Section 6.2. This is especially relevant to nanomechanical systems, where even the best state-of-the-art optomechanical devices have loss factors of the order of 10%[116].

6.3.3 Squeezing comparison

We can now easily see that setting μ to near the backaction-dominated regime allows the equivalent QND measurement strength μ_{eff} to be deeply within it. Measurement of the proxy $\hat{Y}$ quadrature can therefore be used to condition the $\hat{X}$ quadrature to below the level of the zero-point motion. This can be shown in the general case by using numerical solutions to Eqs (6.2-6.4). Figure 6.4 shows the minimum parametric drive strength required to achieve a fixed level of quantum squeezing using the optimum measurement rate μ_{opt}, as well as the purity of the final conditional state. The required measurement strength and achievable purity for

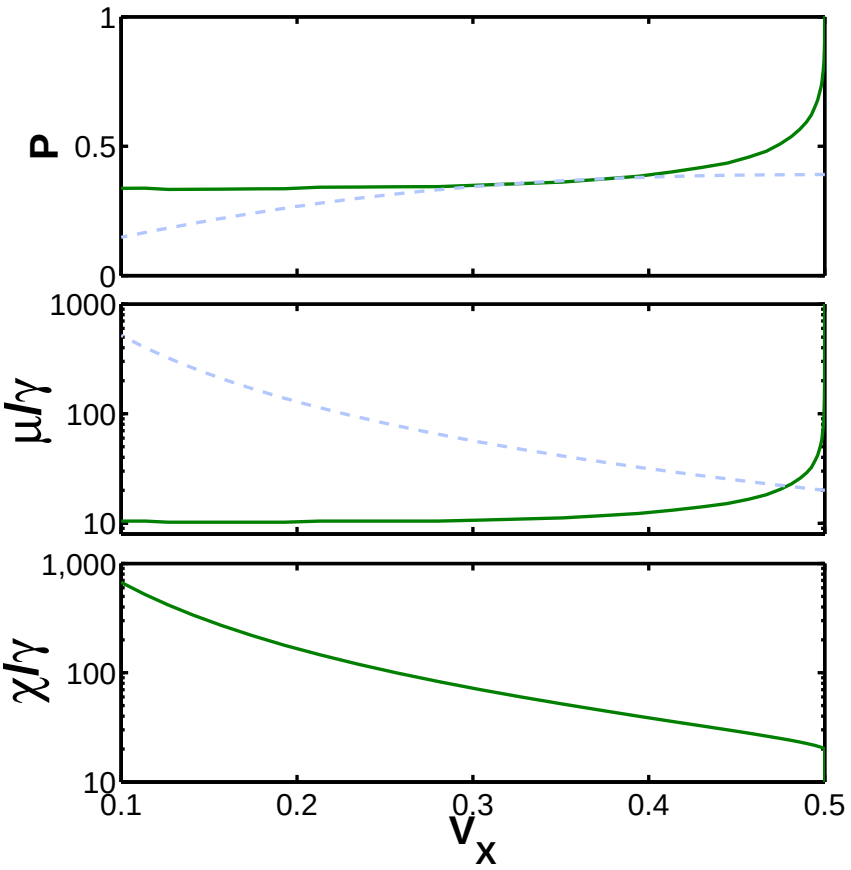

Figure 6.4: Comparison of purity and key parameters for ideal backaction evasion (light, dashed lines) and optimal detuned parametric amplification (solid lines) in the quantum squeezing regime $V_X < 0.5$. For DMPA, the measurement strength μ (middle panel) is optimised to minimise the squeezed variance for each parametric drive strength χ/γ (lower panel). In both cases, the set parameters are an efficiency of $\eta = 1$ and the mean thermal phonon occupation of $N = 10$.

backaction evasion are shown for comparison. In the limit of strong squeezing, the parametric drive takes over the measurement's role in backaction evasion, while the optimal measurement strength approaches the constant given by Eq. (6.16) as expected. For low temperatures, this is currently an experimentally feasible parameter, with recent electromechanical[117] and optomechanical[115, 48] experiments demonstrating backaction noise exceeding zero-point and thermal fluctuations ($\mu > 2\mu_{\rm opt}$).

With the measurement strength optimised, the squeezing is limited only by the normalised parametric drive strength χ'. As in the rest of this thesis, the rotating wave approximation forces the restriction $\chi' \ll Q$, where $Q = \omega_m/\gamma$. Experimental limits on χ' are also set by the linear response range of the resonator, since the antisqueezed quadrature has variance exceeding the thermal variance by a factor of $1 + \chi'^2$. Finally, the condition $\Delta = \pm\chi$ requires precise frequency control of both the resonator and parametric modulation to avoid the instability

threshold $|\Delta_{\rm th}| = \sqrt{\chi^2 - \gamma^2}$, which becomes closer with increasing χ'. Therefore, environmental influences on the oscillator frequency such as temperature fluctuations are detrimental in the strong driving regime, as is also the case for backaction evading protocols[113].

6.3.4 Purity comparison

So far in this analysis, the parallels between DMPA and backaction evasion have been demonstrated for the dynamics and statistics of the $\hat{X}$ quadrature. It is interesting to note that these parallels do not extend to the orthogonal $\hat{Y}$ quadrature, which is amplified and conditioned in the DMPA scheme rather than heated. The variance of the $\hat{Y}$ quadrature is relevant to future quantum applications, many of which rely on a pure or almost-pure squeezed Gaussian state as a building block, as discussed in Section 2.2. To illustrate the difference between the two schemes considered, we compare the quantity $P = V_g^2/(V_X V_Y - C^2)$, which reaches a maximum value of one for a pure state.

For a backaction evading measurement, the purity can be obtained from the solutions of (3.45-3.47)

$$P_{\rm BAE} = \frac{\eta}{1+\gamma(2N+1)/\mu} \, \frac{2}{\sqrt{1+4\eta\mu(2N+2N_{\rm bad}+1)/\gamma}-1} \, . \tag{6.19}$$

In the ideal good cavity limit $N_{\rm bad} = 0$ and for a strong measurement $\eta\mu' \gg 2N+1$, the backaction causes a decrease in purity towards zero as μ is increased

$$P_{\rm BAE}(\eta\mu/\gamma \gg 2N+1) \approx \sqrt{\frac{\eta\gamma}{\mu(2N+1)}} \, . \tag{6.20}$$

In contrast to the above, the purity of the steady-state conditional state after applying a detuned parametric drive with the QND condition $|\Delta| = \chi$ and $\mu \neq 0$ can be derived from the general solutions (see C.1), and written as

$$P_{\rm DMPA} = \frac{\eta}{1+\gamma(2N+1)/\mu} \left(1 + \frac{2}{\chi'/g - 1}\right) \, . \tag{6.21}$$

In the limit of weak measurement, this purity approaches a very small value due to the amplification of the Y quadrature. However, with an intermediate measurement strength, the conditioning of the Y quadrature allows for a higher purity than the equivalent backaction evading measurement. Since $\chi'/g - 1$ is always positive, it is possible to assign a lower bound from the above that is independent of the parametric drive

$$P_{\rm DMPA} > \frac{\eta}{1+\gamma(2N+1)/\mu} \, . \tag{6.22}$$

In the strong measurement limit this lower bound on the purity approaches η, in contrast to Eq. (6.19) where the purity approaches zero for backaction evading measurement. This difference is attributed to the fact that in the DMPA scheme, both quadratures are conditioned by the measurement. Therefore, even though the $\hat{Y}$ variance is amplified, this quadrature is

still kept confined by a nonlinear conditioning term. In contrast, backaction evasion heats the unmeasured $\hat{Y}$ quadrature, causing V_Y to increase linearly with μ'.

If we consider the optimal measurement strength μ_{opt} that minimises V_X with a fixed parametric drive χ, the purity is reduced from the maximum of η. This purity is plotted in Figure 6.4 for a squeezed $\hat{X}$ variance (i.e. $V_X < 1/2$), where it is compared with the backaction evading case. It can be clearly seen that while the purity deteriorates as squeezing improves for backaction evasion, the DMPA purity approaches the lower bound of $\eta/3$ (since in this limit $\mu_{\text{opt}}/\gamma \to N + 1/2$ and $\chi' \gg g$). Furthermore, a compromise can be made by increasing the measurement strength beyond the optimal level, reducing the strength of QND squeezing of the X quadrature in return for higher state purity. This preservation of purity in the strong squeezing limit is in stark contrast to conventional QND quadrature measurement of an oscillator and other methods for steady-state mechanical squeezing. One notable recent proposal using dissipative optomechanics results in purity scaling more favourably than for backaction evasion[118], however in this case the purity also degrades in the strong squeezing limit.

6.3.5 General solution for effective measurement strength

Some additional light can be shed on the parallel between DMPA and backaction evasion by quantifying the effective measurement enhancement μ_{eff}/μ. This was found to be equal to $(1 + \chi'^2)$ in the limit of no measurement, and reduced to unity in the strong measurement limit. It is between these two limits, where weak measurement and strong parametric driving work in concert, that our scheme finds utility in QND measurement. This intermediate regime — described above for the limit of strong driving — will now be examined in detail. Making use of already derived exact solutions to Eqns (6.2-6.4), we can explicitly find μ_{eff} in terms of experimental parameters. This also allows direct comparisons to be made with state-of-the art backaction evasion experiments.

The ratio μ_{eff}/μ, quantifying the ratio of conditioning measurement to backaction-inducing measurement, is given by (see Appendix C.1)

$$\frac{\mu_{\text{eff}}}{\mu} = \frac{2(1+\chi'^2)}{1+\sqrt{(1+4\text{SNR})^2+16\chi'^2\text{SNR}}-4\text{SNR}}\,, \tag{6.23}$$

where $\text{SNR} = \eta\mu(2N + 2N_{\text{BA}} + 1)/\gamma$ defines the signal-to-noise ratio with which the combined thermal and back-action driven motion can be resolved over the measurement noise in the absence of driving. Since $N_{\text{BA}} \propto \mu$, the inclusion of backaction means that in the limit $N_{\text{BA}} \gg N + 1/2$, the SNR becomes quadratic in μ rather than linear.

As SNR is increased, the effective measurement enhancement given by Eq. (6.23) passes through three regimes, as illustrated in Figure 6.5 for three values of χ'. For a strong drive ($\chi' \gg 1$), these regimes have simple, well-defined boundaries. The weak measurement limit, where the enhancement is maximised, ends when $\text{SNR} \approx \chi'^{-2}$. Beyond this is an intermediate region of nonzero but reduced gain, where the term $\chi'^2\text{SNR}$ is dominant in the denominator

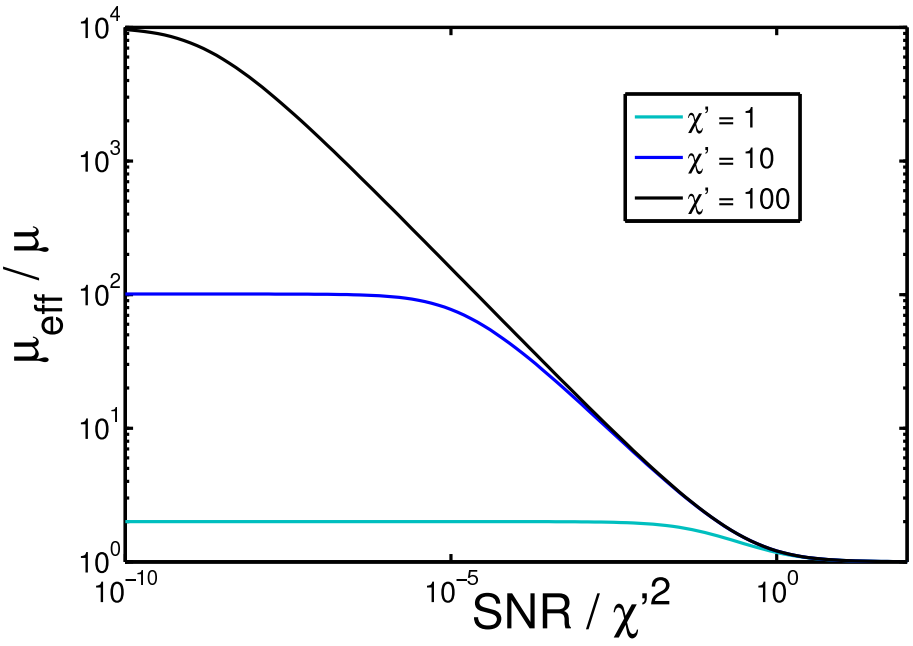

Figure 6.5: Effective enhancement of the measurement strength as a function of the combined parameter SNR/χ'^2. For each trace, χ' is kept constant. The far-left limit corresponds to the weak-measurement limit, where the maximum enhancement is determined by χ'. On the far right, in the strong measurement limit, the enhancement disappears. In the intermediate region, the gradient is approximately $-1/2$, indicating a linear increase of μ_{eff} with χ.

of Eq. (6.23). This corresponds to the amplified $\hat{Y}$ quadrature being well transduced above the measurement noise. Comparing to Eq. (6.5), this is also where the term μV_Y becomes important and the effective measurement ceases to be dominated by the coherent parametric drive. Finally, when SNR exceeds χ'^2, the direct measurement of the X quadrature is more efficient than the proxy measurement and μ_{eff}/μ approaches 1.

To utilise the full performance of the DMPA-based backaction evasion scheme, the effective measurement strength μ_{eff} must be large compared to γ, while the spurious heating N_{BA} must be weak compared to the thermal noise. It is in the aforementioned intermediate regime that this occurs and the level of quantum squeezing is optimised. When $\chi' \gg 1$ this regime corresponds to an SNR of order unity, signifying that the thermal motion is barely transduced without the aid of the parametric drive. We can then simplify Eq. (6.23) to

$$\frac{\mu_{\mathrm{eff}}}{\mu} \approx \frac{\chi'}{2\sqrt{\mathrm{SNR}}} \,. \tag{6.24}$$

We see that in this intermediate regime, the enhancement is linear with χ', as is also seen in Figure 6.5. This linear enhancement is in contrast to the weak measurement limit, where the enhancement scales as χ'^2. Substituting the above expression into Eq. (6.6) and solving in the limit $\chi' \gg 1$, we get

$$V_X \approx \frac{\mathrm{SNR}^{3/4}}{\sqrt{2\chi'\eta\mu/\gamma}} \,, \tag{6.25}$$

in exact agreement with Eq. (6.15).

6.4 Resolved sideband cooling

Up to this point we have only considered optomechanical systems as ultra-sensitive transducers of position fluctuations. It is natural to ask whether there is any advantage in using a detuned parametric drive in conjunction with the near-ubiquitous optomechanical technique of sideband cooling. The resonant driving case of this has been analysed previously, albeit with a focus on the cavity output spectrum[119].

We can model sideband cooling by extending the master equation to include a cavity bath. This is done by adiabatically eliminating the cavity[83], and results in the back-action terms in equation (3.22) being replaced by terms analogous to those for the thermal bath. The deterministic part of the master equation is then

$$\begin{aligned}\langle \mathrm{d}\langle \hat{A}\rangle\rangle &= -\frac{i}{\hbar}\langle[\hat{A},\tilde{H}]\rangle\,\mathrm{d}t + 2\gamma N\langle\mathcal{D}[\hat{a}^\dagger]\hat{A}\rangle\,\mathrm{d}t + 2\gamma(N+1)\langle\mathcal{D}[\hat{a}]\hat{A}\rangle\,\mathrm{d}t \\ &\quad +2\gamma_C N_C\langle\mathcal{D}[\hat{a}^\dagger]\hat{A}\rangle\,\mathrm{d}t + 2\gamma_C(N_C+1)\langle\mathcal{D}[\hat{a}]\hat{A}\rangle\,\mathrm{d}t\ ,\end{aligned} \tag{6.26}$$

where the general forms of the optical damping γ_C and effective cavity temperature N_C are given in [120] as Γ_{opt} and $\bar{n}_M^O$ respectively. Taking the limit of large cavity loss $\kappa \gg \omega_m$ and zero cavity detuning, the back-action noise $\gamma_C(2N_C+1)$ from the master equation is equal to μ as we have defined in Eq. (3.20) so our approach is consistent with Ref. [120].

On the red sideband (i.e. cavity detuning equal to $-\omega_m$) and in the good cavity limit, the cavity temperature N_C approaches zero and all photons detected are a product of phonon absorption. Consequently, only downgoing transitions appear in the measurement terms of the master equation. In this regime, adiabatic elimination can be performed on the stochastic master equation for the coupled cavity-oscillator system as in Ref. [85]. The resulting stochastic master equation for the oscillator alone is then equivalent to heterodyne detection of a cavity output[87] and has the form

$$\begin{aligned}\mathrm{d}\langle\hat{A}\rangle &= -\frac{i}{\hbar}\langle[\hat{A},\tilde{H}]\rangle\,\mathrm{d}t + [2\gamma N]\langle\mathcal{D}[\hat{a}^\dagger]\hat{A}\rangle\,\mathrm{d}t + [2\gamma(N+1)+\mu]\langle\mathcal{D}[\hat{a}]\hat{A}\rangle\,\mathrm{d}t \\ &\quad +\sqrt{\eta\mu/2}\langle\mathcal{H}[\hat{a}]\hat{A}\rangle\,\mathrm{d}W_1 + \sqrt{\eta\mu/2}\langle\mathcal{H}[i\hat{a}]\hat{A}\rangle\,\mathrm{d}W_2\ .\end{aligned} \tag{6.27}$$

In this case, the Wiener processes are

$$\mathrm{d}W_1 = \mathrm{d}Q_X - \sqrt{\eta\mu}\langle\hat{X}\rangle\mathrm{d}t \tag{6.28}$$

$$\mathrm{d}W_2 = \mathrm{d}Q_Y - \sqrt{\eta\mu}\langle\hat{Y}\rangle\mathrm{d}t\ . \tag{6.29}$$

This master equation leads to variance equations by the same method as in Chapter 3. Letting $\theta = \pi/4$

$$\frac{d}{dt}V_X = -(2\gamma+\mu)(V_X-1/2) - 2(\Delta-\chi)C + 2N\gamma - \eta\mu[(V_X-1/2)^2 + C^2] \tag{6.30}$$

$$\frac{d}{dt}V_Y = -(2\gamma+\mu)(V_Y-1/2) + 2(\Delta+\chi)C + 2N\gamma - \eta\mu[(V_Y-1/2)^2 + C^2] \tag{6.31}$$

$$\frac{d}{dt}C = -(2\gamma+\mu)C - \Delta(V_Y-V_X) + \chi(V_X+V_Y) - \eta\mu C(V_X+V_Y-1)\ . \tag{6.32}$$

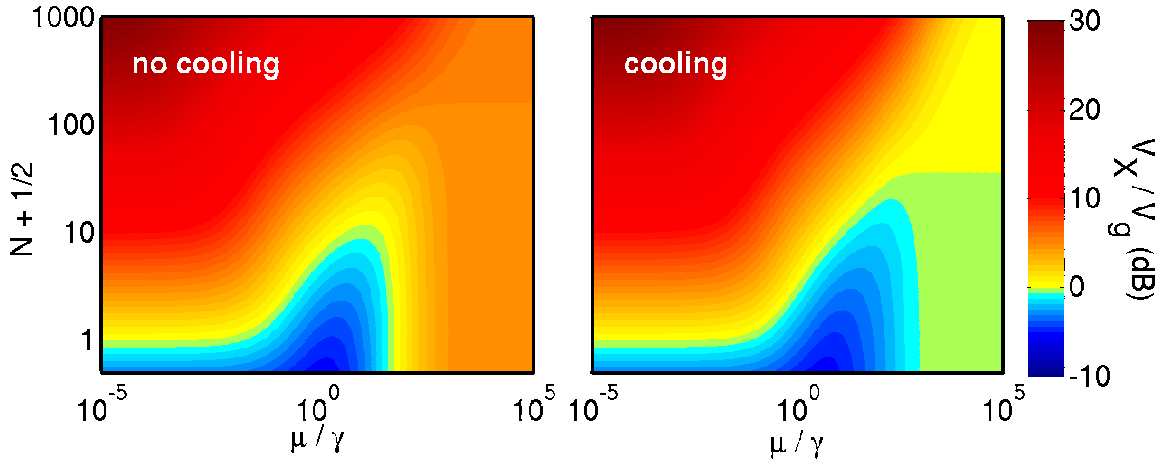

Figure 6.6: Squeezed conditional variance for an inefficient detector ($\eta = 0.1$), normalised to the ground state variance, in the (left) normal and (right) ideal resolved sideband regime. In both cases, $\chi = 100\gamma$ and detuning from threshold is γ.

Compared to the standard continuous measurement derived earlier, the additional terms proportional to μ here are an unconditional linear damping as well as an offset in the conditioning term, such that all measurement terms disappear for a symmetric pure state $V_X = V_Y = 1/2$ with $C = 0$. The threshold condition is now dependent on μ

$$\chi_{th}^{RSB} = \sqrt{(\gamma + \mu/2)^2 + \Delta^2}\,, \tag{6.33}$$

and the unconditional variance with no parametric drive is

$$V_T = \frac{2\gamma}{2\gamma + \mu} N + \frac{1}{2}\,, \tag{6.34}$$

as in [120]. For perfect efficiency, the linear optical damping terms vanish since

$$-\mu(V_X - 1/2) - \mu(V_X - 1/2)^2 = -\mu V_X^2 + \mu/4\,, \tag{6.35}$$

leaving variance equations that are identical to Eqs (4.25-4.27) apart from an expected factor of 4 in measurement strength[39]. However, for $\eta \ll 1$, resolved sideband cooling offers a qualitative difference since a pure state is always approached in the strong measurement limit. Without cooling, this limiting variance increases by a factor of $1/\sqrt{\eta}$.

These differences are small, however, in the important regime around $\mu \approx \gamma$. This is shown in Figure 6.6, using numerical solutions to the steady-state variance equations. With resolved sideband cooling, the squeezing extends further into the back-action dominated region $\mu > \gamma$, however the maximum squeezing is unchanged. Outside the good cavity limit, the cavity bath temperature increases and the result can be expected to be worse. Therefore, while resolved sideband cooling aids in resolving zero-point fluctuations in the presence of detector inefficiency, the requirement of strong measurement precludes it from being significantly useful in the context of parametric squeezing. Sideband cooling is, however, quite compatible with

backaction evasion-based squeezing schemes as they both operate best in the (would-be) backaction dominated regime and can both be implemented using similar techniques[91]. This combination, known as reservoir engineering, is analysed in Ref. [118].

Chapter 7

Mechanical entanglement via detuned parametric amplification

7.1 Introduction

Observing quantum entanglement between massive objects has been a long-standing milestone in exploring the quantum to classical transition[2, 6], constructing hybrid quantum information systems[69, 30, 76] and sensing forces with ultrahigh precision[121]. This goal has prompted interest in the scaling-up of matter-wave interferometers[122, 123], in levitating microparticles[9] and in arrays of mechanical oscillators[44, 124], among other research. Optomechanical systems, in which mechanical oscillators are coupled to optical or microwave fields, are well known as a promising basis for observing macroscopic entanglement in a wide variety of architectures[120, 34].

The advantage of optomechanics lies in the ability to effectively transduce mechanical motion; using backaction evading methods[36], in principle one can achieve precision beyond the level of the quantum zero-point motion[46]. Measurement with sub-zero point precision is only possible for one quadrature of motion, at the expense of degraded sensitivity in the other, due to Heisenberg's uncertainty principle. Such "quantum squeezing" of a quadrature, when applied to collective observables of two or more oscillators, yields quantum entanglement between the oscillators. Recently, the theory of optomechanical back-action evasion, which allows measurement-based squeezing, has been expanded to two-mode systems[114], providing a route to mechanical entanglement. In addition, entanglement can be achieved via dispersive[125, 126, 127] and dissipative[128, 129] interactions with cavity fields, including the use of squeezed and entangled fields[130, 131, 132]. However, while feasible in principle, purely optomechanical entanglement is difficult to achieve in practice due to the requirement of strong and efficient coupling to the optical or microwave field.

In parallel to developments in optomechanics, the fabrication of arrays of electromechanical resonators has developed to an extent that multi-mode coupling can now be precisely

controlled[62, 61]. Theoretical work shows that modulation of these couplings, which reduces fluctuations in certain collective quadratures of motion, is also sufficient for the creation of entanglement[133, 134], thus providing a simple and accessible alternative to purely measurement-based schemes. In this previous work, appreciable entanglement could not be sustained for steady-state operation, as is also the case for resonant parametric squeezing of a single oscillator[135].

In Chapter 6, it was shown that with the aid of weak continuous measurement, detuning a parametric drive from resonance allows strong steady-state squeezing of an oscillator. Here, we show that the same principle can be applied generally to coupled oscillators in at least two feasible scenarios, allowing strong two-mode entanglement. The first scheme involves a modulation of the coupling between the oscillators, while the second combines a constant linear coupling with single-mode parametric drives. Since only weak continuous measurement is required, the oscillators can be monitored individually without spurious back-action noise, thereby avoiding the need for restrictive measurement setups that couple only to the collective variables of interest. Additionally, the inbuilt parametric tunability of the oscillators in our scheme relaxes the engineering requirements for the physical device. Finally, we show that the entanglement generated by our scheme can be achieved with realistic experimental parameters, and compare this to back-action evading methods[114], making use of Duan's inseparability criterion[78].

7.2 Model one: Modulated coupling

Here, we consider a simple detuning of a previously proposed mechanical two-mode squeezing scheme[133] involving a modulated position-position coupling. Consider two oscillators with identical resonance frequency ω_m, which have a controlled time-dependent coupling between them as shown in Figure 7.1(a). If the coupling is sinusoidally modulated about zero at a frequency $2\omega_d$, the Hamiltonian can be written

$$\tilde{H} = \frac{1}{2m}(\tilde{p}_1^2 + \tilde{p}_2^2) + \frac{m\omega_m^2}{2}(\tilde{x}_1^2 + \tilde{x}_2^2) + g\tilde{x}_1\tilde{x}_2\cos(2\omega_d t)\ , \tag{7.1}$$

where the half-modulation frequency $\omega_d = \omega_m - \Delta$. We focus on a modulation frequency near $2\omega_m$, such that $\Delta \ll \omega_m$. The rotating wave approximation is made in a very similar way as in Section 4.3 for a single-mode detuned drive. In this case, the annihilation operators $\tilde{a}$ and $\tilde{b}$

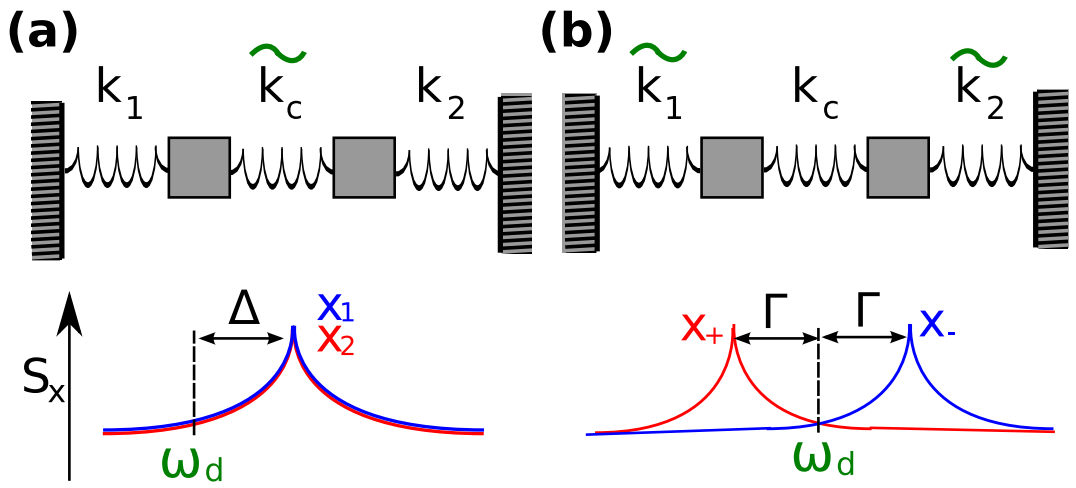

Figure 7.1: Two approaches to achieving entanglement of mechanical oscillators. Each approach is idealised as a coupled mass-on-spring system, with time-dependent modulations at frequency $2\omega_d$ of (a) the intermodal coupling k_c or (b) the spring constants k_1 and k_2. Below are plots of the noise spectra of the mechanical modes in the absence of parametric driving. In (a) the mechanical modes of the two masses are degenerate while in (b) there is normal-mode splitting. In addition, the relation between ω_d and the detuning parameters Δ and Γ are indicated.

satisfy

$$\sqrt{\frac{m_{\rm eff}\omega_m}{\hbar}}\,\tilde{x}_1 = (\tilde{a}+\tilde{a}^\dagger)/\sqrt{2} \tag{7.2a}$$

$$\sqrt{\frac{1}{\hbar m_{\rm eff}\omega_m}}\,\tilde{p}_1 = -i(\tilde{a}-\tilde{a}^\dagger)/\sqrt{2} \tag{7.2b}$$

$$\sqrt{\frac{m_{\rm eff}\omega_m}{\hbar}}\,\tilde{x}_2 = (\tilde{b}+\tilde{b}^\dagger)/\sqrt{2} \tag{7.2c}$$

$$\sqrt{\frac{1}{\hbar m_{\rm eff}\omega_m}}\,\tilde{p}_2 = -i(\tilde{b}-\tilde{b}^\dagger)/\sqrt{2} \tag{7.2d}$$

Using a rotating frame at $\omega_m - \Delta$, the transformed operators $\hat{a}$ and $\hat{b}$ are

$$\hat{a} = \hat{a}e^{-i\omega_d} \tag{7.3}$$

$$\hat{b} = \hat{b}e^{-i\omega_d} \tag{7.4}$$

The interaction Hamiltonian becomes

$$\begin{aligned}\hat{H}_I &= \hbar\Delta(\hat{a}^\dagger\hat{a}+\hat{b}^\dagger\hat{b}+1)+\hbar\chi(\hat{a}\hat{b}+\hat{a}^\dagger\hat{b}^\dagger) \\ &= \frac{\hbar\Delta}{2}(\hat{X}_1^2+\hat{Y}_1^2+\hat{X}_2^2+\hat{Y}_2^2)+\hbar\chi(\hat{X}_1\hat{X}_2-\hat{Y}_1\hat{Y}_2)\,,\end{aligned} \tag{7.5}$$

where $\chi = g/2m\omega_m$ and the single-mode quadrature operators are defined as

$$\hat{X}_1 = (\hat{a}+\hat{a}^\dagger)/\sqrt{2} \tag{7.6a}$$

$$\hat{Y}_1 = -i(\hat{a}-\hat{a}^\dagger)/\sqrt{2} \tag{7.6b}$$

$$\hat{X}_2 = (\hat{b}+\hat{b}^\dagger)/\sqrt{2} \tag{7.6c}$$

$$\hat{Y}_2 = -i(\hat{b}-\hat{b}^\dagger)/\sqrt{2} \tag{7.6d}$$

We can see that the terms proportional to the parameter χ constitute a two-mode squeezing operation, well-known in quantum optics[136]. In the resonant case $\Delta = 0$, this two-mode squeezing results in amplification of two collective quadratures of motion and squeezing of the other two. When the rate of this process exceeds the damping rate of the system (i.e. $\chi > \gamma$), the amplification causes exponential growth of the mechanical oscillations, leading to deleterious mechanical and measurement nonlinearities. Tian et al. overcome this by following the squeezing process with a second modulation to swap the fluctuations between quadratures[133]. Here, we instead consider the steady-state behaviour in the more general case where $\Delta \neq 0$.

We define the quadratures as those of the two natural collective modes $x_+ = (x_1 + x_2)/\sqrt{2}$ and $x_- = (x_1 - x_2)/\sqrt{2}$, namely

$$\hat{X}_+ = (\hat{X}_1 + \hat{X}_2)/\sqrt{2} \tag{7.7a}$$
$$\hat{X}_- = (\hat{X}_1 - \hat{X}_2)/\sqrt{2} \tag{7.7b}$$
$$\hat{Y}_+ = (\hat{Y}_1 + \hat{Y}_2)/\sqrt{2} \tag{7.7c}$$
$$\hat{Y}_- = (\hat{Y}_1 - \hat{Y}_2)/\sqrt{2}\,. \tag{7.7d}$$

The two non-zero commutators between these operators are

$$[\hat{X}_+, \hat{Y}_+] = [\hat{X}_-, \hat{Y}_-] = i\,. \tag{7.8}$$

In these collective variables, the Hamiltonian can be factorised as

$$\tilde{H} = \frac{\hbar(\Delta+\chi)}{2}(\hat{X}_+^2 + \hat{Y}_-^2) + \frac{\hbar(\Delta-\chi)}{2}(\hat{X}_-^2 + \hat{Y}_+^2)\,. \tag{7.9}$$

With equal dissipation for both oscillators at rate γ, the equations of motion are

$$\begin{bmatrix} \mathrm{d}\hat{X}_+ \\ \mathrm{d}\hat{X}_- \\ \mathrm{d}\hat{Y}_+ \\ \mathrm{d}\hat{Y}_- \end{bmatrix} = \begin{bmatrix} -\gamma & 0 & -\chi+\Delta & 0 \\ 0 & -\gamma & 0 & \chi+\Delta \\ -\chi-\Delta & 0 & -\gamma & 0 \\ 0 & \chi-\Delta & 0 & -\gamma \end{bmatrix} \begin{bmatrix} \hat{X}_+ \\ \hat{X}_- \\ \hat{Y}_+ \\ \hat{Y}_- \end{bmatrix} \mathrm{d}t + \sqrt{2\gamma} \begin{bmatrix} \mathrm{d}\hat{X}_{+\mathrm{in}}(t) \\ \mathrm{d}\hat{X}_{-\mathrm{in}}(t) \\ \mathrm{d}\hat{Y}_{+\mathrm{in}}(t) \\ \mathrm{d}\hat{Y}_{-\mathrm{in}}(t) \end{bmatrix}\,. \tag{7.10}$$

It is easy to see that the four collective quadratures can be sorted into their non-commuting pairs, with the two pairs independent of each other

$$\begin{bmatrix} \mathrm{d}\hat{X}_\pm \\ \mathrm{d}\hat{Y}_\pm \end{bmatrix} = \begin{bmatrix} -\gamma & \Delta\mp\chi \\ -\Delta\mp\chi & -\gamma \end{bmatrix} \begin{bmatrix} \hat{X}_\pm \\ \hat{Y}_\pm \end{bmatrix} \mathrm{d}t + \sqrt{2\gamma} \begin{bmatrix} \mathrm{d}\hat{X}_{\pm\mathrm{in}}(t) \\ \mathrm{d}\hat{Y}_{\pm\mathrm{in}}(t) \end{bmatrix} \tag{7.11}$$

It is important to note that the independence of each pair of quadratures requires the two oscillators ω_m to have identical resonance frequencies and damping rates γ. While the resonance frequencies in this scheme can be made equal by using an optical spring[120] or capacitive tuning[25, 60] on individual oscillators, the individual damping rates are more difficult to engineer. Unequal frequencies or damping rates would be expected to degrade entanglement, the analysis of which would require the solution to the full 10-element covariance matrix in the case

of modulated coupling. The constant coupling scheme below is more naturally robust to these experimental imperfections, as will be further discussed in Section 7.7.

The system we have described remains below threshold and therefore convergent as long as $\chi < \chi_{\rm th}$ where $\chi_{\rm th} = \sqrt{\gamma^2 + \Delta^2}$. That is, χ can be made much larger than γ as long as the absolute detuning follows suit.

To see the utility of a large detuning, consider the simple case $\Delta = \pm\chi$. For example, setting $\Delta = \chi$ gives

$$\hat{H}_I = \hbar\chi(\hat{X}_+^2 + \hat{Y}_-^2) \, . \tag{7.12}$$

This Hamiltonian is similar to a quantum non-demolition (QND) measurement in that in the absence of damping, $\hat{X}_+$ and $\hat{Y}_-$ are constants of the motion. This is analogous to the scenario discussed in Section 6.3 for a single continuously measured oscillator, which was shown to correspond to backaction evading measurement. As can be verified from Eq. (7.11), the quasi-QND variables $\hat{X}_+$ and $\hat{Y}_-$ are now only influenced by dissipation. However, a time-dependent signal — such as thermal noise — in $\hat{X}_+$ or $\hat{Y}_-$ will appear in the subsequent evolution of non-QND observables $\hat{Y}_+$ and $\hat{X}_-$, respectively. For values of χ much greater than γ, these signals will appear strongly amplified. Weak measurements of $\hat{Y}_+$ and $\hat{X}_-$ then provide enhanced effective measurements of the quasi-QND observables $\hat{X}_+$ and $\hat{Y}_-$. The result is that one can strongly condition the latter quadratures without the backaction of a strong measurement. The enhanced collective measurement described above also occurs in the general case $|\Delta| \neq \chi$, albeit without the simplified QND dynamics, and is most pronounced at the slightly lower detuning where $\chi \approx \chi_{\rm th}$.

7.3 Collective-mode measurement and entanglement

For ideal continuous variable entanglement, it is necessary for two collective quadratures of the two oscillators to be localised to below the zero-point motion. In principle, two commuting collective quadratures can be measured without backaction, implying that this two-mode squeezing can be achieved by a strong measurement. However, achieving such an ideal non-local measurement is difficult without complex measurement techniques. For example, the variable $\tilde{x}_1 - \tilde{x}_2$ can be measured by using the two oscillators as the end-mirrors of an optomechanical cavity. However, this configuration only yields information about the quadratures $\hat{X}_-$ and $\hat{Y}_-$, which do not commute and hence cannot be squeezed. The measurement of only two commuting collective observables is the task of two-mode backaction evasion[114], which will be discussed later.

Detuned parametric driving provides an alternative solution to this problem by making sub-zero point collective fluctuations accessible to weak measurement. This is possible due to correlations between the squeezed and amplified collective quadratures, with the specific dynamics shown in the previous section. With only weak measurement, the position of each

oscillator can be independently and continuously monitored without significant backaction, eliminating the need for specialised measurement techniques. Instead, collective quadratures can be localised to below the zero point level by conditioning on the classical measurement records. In other words, while a squeezed quadrature (for example X_+) has its own measurement record dominated by measurement noise, an accurate estimate of X_+ can be filtered from the fluctuations of its amplified pair Y_+, which can be well transduced. In this sense, detuned parametric amplification with weak measurement conditioning is an alternative to two-mode backaction evading measurement.

7.4 Conditional variances

The conditional variance quantifies the error in the optimal estimate of an observable when past measurements are taken into account. As in previous chapters, the effects of measurement as well as thermal noise are modelled using a stochastic master equation. Let us assume the two oscillator positions x_1 and x_2 are measured independently. All four collective quadratures will then experience the same rate of back-action and conditioning, quantified by the parameter μ. The master equation is therefore obtained by duplicating the single-mode master equation given by Eq. (3.22). An observable $\hat{A}$ will then evolve as

$$\begin{aligned} \mathrm{d}\langle\hat{A}\rangle &= -\frac{i}{\hbar}\langle[\hat{A},\tilde{H}]\rangle\,\mathrm{d}t + [2\gamma N+\mu]\langle\mathcal{D}[\hat{a}^\dagger+\hat{b}^\dagger]\hat{A}\rangle\,\mathrm{d}t + [2\gamma(N+1)+\mu]\langle\mathcal{D}[\hat{a}+\hat{b}]\hat{A}\rangle\,\mathrm{d}t \\ &\quad +\sqrt{\eta\mu}(\langle\mathcal{H}[\hat{X}_+]\hat{A}\rangle\,\mathrm{d}W_1+\langle\mathcal{H}[\hat{Y}_+]\hat{A}\rangle\,\mathrm{d}W_2+\langle\mathcal{H}[\hat{X}_-]\hat{A}\rangle\,\mathrm{d}W_3+\langle\mathcal{H}[\hat{Y}_-]\hat{A}\rangle\,\mathrm{d}W_4)\,. \end{aligned} \tag{7.13}$$

Here, the Lindblad superoperators for the two oscillators are combined for compactness, which is possible due to linearity. As before, the evolution of the conditional variances is obtained by inserting linear and quadratic observables into the master equation. In the steady state, the only non-zero covariances are those between $\hat{X}_+$ and $\hat{Y}_+$ and between $\hat{X}_-$ and $\hat{Y}_-$. This leaves two independent sets of three equations, written in collated form as

$$\begin{aligned} \frac{\mathrm{d}V_{X\pm}}{\mathrm{d}t} &= -2\gamma V_{X\pm} - 2(\Delta\mp\chi)C_\pm + 2\gamma V_T - 4\eta\mu(V_{X\pm}^2+C_\pm^2) \\ \frac{\mathrm{d}V_{Y\pm}}{\mathrm{d}t} &= -2\gamma V_{Y\pm} + 2(\Delta\pm\chi)C_\pm + 2\gamma V_T - 4\eta\mu(V_{Y\pm}^2+C_\pm^2) \\ \frac{\mathrm{d}C_\pm}{\mathrm{d}t} &= -2\gamma C_\pm \pm \Delta(V_{X\pm}-V_{Y\pm}) \pm \chi(V_{X\pm}+V_{Y\pm}) - 4\eta\mu C_\pm(V_{X\pm}+V_{Y\pm})\,, \end{aligned} \tag{7.14}$$

where as before $V_T = N + 1/2 + \mu/2\gamma$. Remarkably, each of these sets is identical to the three variance equations in the one-mode detuned parametric amplification theory, with steady-state solutions already derived in Chapter 4. This means that the amount of conditional two-mode squeezing generated by a coupling rate modulation of χ is the same as the single mode squeezing available using a spring constant modulation of χ. The maximum squeezing appears at some angle α in the X_+, Y_+ plane, and at 90 degrees to this angle in the X_-, Y_- plane. That is,

$$Q_{\alpha+} = X_+\cos\alpha + Y_+\sin\alpha \tag{7.15}$$

$$Q_{\alpha-} = Y_-\cos\alpha - X_-\sin\alpha \tag{7.16}$$

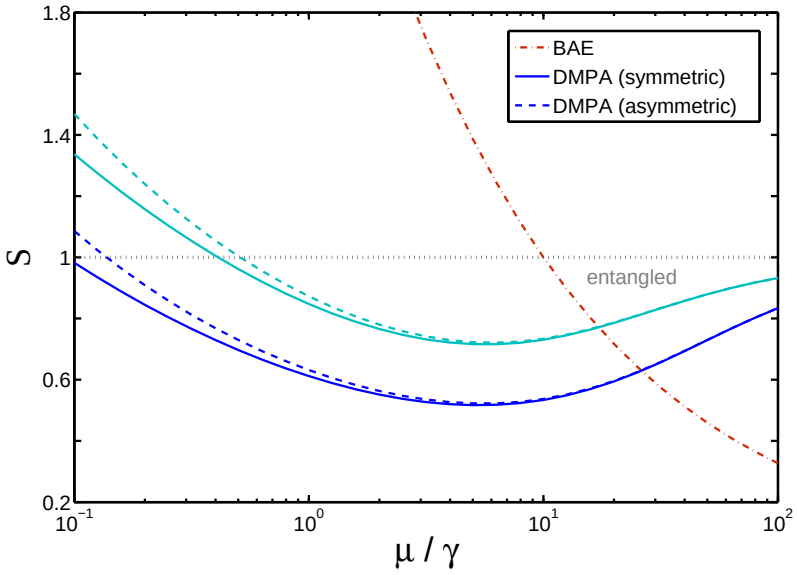

Figure 7.2: Separability S as a function of measurement strength in the case of symmetric damping rates (solid lines); and using the constant-coupling method with a damping asymmetry $\gamma_D = 0.5\gamma_S$ (dashed lines). Light and dark curves indicate normalised drive strengths χ/γ of 25 and 50, respectively, while the mean phonon occupation N is 5 and efficiency η is unity. The dot-dashed curve represents the minimum separability using two-mode backaction evasion.

We will denote the variances of these optimal quadratures as $V_{\alpha+}$ and $V_{\alpha-}$, respectively.

The necessary and sufficient conditions for entanglement of bipartite Gaussian states are discussed in Section 2.4. Here, we quantify the entanglement using the product form for separability

$$S_P = 2\sqrt{V_{\alpha+}V_{\alpha-}}\,, \tag{7.17}$$

In general, a separability S_P below unity as defined above is a sufficient condition for entanglement. This requires the geometric mean of the quadrature variances $V_{\alpha+}$ and $V_{\alpha-}$ to be below the level of the zero-point motion. Inserting the single-mode solution for V_α given by Eq. (4.48), we find

$$S_P = \frac{\sqrt{(\gamma+\chi\sin(2\alpha))^2+4\gamma^2\mathrm{SNR}}-\gamma-\chi\sin(2\alpha)}{2\eta\mu}\,, \tag{7.18}$$

where the signal to noise ratio is given by Eq. (3.33) and the squeezing angle α is given by Eq. (4.51).

Similar to our previous results for single-mode squeezing, entanglement is easily achievable for a low mean phonon occupation N, detuning situated near threshold ($\chi_{th} \approx \chi$) and with a moderate measurement strength, as shown by Figure 7.2. In the strong measurement regime, backaction causes the μ^2 term in SNR to dominate and the entanglement to disappear as expected. With a moderate measurement strength, the parametric drive boosts the effective measurement into this regime without adding backaction. When $\chi \gg \gamma$, the optimal conditioning occurs near $\mu \approx \gamma(N + 1/2)$, with the separability S scaling as $\sqrt{\gamma/\chi}$. In contrast,

backaction evasion can only produce entanglement in the strong and efficient measurement regime $\eta\mu \gg \gamma$, as shown in Figure 7.2.

By combining measurement conditioning and unitary coupling, this scheme hybridises two approaches to entanglement generation. In contrast to purely parametric-based proposals such as Ref. [133], the entanglement can be made arbitrarily strong with the system remaining in the steady-state. Unlike purely measurement-based proposals, independent weak continuous measurements of the two oscillators are sufficient to generate entanglement between them. This can be confirmed by reconstructing the conditional covariance matrix from the measurement record. Entanglement can also be independently verified via direct tomography of the mechanical states, using strong projective measurements on the individual oscillators[137] and analysis of correlations. Even with this verification step, at no stage does a collective mechanical mode need to be measured directly.

7.5 Model two: constant coupling

An equivalent scenario, resulting in the same variance equations, can arise from constant linear coupling between two oscillators, with degenerate parametric drives applied individually to each oscillator on resonance ($\Delta = 0$). In this case, as illustrated by Figure 7.1(b), effective detunings for the collective variables are provided by the normal-mode splitting, which is equal to twice the coupling rate Γ. The Hamiltonian is given by

$$\tilde{H} = \frac{1}{2m}(\tilde{p}_1^2 + \tilde{p}_2^2) + \frac{\Gamma}{m\omega_m}\tilde{x}_1\tilde{x}_2 + \frac{m\omega_m}{2}[\tilde{x}_1^2(\omega_m + 2\chi\sin 2\omega_m t) + \tilde{x}_2^2(\omega_m + 2\chi\sin 2\omega_m t)]$$

Going into a rotating frame at ω_m, assuming $\Gamma \ll \omega_m$

$$\begin{aligned}\hat{H}_I &= \hbar\Gamma(\hat{a}^\dagger\hat{b} + \hat{a}\hat{b}^\dagger) - \frac{i\hbar\chi}{2}(\hat{a}^2 - \hat{a}^{\dagger 2} + \hat{b}^2 - \hat{b}^{\dagger 2}) \\ &= \hbar\Gamma(\hat{X}_1\hat{X}_2 + \hat{Y}_1\hat{Y}_2) + \frac{\hbar\chi}{2}(\hat{X}_1\hat{Y}_1 + \hat{Y}_1\hat{X}_1 + \hat{X}_2\hat{Y}_2 + \hat{Y}_2\hat{X}_2)\end{aligned} \tag{7.19}$$

which factorises as

$$\hat{H}_I = \frac{\hbar(\chi+\Gamma)}{2}(\hat{U}_1\hat{V}_2 + \hat{V}_2\hat{U}_1) + \frac{\hbar(\chi-\Gamma)}{2}(\hat{U}_2\hat{V}_1 + \hat{V}_1\hat{U}_2)\ , \tag{7.20}$$

where the new collective quadratures are defined as

$$\hat{U}_1 = (\hat{X}_1 + \hat{Y}_2)/\sqrt{2} \tag{7.21a}$$

$$\hat{U}_2 = (\hat{X}_1 - \hat{Y}_2)/\sqrt{2} \tag{7.21b}$$

$$\hat{V}_1 = (\hat{Y}_1 - \hat{X}_2)/\sqrt{2} \tag{7.21c}$$

$$\hat{V}_2 = (\hat{Y}_1 + \hat{X}_2)/\sqrt{2}\ . \tag{7.21d}$$

As in the first model, we consider the independent monitoring of both oscillators, allowing these observables to be constructed trivially via lock-in techniques. It should be noted that

the times at which the $\hat{X}$ and $\hat{Y}$ quadratures reflect the true position differ by a quarter of an oscillator cycle. However, in the case of high-Q oscillators such that $Q \gg N$, a quarter-cycle is insufficient time for thermal perturbations to influence the oscillators and therefore can be presumed to have little practical effect on entanglement.

The two non-zero commutators between the four new operators are

$$[\hat{U}_1, \hat{V}_1] = [\hat{U}_2, \hat{V}_2] = i \ , \tag{7.22}$$

so that with damping, the mean evolution of the four quadratures is given by

$$\begin{bmatrix} \mathrm{d}\hat{U}_1 \\ \mathrm{d}\hat{U}_2 \\ \mathrm{d}\hat{V}_1 \\ \mathrm{d}\hat{V}_2 \end{bmatrix} = \begin{bmatrix} -\gamma & \chi-\Gamma & 0 & 0 \\ \chi+\Gamma & -\gamma & 0 & 0 \\ 0 & 0 & -\gamma & -\chi-\Gamma \\ 0 & 0 & -\chi+\Gamma & -\gamma \end{bmatrix} \begin{bmatrix} \hat{U}_1 \\ \hat{U}_2 \\ \hat{V}_1 \\ \hat{V}_2 \end{bmatrix} \mathrm{d}t + \sqrt{2\gamma} \begin{bmatrix} \mathrm{d}\hat{U}_{1\mathrm{in}}(t) \\ \mathrm{d}\hat{U}_{2\mathrm{in}}(t) \\ \mathrm{d}\hat{V}_{1\mathrm{in}}(t) \\ \mathrm{d}\hat{V}_{2\mathrm{in}}(t) \end{bmatrix} . \tag{7.23}$$

This immediately resembles Eq. (7.11) for the case of two-mode squeezing via modulated coupling, but with the detuning Δ replaced by half of the normal-mode splitting Γ. This method is analogous to the generation of two-mode squeezing of light by coupling two single squeezed modes on a beam-splitter[71]. Again choosing the simplified case $\chi = \Gamma$, we find that $\hat{V}_1$ is a proxy observable for $\hat{V}_2$ and $\hat{U}_2$ is a proxy observable for $\hat{U}_1$. The variance equations are likewise identical to those in the modulated coupling case. Notably, unlike the previous method, in this case the dynamical coupling due to the parametric drive is between commuting pairs of observables, that is

$$[U_1, U_2] = [V_1, V_2] = 0 \ . \tag{7.24}$$

Therefore, these pairs of observables both qualify as quantum mechanics-free subsystems, a topic of recent interest[138].

7.6 Comparison with measurement-based scheme

Creating two-mode entanglement using parametric amplification and weak measurement avoids the difficult problem of achieving a strong measurement of the commuting quadratures $\hat{X}_+$ and $\hat{Y}_-$ without also measuring the orthogonal quadratures $\hat{X}_-$ and $\hat{Y}_+$. As described in Section 7.3, any measurement of the latter quadratures would introduce backaction to (and thus prevent squeezing of) the former. Methods to overcome this backaction using measurement alone generally involve a time-dependent modulation of coupling to the transducer. A recent proposal for this kind of cavity optomechanics-based backaction evasion[114] involves using oscillators of differing frequency, such that the quadrature $\hat{Y}_-$ is measured via dynamic coupling with the single transduced collective quadrature $\hat{X}_+$. Although the analysis in that work assumes the good-cavity limit, ideal for one-mode backaction evasion[46], spurious heating still arises when the dynamic coupling is too slow. That is, the frequency difference $\Omega = (\omega_b - \omega_a)/2$ must be much larger than the mechanical decay rate for both quadratures to be measured efficiently.

The methods we have outlined here, by contrast, allow strong transduction of two commuting collective quadratures below the level of the zero-point motion, with no extra spurious heating arising from the degeneracy of the oscillators. Instead, the backaction heating is a decreasing function of the parametric drive strength. While in principle Ω/γ can be made very large in the measurement-based scheme by using different sized oscillators, in practice this would lead to asymmetries in the damping and measurement rates and hence further experimental difficulties. In allowing the use of similar oscillators, a parametric amplification scheme for mechanical entanglement offers a significant experimental advantage. In addition, while asymmetry in the measurement coupling must be compensated for in two-mode backaction evasion[114], both of the above methods can be used in the weak measurement regime where unequal backaction noise is less critical. Furthermore, the above methods can be used outside the good-cavity regime of optomechanics, whereas this regime is necessary for two-mode backaction evasion.

7.7 Damping asymmetry

To this point the two methods proposed here differ only in experimental implementation. The constant coupling method has the advantage that the ability to tune the individual resonance frequencies is already assumed, and can be achieved by a constant offset of the parametric drive. A more important distinction of the constant coupling method, however, is that it is also robust to unequal damping rates for the two oscillators, a common experimental scenario that cannot otherwise be easily corrected. While the two-mode squeezing method requires equal damping rates $\gamma_1 = \gamma_2 = \gamma$ to keep the two pairs of quadratures independent of each other, this is not required for the constant coupling method. Instead, the damping asymmetry modifies only the effective parametric drive rate. This can be shown by the more general form of Eq. (7.23)

$$\begin{bmatrix} \mathrm{d}\hat{U}_1 \\ \mathrm{d}\hat{U}_2 \\ \mathrm{d}\hat{V}_1 \\ \mathrm{d}\hat{V}_2 \end{bmatrix} = \begin{bmatrix} -\gamma & \chi_1-\Gamma & 0 & 0 \\ \chi_1+\Gamma & -\gamma & 0 & 0 \\ 0 & 0 & -\gamma & -\chi_2-\Gamma \\ 0 & 0 & -\chi_2+\Gamma & -\gamma \end{bmatrix} \begin{bmatrix} \hat{U}_1 \\ \hat{U}_2 \\ \hat{V}_1 \\ \hat{V}_2 \end{bmatrix} \mathrm{d}t + \sqrt{2\gamma} \begin{bmatrix} \mathrm{d}\hat{U}_{1\mathrm{in}}(t) \\ \mathrm{d}\hat{U}_{2\mathrm{in}}(t) \\ \mathrm{d}\hat{V}_{1\mathrm{in}}(t) \\ \mathrm{d}\hat{V}_{2\mathrm{in}}(t) \end{bmatrix}, \tag{7.25}$$

where

$$\chi_1 = \chi - (\gamma_1 - \gamma_2)/2 \tag{7.26}$$

$$\chi_2 = \chi + (\gamma_1 - \gamma_2)/2 \tag{7.27}$$

$$\gamma = (\gamma_1 + \gamma_2)/2\,. \tag{7.28}$$

Therefore, an increased effective rate χ_2 drives the squeezing in one pair of quadratures, while in the other pair the rate is decreased to χ_1. At first glance this would appear to have little effect on the separability, since to first order the loss of squeezing in $\hat{U}_1$ would be made up for

by increased squeezing in $\hat{V}_2$. However, the fact that all quadratures share an effective detuning rate Γ implies that when $\hat{V}_1, \hat{V}_2$ are at the instability threshold (i.e. optimally squeezed), the pair $\hat{U}_1, \hat{U}_2$ are bound to be further away from it due to a weaker effective parametric drive. For a strong parametric drive, this asymmetry has a modest effect, as shown for a 50% difference in damping rates in Figure 7.2.

7.8 Experimental outlook and conclusion

We have provided two routes to robust mechanical entanglement, neither of which rely on being in the deeply backaction-dominated regime, being in the optomechanical good-cavity limit, or on temporally modulated measurement coupling. Instead, by using simple parametric processes to create amplified proxy observables, weak or inefficient measurement is sufficient to strongly condition collective quadratures, thus avoiding the need for collective backaction evading measurements. Methods to continually alternate the sign of intermodal coupling between oscillators, as required by the modulated coupling scheme, have been outlined for electronic resonators[133], but are difficult to extend to multiple mechanical modes. In contrast, the key technique required for the constant-coupling method (single-mode parametric amplification) is well developed in micromechanical and nanomechanical systems[25, 60, 24]. In such devices, intrinsic intermodal coupling through the substrate is substantial, fulfilling the second requirement of this scheme. An example of such a device, recently demonstrated by Okamoto et al.[61], has an intrinsic coupling rate Γ exceeding the damping rate by a factor of around 400, while the piezoelectric strain is sufficient to parametrically drive well above threshold by at least a factor of 100. For such devices to achieve quantum entanglement using the constant coupling method would require significant improvements in measurement sensitivity, as well as increased mode frequency to reduce the mean phonon occupation. The recent experimental work by Bochmann et al.[31], in which a high-frequency mechanical resonator has both piezoelectric and optomechanical coupling, appears to be very promising in this respect. By extending such technology to multiple oscillators, steady-state entanglement of massive objects could be well within reach.

Chapter 8

Quantum state tomography with continuous measurement

8.1 Introduction

So far, this thesis has focused on creating quantum mechanical states of mechanical resonators. A complementary goal is the verification of these states. Often, these two goals are satisfied at the same time. For example, in the case of the steady-state protocols described earlier, measurement both creates and verifies the statistics of the squeezed Gaussian states. However, for more complex quantum states, measurement is not involved and can indeed be detrimental. For example, it is well known that a superposition of two distinct quantum states is destroyed by a measurement that can distinguish between them. Similarly, an energy eigenstate is incompatible with position measurement. This limitation is significant for mechanical oscillators, since it is very difficult to sensitively measure observables other than position. In such cases, verification of the characteristics of the state generally involves a methodical measurement process known as tomography.

Quantum state tomography is vital in experimental settings, even if the state was created by a trusted party. In the same way that one test-drives a car in various likely conditions to make sure it has been manufactured correctly for its purpose, tomography is a test-drive in the relevant phase-space of the prepared quantum state. For a harmonic oscillator, as in optics, this is the quadrature phase space introduced in Chapter 2.

The Wigner function describes a quasi-probability distribution over the quadrature phase space. This two-dimensional distribution is put together from one-dimensional distributions (known as marginals) in the same way that a 3D scan of the brain is put together from multiple 2D scans. Unlike a regular probability distribution, the Wigner function can display negativity as a signature of nonclassicality. As a rule of thumb, negativity is restricted to regions smaller than the ground-state variance (that is, $\sigma_X\sigma_Y$ for the state $|0\rangle$). Therefore, features in the 1D marginals that are smaller than the width of the ground-state must be able to be resolved in

order to reproduce Wigner negativity.

In quantum optics, homodyne measurement is a standard and effective tool for performing tomography on light in a cavity[139]. This is done by repeatedly preparing the state and measuring one field quadrature to build up a marginal distribution. This is repeated for many quadratures and common inverse transforms are used to reproduce a Wigner function[140, 141]. This is a difficult problem, since noise and experimental imperfections lead to discrepancies between the prepared and reconstructed states. Specifically, added noise decreases the resolution of the marginals, making it more difficult to verify that a nonclassical state existed. Various estimation techniques exist to optimise the reconstruction in these cases[141].

Even with the prospect of nonclassical mechanical states becoming within reach, the problem of verification of these states has received little attention. One recent paper proposes the use of strong optical pulses with certain timings to build up quadrature statistics[137], a method akin to backaction evasion. Another couples the resonator to an atom as an ancilla quantum system[142]. Numerous other methods are possible, as evidenced by the numerous proposals for measuring the motional states of trapped ions[143].

In keeping with the spirit of the thesis, this chapter will investigate the potential of resonant parametric amplification and weak continuous measurement for mechanical tomography of an independently prepared state. Since parametric modulation provides noiseless amplification of one quadrature, one would expect this to be well suited to tomographic reconstruction. The challenge here is to accurately model the state's evolution during this process, and to optimally use the measurement to predict the initial state. This idea is akin to a recent tomography proposal for trapped nanoparticles, where the dynamics are modified to make the evolution highly dependent on the initial state[144].

In order to perform this analysis, the theory of linear quantum trajectories developed in quantum optics[145] will be applied to a continuous position measurement. Instead of the master equation approach used in previous chapters, this approach involves the use of a linear stochastic Schrödinger equation (SSE). The SSE equivalent of the master equation used in previous chapters is discussed in Section 8.3, and the evolution of a coherent state is derived in Section 8.4.

Due to the linearity of the SSE, this method enables an extension to non-Gaussian states as superpositions of coherent states. As shown in Section 8.5, all results for coherent states apply to arbitrary quantum states. Such states are most naturally represented by a phase-space distribution known as a Q-function. The effect of the thermal and measurement noise is to limit the resolution of this Q-function.

Similarly to previous chapters, the expected coherent-state evolution is used in Section 8.6 to derive a filter function for the measurement and an associated variance to represent the estimate error. Unlike previous chapters, this estimate refers to the state at the beginning of measurement, rather than the present time. This filter can then be used to reconstruct a phase-space distribution for the initial state, with a resolution given in terms of the estimate

error.

While backaction limits the accuracy of a continuous measurement and precludes nonclassical state verification on its own, above-threshold parametric pre-amplification can easily bring the resolution to the level required for quantum state tomography. Initial analytic derivations provide an upper bound on the estimate error in this case, supported by numerical simulations. It is shown that for a strong enough drive, the coherent amplification of the initial position overcomes the subsequent thermal and zero-point noise entering the oscillator.

8.2 Linear quantum trajectories

The stochastic master equation introduced in Chapter 3 describes the evolution of the ensemble of states that makes up the density matrix. The stochastic part of the equation models the noise inherent to the measurement of the system, while the deterministic part describes the average effect of the unobserved processes such as thermal noise. For Gaussian states, only the evolution of the means and variances are required, which can be calculated easily from a density matrix representation. For non-Gaussian states, the full basis of quantum states must be used, making both numerical and analytic calculations more difficult.

The evolution of an open quantum system can be equivalently modelled by a stochastic Schrödinger equation. Like the conventional Schrödinger equation, a SSE provides the evolution of a pure quantum state, as opposed to a density matrix. Unlike the conventional Schrödinger equation, the evolution is not deterministic and includes random processes to model coupling to the environment. Each instance of these processes is known as a trajectory. This approach was initially developed to speed up numerical calculations[146], but is also useful to obtain insight into quantum behaviour at the fundamental level[87, 147].

Here, I will use a linear form of the SSE to derive the evolution of a coherent mechanical state under the influence of continuous measurement and dissipation. The error in the best estimate of an initial state given the measurement record is derived. Since we are using coherent states and a linear equation, this can be generalised to arbitrary initial states.

8.3 The stochastic Schrödinger equation

We consider an oscillator in the rotating frame at its resonance frequency, with a generalised position measurement of rate μ and coupled with rate γ to a thermal bath as in Section 3. We will assume perfect efficiency for the sake of simplicity.[1] The stochastic influences of the bath can be separated into one zero-point noise process $\xi(t)$ and one thermal noise process $\zeta(t)$, both being complex. The measurement records are given by $W_1(t)$ and $W_2(t)$ for the $\hat{X}$ and $\hat{Y}$

[1]Inefficiency can be modelled as an addition to the thermal phonon occupation. Letting the effective measurement rate equal $\mu = \eta\mu_0$ then $N_{\mathrm{meas}} = (1-\eta)\mu_0/2\gamma$.

quadratures, respectively. All of these are Wiener processes, subject to the Ito rules

$$\begin{aligned} \mathrm{d}\zeta^*\mathrm{d}\zeta &= N\mathrm{d}t & (8.1)\\ \mathrm{d}\xi^*\mathrm{d}\xi &= \mathrm{d}t & (8.2)\\ (\mathrm{d}W_1)^2 &= \mathrm{d}t & (8.3)\\ (\mathrm{d}W_2)^2 &= \mathrm{d}t & (8.4) \end{aligned}$$

Note that $\mathrm{d}\zeta(t)$ is not a unit white noise, but is scaled by the temperature. The linear SSE can be written as

$$\begin{aligned} |\psi(t+\mathrm{d}t)\rangle &= [1-\frac{i}{\hbar}H\,\mathrm{d}t+\sqrt{2\gamma}a\,\mathrm{d}\xi(t)+\sqrt{2\gamma}(a^\dagger\mathrm{d}\zeta-a\,\mathrm{d}\zeta^*)+\sqrt{\mu}(\hat{X}\,\mathrm{d}W_1+\hat{Y}\,\mathrm{d}W_2)\\ &\quad -\gamma a^\dagger a\,\mathrm{d}t-N\gamma(a^\dagger a+aa^\dagger)\,\mathrm{d}t-\frac{\mu}{2}(\hat{X}^2+\hat{Y}^2)\mathrm{d}t]|\psi(t)\rangle \qquad (8.5) \end{aligned}$$

The zero-point noise operator is purely dissipative, and is modelled in the same way as heterodyne measurement[145]. The thermal noise operator takes the form of an infinitesimal random displacement[148]. Finally, the measurement operators follow the generalisation of linear trajectories by Jacobs and Knight[147]. Combining $\mathrm{d}W_1$ and $\mathrm{d}W_2$ as

$$\mathrm{d}Z=(\mathrm{d}W_1+i\mathrm{d}W_2)/\sqrt{2} \qquad (8.6)$$

we can see that the stochastic measurement terms can be written $\hat{a}^\dagger\,\mathrm{d}Z+\hat{a}\,\mathrm{d}Z^*$, which differs from the thermal noise by a change in sign.

Rewriting Eq. (8.5) as

$$|\psi(t+\mathrm{d}t)\rangle=[1+\hat{\theta}(t)]|\psi(t)\rangle \qquad (8.7)$$

the density matrix evolves as

$$\mathrm{d}\rho(t)=[1+\hat{\theta}(t)]\rho(t)[1+\hat{\theta}^\dagger(t)]-\rho(t)=\hat{\theta}(t)\rho+\rho\hat{\theta}^\dagger(t)+\hat{\theta}(t)\rho\hat{\theta}^\dagger(t) \qquad (8.8)$$

Evaluating the right hand side, applying the Ito rules and throwing away the "lost" terms proportional to $\mathrm{d}\xi$ and $\mathrm{d}\zeta$ gives the stochastic master equation. It is easy to check that this exactly reproduces Eq. (3.22), the master equation used in previous chapters, except for the mean values $\langle\hat{X}\rangle$ and $\langle\hat{Y}\rangle$ in the latter, which would require a nonlinear SSE. The consequence of this absence is that the state does not remain normalised during its evolution, and that the norm $\langle\psi(t)|\psi(t)\rangle$ is therefore trajectory-dependent. One consequence of this is that expectation values for a particular trajectory must be normalised by $\langle\psi(t)|\psi(t)\rangle$. A second consequence is that the norm must be used to detemine the probability of this trajectory. The advantage of this approach, however, is that the evolution of a given state (for example, a coherent state) will also apply to an arbitrary superposition of coherent states, due to the linearity of Eq. (8.5).

8.4 Coherent state evolution

Since we are in the rotating frame with no deterministic unitary evolution, we can set $\hat{H}=0$. Now, if we assume an initial coherent state $|\psi(0)\rangle=|\alpha(0)\rangle$, this will remain coherent for all

times due to only first-order terms in $a^\dagger$ in Eq. (8.5).[2] To show this, we can factorise Eq. (8.5), making use of the displacement operator

$$\mathrm{D}[g]|\alpha\rangle = \exp[ga^\dagger - g^*a]|\alpha\rangle = \exp[(g\alpha^* - g^*\alpha)/2]|\alpha + g\rangle \tag{8.9}$$

This factorisation takes the form

$$|\psi(t+\mathrm{d}t)\rangle = \mathrm{D}[\sqrt{2\gamma}\mathrm{d}\zeta]\,\mathrm{D}[\sqrt{\mu}\mathrm{d}Z]\exp[2\sqrt{\mu}a\mathrm{d}Z^*]\exp[\sqrt{2\gamma}a\mathrm{d}\xi]\exp[-(\gamma+2\mu)a^\dagger a\mathrm{d}t]|\psi(t)\rangle \tag{8.10}$$

which can be easily checked by Taylor expanding all terms to second order and using the Ito rules for the complex increments. Now let

$$|\psi(t)\rangle = e^{f(t)}|\alpha(t)\rangle \tag{8.11}$$

such that the norm of the state can be written

$$\langle\psi(t)|\psi(t)\rangle = e^{f(t)+f^*(t)} \tag{8.12}$$

Performing the operations in Eq. (8.10) will allow the time-evolution of $f(t)$ and $\alpha(t)$ to be found. Since the state remains coherent, this means

$$|\psi(t+\mathrm{d}t)\rangle = e^{f(t)+\mathrm{d}f(t)}|\alpha(t)+\mathrm{d}\alpha(t)\rangle \tag{8.13}$$

The increments $\mathrm{d}f$ and $\mathrm{d}\alpha$ can be found by substituting the state $|\alpha\rangle$ into Eq. (8.10) and evaluating one exponential operator at a time. The rightmost operator has the effect

$$\exp[-\Gamma a^\dagger a\,\mathrm{d}t]|\alpha\rangle = \exp[-\Gamma|\alpha|^2\,\mathrm{d}t]|\alpha(1-\Gamma\,\mathrm{d}t)\rangle \tag{8.14}$$

and the next two terms simply use the coherent state property $a|\alpha\rangle = \alpha|\alpha\rangle$. These are finally followed by the displacement operators, leaving

$$\mathrm{d}\alpha(t) = -(\gamma+2\mu)\alpha(t)\,\mathrm{d}t + \sqrt{2\gamma}\mathrm{d}\zeta + \sqrt{\mu}\mathrm{d}Z \tag{8.15}$$

$$\mathrm{d}f(t) = -(\gamma+2\mu)|\alpha(t)|^2\mathrm{d}t + \sqrt{2\gamma}\left[\alpha(t)\mathrm{d}\xi + \frac{1}{2}(\alpha^*(t)\mathrm{d}\zeta - \alpha(t)\mathrm{d}\zeta^*)\right] + \frac{\sqrt{\mu}}{2}(3\alpha(t)\mathrm{d}Z^* + \alpha^*(t)\mathrm{d}Z) \tag{8.16}$$

Note that the thermal noise $\zeta(t)$ only directly contributes to the imaginary part of $f(t)$, adding noise to the overall phase of the state. The coherent displacement $\alpha(t)$ follows a zero-mean Ornstein-Uhlenbeck process, with the solution

$$\alpha(t) = \left[\alpha_0 + \sqrt{\mu}\int_0^t e^{\Gamma_0\tau}\mathrm{d}Z(\tau) + \sqrt{2\gamma}\int_0^t e^{\Gamma_0\tau}\mathrm{d}\zeta(\tau)\right]e^{-\Gamma_0 t} \tag{8.17}$$

$$= [\alpha_0 + \alpha_1(Z,t) + \alpha_2(\zeta,t)]e^{-\Gamma_0 t} \tag{8.18}$$

so the coherent state amplitude exhibits the statistics of 2D Brownian motion, as expected. The damping rate $\Gamma_0 = \gamma + 2\mu$ notably includes the measurement strength.

[2] This analysis can also be performed with $a^{\dagger 2}$ terms — such as from squeezing Hamiltonians — following the method of Goetsch and Graham[149].

8.5 Optimal estimation of an initial state

Above, the evolution of the coherent state displacement $\alpha(t)$ of a mechanical oscillator is given as a function of its environmental stochastic influences, as well as the evolution of the state's prefactor $\exp[f(t)]$ based on these same processes and the displacement. Of these noisy processes, however, only that representing the measurement $Z(t)$ is known. This is in contrast to an optical cavity where, if the outgoing light is detected with perfect efficiency, a quantum-limited estimate of the initial state can be produced by waiting for all of the light to leave the cavity[145]. In terms of our parameters, this situation would be equivalent to $\mu \gg \gamma(2N+1)$.

Ultimately, we would like to find the likelihood of a proposed initial state $|\psi(0)\rangle$, in the presence of unknown stochastic processes $\xi(t), \zeta(t)$, given a measurement record $Z(t)$. This can be expressed in terms of Bayesian probability as

$$\begin{aligned} P(\psi(0)|Z) &= \frac{P(Z|\psi(0))P(\psi(0))}{P(Z)} && (8.19)\\ &= \frac{P(\psi(0))}{P(Z)}\mathrm{E}_{\xi,\zeta}\left[\langle\psi(t)|\psi(t)\rangle\right] && (8.20)\\ &= \frac{P(\psi(0))}{P(Z)}\mathrm{E}_{\xi,\zeta}\left[\exp(f(\xi,\zeta,Z)+f^*(\xi,\zeta,Z))\right] && (8.21)\end{aligned}$$

where the expectation is over all unravellings of ξ and ζ[150].

At first, we will only assume that $|\psi(0)\rangle$ is a coherent state. The normalisation above is then simply the integral over all coherent states, so that

$$P(\alpha(0)|Z) = \frac{\mathrm{E}_{\xi,\zeta}[\langle\psi(t)|\psi(t)\rangle]}{\int \mathrm{E}_{\xi}[\langle\psi(t)|\psi(t)\rangle]\,\mathrm{d}^2\alpha_0} \tag{8.22}$$

Given that we know the evolution of $f(t)$ given an initial coherent state, the above probability can be calculated by performing a simple integral. A Gaussian distribution is expected, with a width depending in some way on μ, γ and N and time. This will be derived in the next section.

8.5.1 Q-function

An arbitrary density matrix can be represented in the coherent state basis by a Q-function.

$$Q(\alpha,\rho) = \frac{1}{\pi}\langle\alpha|\rho|\alpha\rangle \tag{8.23}$$

which is non-negative and equivalent to a Gaussian-convolved Wigner function[3]. Given an initial coherent state

$$\rho_0 = |\alpha_0\rangle\langle\alpha_0| \tag{8.24}$$

the Q-function is

$$\begin{aligned} Q(\alpha,\rho_0) &= \frac{1}{\pi}|\langle\alpha|\alpha_0\rangle|^2 && (8.25)\\ &= \frac{1}{\pi}\exp(-|\alpha-\alpha_0|^2) && (8.26)\end{aligned}$$

[3]In principle, a Q-function can be deconvolved back into a Wigner function[141]

which is a Gaussian distribution of variance 1/2 about α_0.

Preparing this initial state and letting the system evolve for some time t, the entire measurement record Z until time t can be turned into an estimate $\alpha_{\rm est}(Z)$ of α_0. By repeating this measurement, a probabability distribution can be built up. This Gaussian distribution would resemble the Q-function above, but due to the imperfect measurement, would have an increased variance, which we will call $\sigma^2(t)$. We can represent this "smearing" of the distribution by a convolution of the initial Q-function

$$P(\alpha_0|Z(t)) = \frac{1}{\pi\sigma_C^2}\iint \mathrm{d}^2\alpha' \exp\left(\frac{-|\alpha' - \alpha_{\rm est}(Z)|^2}{2\sigma_C^2(t)}\right)|\langle\alpha_0|\alpha'\rangle|^2 \tag{8.27}$$

$$= \frac{1}{2\pi\sigma^2}\exp\left(\frac{-|\alpha_0 - \alpha_{\rm est}(Z)|^2}{2\sigma^2(t)}\right) \tag{8.28}$$

Since the convolution adds the variance of the Q-function, it is easy to show that that the variance of the convolution function is

$$\sigma_C^2(t) = \sigma^2(t) - 1/2 \tag{8.29}$$

That is, the convolution applied to the initial Q-function approaches a delta function in the limit of a perfect measurement where $\sigma^2 = 1/2$.

8.5.2 POVM element

By making use of a probability operator-valued measure (POVM), we can show that the process of estimating an initial coherent state also applies to a general Q-function, and results in a similar convolution to that in Eq. (8.27). Let us assume again an initial coherent state

$$\rho_0 = |\alpha_0\rangle\langle\alpha_0| \tag{8.30}$$

Along with an estimate $\alpha_{\rm est}(Z)$, the measurement record can also be used to reconstruct the corresponding POVM element $\hat{W}(Z)$. This operator defines the effect of the measurement and noise processes, such that its expectation value gives the probability of the time-series $Z(t)$ occuring for an initial state $|\alpha_0\rangle$

$$P(\alpha_{\rm est}(Z)|\alpha_0) = \mathrm{Tr}[\hat{W}(Z)\rho_0] \tag{8.31}$$

$$= \mathrm{Tr}[\hat{W}(Z)|\alpha_0\rangle\langle\alpha_0|] \tag{8.32}$$

$$= \langle\alpha_0|\hat{W}(Z)|\alpha_0\rangle \tag{8.33}$$

By Bayes' theorem, this function should be equivalent to the Gaussian distribution in the right hand side of Eq. (8.28), to within a constant factor. It is easily shown that by defining $\hat{W}$ as

$$\hat{W} = \frac{1}{2\pi\sigma^2}\exp[-(a^\dagger - \alpha_{\rm est}^*)(a - \alpha_{\rm est})/2\sigma^2] \tag{8.34}$$

then Taylor expanding and putting in normal order, the resulting distribution is

$$P(\alpha_{\rm est}(Z)|\alpha_0) = \langle\alpha_0|\hat{W}|\alpha_0\rangle = \frac{1}{2\pi\sigma^2}\exp\left(\frac{-|\alpha_0 - \alpha_{\rm est}|^2}{2\sigma^2}\right) \tag{8.35}$$

which agrees with Eq. (8.28) as intended. Therefore, the overall influence of the stochastic operators over time on the probability distribution, conditional on the measurement record $Z(t)$, can be uniquely represented by the operator $\hat{W}$.

8.5.3 Generalisation to an arbitrary initial state

Due to the fact that we are using a linear SSE, the POVM operator $\hat{W}$ can be applied to an arbitrary pure initial state $|\psi(0)\rangle$. Let this be a sum of coherent states

$$|\psi(0)\rangle = \sum_i c_i |\alpha_i\rangle \tag{8.36}$$

where each c_i is a complex number, so after some time

$$|\psi(t)\rangle = \sum_i c_i e^{f_i(t)} |\alpha_i(t)\rangle \tag{8.37}$$

where each α_i and f_i evolve together according to the solution of the SSE.

The idea that $\hat{W}$ as defined in Eq. (8.34) can be applied to an arbitrary state can be directly validated by a consistency check. Applying the Born rule, and again using the normally ordered Taylor expansion of $\hat{W}$, we get

$$\begin{aligned} P(\alpha_{\text{est}}(Z)|\psi(0)) &= \langle\psi(0)|\hat{W}|\psi(0)\rangle & (8.38)\\ &= \frac{1}{2\pi\sigma^2}\sum_{i,j} c_i^* c_j \langle\alpha_i|\exp[-(a^\dagger - \alpha_{\text{est}}^*)(a-\alpha_{\text{est}})/2\sigma^2]|\alpha_j\rangle & (8.39)\\ &= \frac{1}{2\pi\sigma^2}\sum_{i,j} c_i^* c_j \langle\alpha_i|\alpha_j\rangle \exp\left[\frac{(\alpha_i^* - \alpha_{\text{est}}^*)(\alpha_j - \alpha_{\text{est}})}{2\sigma^2}\right] & (8.40) \end{aligned}$$

While this expression is complicated, we can show that applying the convolution in (8.27) to a general initial Q-function results in the same distribution. Beginning with the conjecture

$$\begin{aligned} P(\psi(0)|Z(t)) &= \frac{1}{2\sigma_C^2}\iint \mathrm{d}^2\alpha' \exp\left(\frac{-|\alpha' - \alpha_{\text{est}}(Z)|^2}{2\sigma_C^2(t)}\right) Q(\alpha', |\psi(0)\rangle\langle\psi(0)|) & (8.41)\\ &= \frac{1}{2\pi\sigma_C^2}\iint \mathrm{d}^2\alpha' \exp\left(\frac{-|\alpha' - \alpha_{\text{est}}(Z)|^2}{2\sigma_C^2(t)}\right) |\langle\psi(0)|\alpha'\rangle|^2 & (8.42) \end{aligned}$$

Expanding out the square of the inner product $|\langle\psi(0)|\alpha'\rangle|^2$ and using the relation

$$\langle\alpha_i|\alpha'\rangle\langle\alpha'|\alpha_j\rangle = \langle\alpha_i|\alpha_j\rangle \exp[-(\alpha' - \alpha_j)(\alpha'^* - \alpha_i^*)] \tag{8.43}$$

we get

$$\begin{aligned} P(\psi(0)|Z(t)) &= \frac{1}{2\pi\sigma_C^2}\iint \mathrm{d}^2\alpha' \exp\left(\frac{-|\alpha' - \alpha_{\text{est}}(Z)|^2}{2\sigma_C^2(t)}\right) \sum_{i,j} c_i^* c_j \langle\alpha_i|\alpha'\rangle\langle\alpha'|\alpha_j\rangle & (8.44)\\ &= \frac{1}{2\pi\sigma_C^2}\sum_{i,j} c_i^* c_j \langle\alpha_i|\alpha_j\rangle \iint \mathrm{d}^2\alpha' \exp\left(\frac{-|\alpha' - \alpha_{\text{est}}(Z)|^2}{2\sigma_C^2(t)}\right) \exp[-(\alpha' - \alpha_j)(\alpha'^* - \alpha_i^*)] \end{aligned}$$

Separating out each α in the integral into real and imaginary parts, and using the formula for a Fourier-transformed Gaussian

$$\int_{-\infty}^{\infty} \exp\left(\frac{-(x-\mu)^2}{2\sigma^2}\right) \exp(itx) = \exp(i\mu t - \sigma^2 t^2/2) \tag{8.45}$$

we obtain Eq. (8.40), thus confirming the conjecture.

In summary, there exists a filter to produce an optimal estimate α_{est} of an initial displacement α_0 using the measurement record Z. This filter can also be used for an arbitrary superposition of coherent states to populate a phase-space distribution over many trials. The resulting distribution will be the original Q-function of the state convolved with a Gaussian of width σ_C.

8.6 Optimal estimate and variance

The task now is to find the parameters in the POVM element given by $\sigma(t)$ and $\alpha_{\text{est}}(Z)$. The first of these is influenced by the amount of lost information, while the second should depend also on the system dynamics. Recalling Eq. (8.16) for an initial coherent state

$$\begin{aligned} \langle\psi(t)|\psi(t)\rangle &= \exp(2\text{Re}[f(\alpha(0),\xi,Z)]) &(8.46)\\ &= \exp\left(\int_0^t -2\Gamma_0|\alpha(\tau,Z)|^2 + 4\sqrt{\mu}\text{Re}[\alpha(\tau)\text{d}Z^*(\tau)] + 2\sqrt{2\gamma}\text{Re}[\alpha(\tau)\text{d}\xi(\tau)]\right) &(8.47)\end{aligned}$$

Interestingly, this exponential can be expressed as the result of a geometric Brownian motion

$$\text{d}\langle\psi(t)|\psi(t)\rangle = \left(4\sqrt{\mu}\text{Re}[\alpha(t)\text{d}Z^*(t)] + 2\sqrt{2\gamma}\text{Re}[\alpha(t)\text{d}\xi(t)]\right)\langle\psi(t)|\psi(t)\rangle \tag{8.48}$$

It can be seen above that the norm is influenced by the zero-point noise $\xi(t)$ as well as indirectly by the thermal noise $\zeta(t)$ via the coherent state displacement $\alpha(t)$. Since the displacement is not affected by the zero-point noise, the expectation over ξ can be written

$$\begin{aligned} \text{E}_\xi[\langle\psi(t)|\psi(t)\rangle] &= \exp\left(\int_0^t -2\Gamma_0|\alpha(\tau,Z)|^2 + 4\sqrt{\mu}\text{Re}[\alpha(\tau)\text{d}Z^*(\tau)]\right)\\ &\quad\times\text{E}_\xi\left[\exp\left(\sqrt{2\gamma}\int_0^t 2\text{Re}[\alpha(\tau)\text{d}\xi(\tau)]\right)\right] &(8.49)\end{aligned}$$

Since $\alpha(t)$ is independent of ξ, this final integral is normally distributed, so its exponential is log-normally distributed. Denoting this exponent by $F(\alpha,\xi)$, this then has the property

$$\text{E}_\xi\left[e^{F(\alpha,\xi)}\right] = \exp\left(\text{E}_\xi[F(\alpha,\xi)] + \frac{1}{2}\text{E}_\xi[F^2(\alpha,\xi)]\right) \tag{8.50}$$

Here the mean of F is zero, while its variance can be computed by separating the coherent state amplitude into quadratures $\alpha = (X+iY)/\sqrt{2}$ and the zero-point noise into 1D Wiener

processes $\mathrm{d}\xi = (\mathrm{d}\xi_X + i\mathrm{d}\xi_Y)/\sqrt{2}$, and then making use of the Ito isometry.

$$\begin{aligned}
\frac{1}{2}\mathrm{E}_\xi[F^2(\alpha,\xi)] &= \gamma \mathrm{E}_\xi\left[\left(\int_0^t \alpha(\tau)\mathrm{d}\xi + \alpha^*(\tau)\mathrm{d}\xi^*\right)^2\right] &(8.51)\\
&= \gamma \mathrm{E}_\xi\left[\left(\int_0^t X(\tau)\mathrm{d}\xi_X\right)^2 + \left(\int_0^t Y(\tau)\mathrm{d}\xi_Y\right)^2\right] &(8.52)\\
&= \gamma \mathrm{E}_\xi\left[\int_0^t X^2(\tau) + Y^2(\tau)\mathrm{d}\tau\right] &(8.53)\\
&= 2\gamma\int_0^t |\alpha(\tau)|^2\mathrm{d}\tau &(8.54)
\end{aligned}$$

Substituting this back into Eq. (8.49) and taking the expectation over ζ leaves

$$\mathrm{E}_{\xi,\zeta}[\langle\psi(t)|\psi(t)\rangle] = \mathrm{E}_\zeta\left[\exp\left(\int_0^t -4\mu|\alpha(\tau)|^2\,\mathrm{d}\tau + 4\sqrt{\mu}\mathrm{Re}[\alpha(\tau)\mathrm{d}Z^*(\tau)]\right)\right] \quad (8.55)$$

8.6.1 Zero temperature

Let us first set $\zeta(t) = 0$. In this case, no further averaging is needed. Separating into quadratures gives

$$\mathrm{E}_\xi[\langle\psi(t)|\psi(t)\rangle] = \exp\left(\int_0^t -2\mu(X^2(\tau)+Y^2(\tau))\mathrm{d}\tau + 2\sqrt{\mu}(X(\tau)\mathrm{d}W_1(\tau) + Y(\tau)\mathrm{d}W_2(\tau))\right) \quad (8.56)$$

Now, separating each of the quadrature components into the initial parts (X_0,Y_0) and measurement residual parts (X_1,Y_1) as given by Eq. (8.18), the integral will contain terms linear and quadratic in both X_0 and Y_0. This can therefore be written

$$\mathrm{E}_\xi[\langle\psi(t)|\psi(t)\rangle] = \exp\left(\frac{-(X_0 - X_{\mathrm{est}})^2}{2\sigma^2} + G_X\right)\exp\left(\frac{-(Y_0 - Y_{\mathrm{est}})^2}{2\sigma^2} + G_Y\right) \quad (8.57)$$

where G_X and G_Y are terms independent of X_0 and Y_0. After normalising by an integral over initial states, these extraneous terms disappear and we are left with the simple 2D Gaussian (where $\alpha_{\mathrm{est}} = (X_{\mathrm{est}} + iY_{\mathrm{est}})/\sqrt{2}$)

$$P(\alpha_0|Z) = \frac{1}{\pi\sigma^2}\exp\left(\frac{-|\alpha(0) - \alpha_{\mathrm{est}}|^2}{2\sigma^2}\right) \quad (8.58)$$

The parameters of the distribution can be found by integrating Eq. (8.56), giving

$$\begin{aligned}
X_{est}(t) &= \frac{\Gamma_0}{1-e^{-2\Gamma_0 t}}\int_0^t \frac{1}{\sqrt{\mu}}\mathrm{d}W_1(\tau)e^{-\Gamma_0\tau} - 2\left(\sqrt{\mu}\int_0^\tau \mathrm{d}W_1(s)e^{\Gamma_0(s-2\tau)}\right)\mathrm{d}\tau &(8.59)\\
Y_{est}(t) &= \frac{\Gamma_0}{1-e^{-2\Gamma_0 t}}\int_0^t \frac{1}{\sqrt{\mu}}\mathrm{d}W_2(\tau)e^{-\Gamma_0\tau} - 2\left(\sqrt{\mu}\int_0^\tau \mathrm{d}W_2(s)e^{\Gamma_0(s-2\tau)}\right)\mathrm{d}\tau &(8.60)\\
\sigma^2(t) &= \frac{\Gamma_0}{2\mu(1-e^{-2\Gamma_0 t})} &(8.61)
\end{aligned}$$

We can see that the variance of the distribution reduces from infinity at $t = 0$, converging at $t \gg 1/\Gamma_0$ to

$$\sigma^2(t\to\infty) = 1 + \frac{\gamma}{2\mu} \quad (8.62)$$

Subtracting off the ground state variance of 1/2 gives the excess variance

$$\sigma_C^2(t \to \infty) = \frac{1}{2} + \frac{\gamma}{2\mu} \tag{8.63}$$

As shown in Section 8.5, this defines the smallest feature size of the initial state's Q-function that can be resolved in the reconstructed distribution without performing a deconvolution. This excess still includes a minimum variance (where $\mu \gg \gamma$) of 1/2 due to the fact that both quadratures are being detected[145]. The second term above quantifies the additional noise due to bath dissipation. In contrast, the steady-state conditional variance from the stochastic master equation is simply 1/2 for perfect efficiency and zero temperature. Therefore, an initial quantum state is fundamentally hard to image in the weak measurement limit.

The estimates can be rearranged into the form

$$X_{\text{est}}(t) = 2\sigma^2(t)\sqrt{\mu}\int_0^t [(1-\beta_0)e^{-\Gamma_0\tau} + \beta_0 e^{\Gamma_0(\tau-2t)}]\mathrm{d}W_1(\tau) \tag{8.64}$$

$$Y_{\text{est}}(t) = 2\sigma^2(t)\sqrt{\mu}\int_0^t [(1-\beta_0)e^{-\Gamma_0\tau} + \beta_0 e^{\Gamma_0(\tau-2t)}]\mathrm{d}W_2(\tau) \tag{8.65}$$

where

$$\beta_0 = \frac{\mu}{\Gamma_0} = \frac{\mu}{\gamma + 2\mu} \tag{8.66}$$

The first term is simply a weighted average of early of the early results following an exponential decay from $t = 0$. The second term is weighted towards late time results, and becomes more dominant as the measurement improves ($\mu \gg \gamma$) as long as the total measurement time t is not much longer than $1/\Gamma_0$. This term can be interpreted as compensating for the lack of measurement results in the case that the bandwidth of the measurement is too large. Notably, the filter decay rate Γ_0 matches that derived from the master equation at zero temperature given by Eq. (3.42).

8.6.2 Finite temperature

At nonzero temperature, a more difficult task is presented by the thermal noise in $\alpha(t)$, which must be averaged over. While Eq. (8.55) resembles the characteristic function of an integrated squared Ornstein-Uhlenbeck process, which has been treated previously[151, 152], the presence of an extra stochastic integral complicates matters. Heuristically, we can expect the presence of thermal noise to increase the estimate error as well as shorten the time constant of the filter. This is somewhat justified by behaviour of the optimal filter when estimating the current position, as derived in Section 3.5.1 using the stochastic master equation. In the case of perfect efficiency, this is given by

$$\Gamma_{\text{SME}} = \sqrt{\Gamma_0^2 + 8\mu\gamma N} \tag{8.67}$$

That is, the filter becomes wider as the measurement begins to pick up thermal fluctuations.

It is a simpler matter to find the estimate error σ^2 in the presence of thermal noise. Upon examining Eq. (8.55), the expectation value should be Gaussian distributed — that is, the

resulting exponent should be quadratic in X_0 and Y_0. However, the coefficient $1/2\sigma^2$ of these quadratic terms should be independent of the problematic term that is linear in α. Therefore setting $Z(t) = 0$ for all times, while not providing the estimates X_{est} and Y_{est}, will still produce the correct variance. Separating the resulting equation into quadratures leaves

$$\begin{aligned} \mathrm{E}_{\xi,\zeta}[\langle\psi(t)|\psi(t)\rangle] &= \mathrm{E}_{X2}\left[\exp\left(-2\mu\int_0^t (X_0 + X_2(t))^2 e^{-2\Gamma_0\tau}\,\mathrm{d}\tau\right)\right] \\ &\quad \times \mathrm{E}_{Y2}\left[\exp\left(-2\mu\int_0^t (Y_0 + Y_2(t))^2 e^{-2\Gamma_0\tau}\,\mathrm{d}\tau\right)\right] \end{aligned} \tag{8.68}$$

Each of these integrals is of a squared Ornstein-Uhlenbeck process with initial displacement X_0 and decay rate Γ_0. The expectation value of this function has been derived[152, 151], with the conditional solution in our parameters given by

$$\mathrm{E}_{X2}\left[\exp\left(-2\mu\int_0^t (X_0 + X_2(t))^2 e^{-2\Gamma_0\tau}\,\mathrm{d}\tau\right)\right] = f(t)\exp\left[\frac{-2\mu X_0^2}{\Gamma_0(1 + \lambda\coth(\lambda\Gamma_0 t))}\right] \tag{8.69}$$

where

$$\lambda = \sqrt{1 + 8\mu\gamma N/\Gamma_0^2} \tag{8.70}$$

The hyperbolic function above captures the effect of the error reducing from infinity at $t = 0$ to a steady-state value after some time. Notably the rate associated with this process is

$$\lambda\Gamma_0 = \sqrt{\Gamma_0^2 + 8\mu\gamma N} \tag{8.71}$$

This agrees precisely with the filter width Γ_{SME} derived from the stochastic master equation, given by Eq. (8.67), further justifying its use.

The thermal noise, as expected, leads to an increased final variance in the conditional probability, while also causing a faster convergence. The final error is

$$\sigma^2(t \to \infty) = \left(\frac{\gamma}{4\mu} + \frac{1}{2}\right)\left(1 + \sqrt{1 + \frac{8\mu\gamma N}{(\gamma + 2\mu)^2}}\right) \tag{8.72}$$

Subtracting the ground state variance of 1/2 and rearranging produces

$$\sigma_C^2 = V_0 + \frac{\gamma}{2\mu} \tag{8.73}$$

where V_0 is the conditional variance from the master equation given by Eq. (3.32). In the low SNR limit $N\mu/\gamma \ll 1$, this becomes

$$\sigma_C^2 \approx \frac{1}{2} + \frac{\gamma}{2\mu} + N \tag{8.74}$$

or, an addition of N to the zero-temperature case.

The conjecture for the filter bandwidth is backed up by numerical simulations performed using the Quantum Optics Toolbox[153]. The SSE given by Eq. (8.5) was simulated 10000

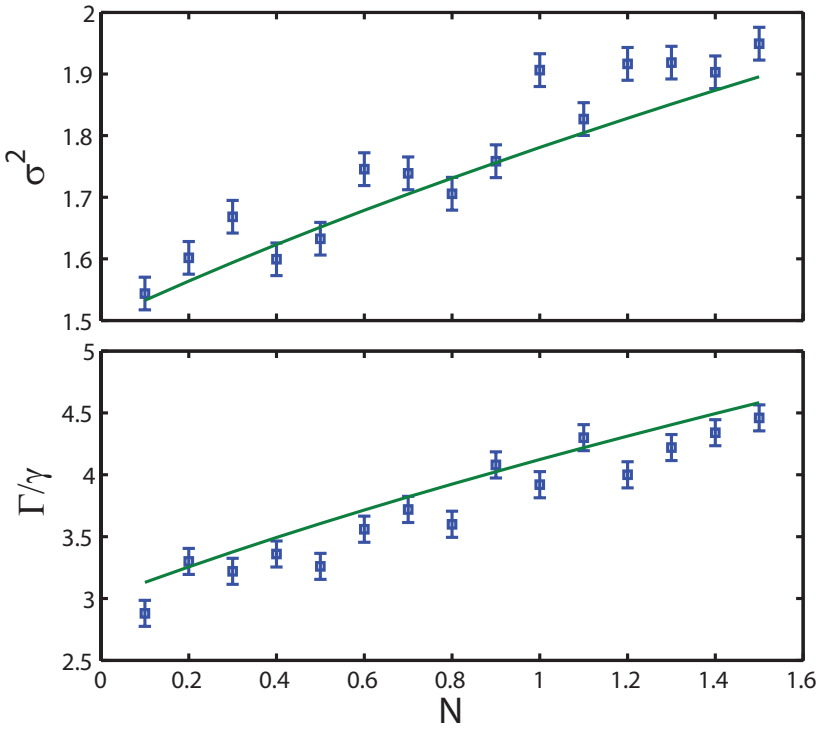

Figure 8.1: Optimal estimate variance (upper panel) and optimal filter width Γ (lower panel) as a function of temperature for $\mu = \gamma = 1$. Simulations were performed over one decay time, using 10000 trajectories for each temperature with only an early-time filter ($\beta = 0$). Solid lines are the analytic solutions for the same parameters given by Eqs (8.72) and (8.67) respectively.

times, using the measured record $Z(t)$ in each case to form an estimate X_{est} of an initial coherent state using various filter decays Γ for a simplified filter

$$X_{\text{est}}(t) = A \int_0^t e^{-\Gamma\tau} \mathrm{d}W(\tau) \tag{8.75}$$

where A is a constant found by optimisation. Although it is likely that the correct filter is of a similar form to Equation (8.64), here we have set the long-time filter parameter β to zero for simplicity.

The variance of X_{est} over all trajectories was computed for each Γ to find the minimum variance and corresponding filter width. Figure 8.1 shows these optimal parameters for various mean phonon occupations N, showing good agreement with the above analytic solutions. It is assumed that slight systematic error is due to the non-optimal restriction $\beta = 0$ for the long-time weighting.

8.7 Parametric amplification

While resonant parametric amplification (without feedback) has limited use in steady-state quantum measurement and control, as discussed in Chapter 4, it is well suited to non-steady-

state applications. Tomography of a state prepared at a particular time is one such example. Increased resolution of one quadrature is especially suitable for quantum-state tomography, which requires accurate single-quadrature marginals to be built up. Since steady-state operation is not required, a parametric drive far above threshold can be used to amplify the state unitarily in a short time compared to noise processes.

To model the effect of a parametric drive, the resonant squeezing Hamiltonian

$$\hat{H} = i\hbar\frac{\chi}{2}(e^{2i\theta}\hat{a}^2 - e^{-2i\theta}\hat{a}^{\dagger 2}) \tag{8.76}$$

can be inserted into the SSE given by Eq. (8.5). This results in an initial coherent state evolving into a squeezed coherent state. Linear quantum trajectories have been analysed for squeezed states[149, 145], but are difficult to solve analytically in the presence of multiple stochastic processes. In this section, we will use two alternative methods to build upon the above intuition.

8.7.1 Amplification with measurement: numerical results

It is easy to show through simulations that non-stationary amplification of a quadrature with simultaneous measurement results in improved resolution. Using a Quantum Optics Toolbox simulation of the SSE given by Eq. (8.5) with the above Hamiltonian, the stochastic squeezed state evolution can be solved numerically. A filter of the same form as Eq. (8.64) is applied to the X quadrature measurement record $W_1(t)$, varying the filter width Γ and the long-time weighting β. An estimate is produced for each combination of parameters from each trajectory, and the mean and variance of the estimates over all trajectories are then calculated.

Figure 8.2 shows the normalised variance for a measurement strength near the standard quantum limit, comparing the amplified, squeezed and undriven cases. Notably, the long-time weighting β has little effect on the estimate error. In the case where the X quadrature is amplified, the optimal variance is reduced along with the optimal filter width. When θ is set so that the X quadrature is squeezed, the opposite occurs. The behaviour of the optimal filter is consistent with the qualitative picture of reduced and increased effective damping rates for the amplified and squeezed quadratures, respectively.

8.7.2 Parametric preamplification

Here we consider a two step process. First, one quadrature is parametrically amplified well above threshold and without measurement until a time t_1. Second, the drive is turned off and the oscillator is measured continuously as in the last section. The first step can be modelled with ensemble averages, using the mean and variance of $X(t_1)$ to determine the signal-to-noise for an estimate of $X(0)$. Then, up to some normalisation, the probability distribution conditioned on a measurement record Z is

$$P(X(0)|Z) = A\int_{-\infty}^{\infty} P(X(0)|X(t_1))P(X(t_1)|Z)\,\mathrm{d}X(t_1) \tag{8.77}$$

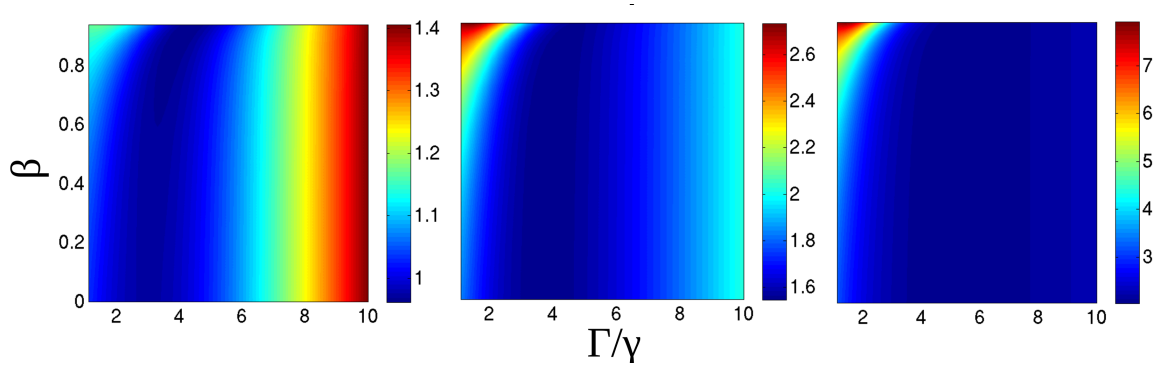

Figure 8.2: Normalised variance $\mathrm{Var}(X_{\mathrm{est}})/\langle X_{\mathrm{est}}\rangle^2$ plotted against filter parameters, using 200 simulated trajectories over one decay time, with a measurement strength $\mu = \gamma$. The central panel is for no parametric drive and is consistent with the theoretical optimal variance of $\sigma^2 = 1.5$. The left and right panels are for X being antisqueezed and squeezed respectively, with $\chi = 2\gamma$.

where A is some constant. Both of these probabilities are Gaussian distributed, and the first can be computed using the ensemble average. The mean value evolution is found using the squeezing Hamiltonian (8.76) in the Lindblad equation (3.1), with the solution

$$\langle X(t)\rangle = \langle X(0)\rangle e^{(\chi-\gamma)t} \tag{8.78}$$

$$= \langle X(0)G(t)\rangle \tag{8.79}$$

while the variance is found in the same way, with the solution

$$V_X(t) = \frac{\gamma(N+1/2)}{\chi-\gamma}(G^2(t)-1) + V_X(0)G^2(t) \tag{8.80}$$

The probability distribution is then

$$P(X(0)|X(t_1)) = \exp\left(\frac{(X_0 - X(t_1)/G^2(t_1)}{2V_X(t_1)/G^2(t_1)}\right) \tag{8.81}$$

so that the excess variance, if the amplification time t_1 is sufficiently long, is

$$\frac{V_X(t_1)}{G^2(t_1)} - V_X(0) = \frac{\gamma(N+1/2)}{\chi-\gamma} \tag{8.82}$$

The measurement step introduces the error $\sigma^2(t-t_1)$ as given by (8.72), but this error is for estimating the amplified signal $X(t_1)$ and is therefore rescaled by $G(t_1)$. Therefore, after the convolution in Eq. (8.77), the final variance of the estimate is

$$V_{\mathrm{est}}(t) = \frac{\sigma^2(t-t_1) + V_X(t_1)}{G^2(t_1)} - V_X(0) \tag{8.83}$$

Although σ^2 blows up in the weak measurement limit, this can be made negligable by making the amplification time t_1 very long. The excess variance can then be made as small as that in Eq. (8.82), which beats the heterodyne limit when $\chi > 2\gamma(N+1)$. This condition corresponds to

fluctuations being amplified faster than new fluctuations can be introduced, and is remarkably similar to that required for quantum squeezing via DMPA, as derived in Section 6.3. The error can be reduced further, as shown in the previous section, by using the measurement results during the amplification. Therefore, the above expression sets an upper bound on the error of the optimal estimate, which will be derived in future work.

The work in this chapter lays some important foundations towards tomography of mechanical states by extending some common ideas from quantum optics to the mechanical regime. The stochastic Schrödinger equation, while more complex than the optical case, does not completely inhibit rigorous analytic solutions. The use of this technique for optimal posterior estimation under various kinds of unitary evolution, including parametric amplification, holds great promise for the verification of quantum states in mechanical systems.

Chapter 9

Conclusions and future work

Measurement and control are not separable concepts — they intersect in many ways, in both classical and quantum regimes. Often, they are mutually exclusive goals. For example, amplification aids measurement of an observable while increasing its uncertainty after the fact, making precise control more difficult. Because of this, parametric amplification of an oscillator has generally been studied in the context of either measurement or control in isolation. For example, the reviews by Clerk et al.[21] and Blencowe[26] analysed parametric amplification of quadratures on resonance with an oscillator in the quantum regime. In this case, the squeezing effect can be used to prepare a quantum state of the oscillator at very low temperatures, while the amplification effect can be used to overcome measurement noise.

In quantum mechanics, where the act of measurement prepares states, measurement and control can be viewed as two sides of the same coin. The purest manifestation of this is quantum non-demolition measurement, in which the measurement does not add noise to the observable. Backaction evasion is the application of this idea to the continuous measurement of an oscillator. This stands in stark contrast to resonant parametric amplification, where either measurement or control is the focus, but not both.

This thesis has extended the application of parametric amplification of a mechanical oscillator in two ways. Firstly, it has examined the more complex dynamics of an oscillator that is not resonant with a parametric drive. In this case, the roles of measurement and control become mixed. A quadrature of motion can be simultaneously measured and localised with better precision by amplifying the dynamically linked orthogonal quadrature. The idea of using dynamically linked observables is not new in quantum measurement, and has been applied to coupled optical modes[154]. The major consequence of this result is that arbitrarily squeezed conditional mechanical states can be prepared in the steady-state without the use of strong measurement or feedback. This goal was previously considered out of reach due to the below-threshold requirements of a resonant parametric drive. A detuned parametric drive can be used as a replacement for strong and efficient backaction evading measurement, and in a special case the two are equivalent. Furthermore, extending these dynamics to coupled oscillators achieves effective collective-mode measurement and thus quantum entanglement.

These results present more options for experimentalists wishing to achieve steady-state squeezing or entanglement in mechanical oscillators. Specifically, they are relevant for experimentalists working with electromechanical or hybrid systems, as an alternative to purely measurement-based techniques. For theorists, the results also pave the way for further exploration of coherent dynamics in the quantum measurement framework set by the stochastic master equation formalism.

The second extended application presented here is above-threshold parametric amplification for state tomography. The property of noiseless amplification is useful out-of-equilibrium in an oscillator in a similar way as for travelling waves in optics. In this case, the parallels between tomography based on parametric amplification and on strong stroboscopic measurement are clear. Here, an upper bound has been derived for the minimum possible error in the reconstructed Q-function in the presence of a parametric drive, and the groundwork has been laid for an exact solution. This sets a clear path for further theoretical study, both in finding a solution for the error and in deconvolution techniques to reconstruct the Q-function. Once these are addressed, this scheme could prove very useful in electromechanical systems in which quantum state preparation will soon be possible, but verification may still be challenging.

Finally, it is worth asking what other forms a parametric drive could take. In this thesis, a classical drive was implicitly considered by adding a sinusoidal term to the oscillator spring constant. It is also possible to achieve the same effect using a second oscillatory mode with quadratic position coupling to the first. One idealisation of this arrangement is a mass-spring system with an additional sideways degree of freedom, such that it also behaves as a pendulum. Since the pendulum frequency depends on its length, the pendulum mode forms a parametric coupling with the mass-spring mode. This applies with equal validity to bulk oscillators, in which frequency pulling due to the mean-square vibration of an orthogonal mode has already been demonstrated[155, 156]. Nonlinear intermodal coupling opens up the possibility of squared position measurement[49, 41] via linear position measurement of a coupled mode, as well as parametric amplification in a regime analogous to the "depleted pump" regime in quantum optics[157]. A combination of these phenomena can be examined in a similar master equation framework to that presented here.

Bibliography

[1] Maximilian Schlosshauer. Decoherence, the measurement problem, and interpretations of quantum mechanics. *Rev. Mod. Phys.*, 76:1267–1305, 2005.

[2] L. Diósi. Models for universal reduction of macroscopic quantum fluctuations. *Phys. Rev. A*, 40:1165–1174, 1989.

[3] Igor Pikovski, Michael R. Vanner, Markus Aspelmeyer, M. S. Kim, and Caslav Brukner. Probing planck-scale physics with quantum optics. *Nature Physics*, 8:393–397, 2012.

[4] Markus Arndt and Klaus Hornberger. Testing the limits of quantum mechanical superpositions. *Nature Physics*, 10:271–277, 2014.

[5] Klaus Hornberger, Stefan Gerlich, Philipp Haslinger, Stefan Nimmrichter, and Markus Arndt. Quantum interference of clusters and molecules. *Rev. Mod. Phys.*, 84:157–173, 2012.

[6] Brian Julsgaard, Alexander Kozhekin, and Eugene S. Polzik. Experimental long-lived entanglement of two macroscopic objects. *Nature*, 413:400 – 403, 2001.

[7] D. M. Meekhof, C. Monroe, B. E. King, W. M. Itano, and D. J. Wineland. Generation of nonclassical motional states of a trapped atom. *Phys. Rev. Lett.*, 76:1796–1799, 1996.

[8] David J. Wineland. Nobel lecture: Superposition, entanglement, and raising schrödingers cat. *Rev. Mod. Phys.*, 85:1103–1114, 2013.

[9] D. E. Chang, C. A. Regal, S. B. Papp, D. J. Wilson, J. Ye, O. Painter, H. J. Kimble, and P. Zoller. Cavity opto-mechanics using an optically levitated nanosphere. *Proc. Nat. Acad. Sci.*, 107(3):1005–1010, 2010.

[10] O. Romero-Isart, A. C. Pflanzer, F. Blaser, R. Kaltenbaek, N. Kiesel, M. Aspelmeyer, and J. I. Cirac. Large quantum superpositions and interference of massive nanometer-sized objects. *Phys. Rev. Lett.*, 107:020405, 2011.

[11] M. D. Eisaman, J. Fan, A. Migdall, and S. V. Polyakov. Invited review article: Single-photon sources and detectors. *Review of Scientific Instruments*, 82(7):–, 2011.

[12] T. R. Albrecht, P. Grütter, D. Horne, and D. Rugar. Frequency modulation detection using highq cantilevers for enhanced force microscope sensitivity. *Journal of Applied Physics*, 69(2), 1991.

[13] K. L. Ekinci and M. L. Roukes. Nanoelectromechanical systems. *Rev. Sci. Instrum.*, 76(6):061101, 2005.

[14] K. L. Ekinci, Y. T. Yang, and M. L. Roukes. Ultimate limits to inertial mass sensing based upon nanoelectromechanical systems. *Journal of Applied Physics*, 95(5), 2004.

[15] M. Poggio, C. L. Degen, H. J. Mamin, and D. Rugar. Feedback cooling of a cantilever's fundamental mode below 5 mk. *Phys. Rev. Lett.*, 99:017201, 2007.

[16] Jennifer C. Driggers, Matthew Evans, Keenan Pepper, and Rana Adhikari. Active noise cancellation in a suspended interferometer. *Review of Scientific Instruments*, 83(2, Part 1), Feb 2012.

[17] Michael A. Taylor, Alex Szorkovszky, Joachim Knittel, Kwan H. Lee, Terry G. McRae, and Warwick P. Bowen. Cavity optoelectromechanical regenerative amplification. *Opt. Express*, 20(12):12742–12751, 2012.

[18] Glen I. Harris, David L. McAuslan, Thomas M. Stace, Andrew C. Doherty, and Warwick P. Bowen. Minimum requirements for feedback enhanced force sensing. *Phys. Rev. Lett.*, 111:103603, 2013.

[19] D.L. Hall and A.B. Flatau. On analog feedback control for magnetostrictive transducer linearisation. *Journal of Sound and Vibration*, 211(3):481–494, 1998.

[20] O.L.R. Jacobs. *Introduction to Control Theory*. Oxford, New York, 1993.

[21] A. A. Clerk, M. H. Devoret, S. M. Girvin, Florian Marquardt, and R. J. Schoelkopf. Introduction to quantum noise, measurement, and amplification. *Rev. Mod. Phys.*, 82:1155–1208, 2010.

[22] Carlton M. Caves. Quantum limits on noise in linear amplifiers. *Phys. Rev. D*, 26:1817–1839, 1982.

[23] B. Yurke, L. R. Corruccini, P. G. Kaminsky, L. W. Rupp, A. D. Smith, A. H. Silver, R. W. Simon, and E. A. Whittaker. Observation of parametric amplification and deamplification in a josephson parametric amplifier. *Phys. Rev. A*, 39:2519–2533, 1989.

[24] Junho Suh, Matthew D. LaHaye, Pierre M. Echternach, Keith C. Schwab, and Michael L. Roukes. Parametric amplification and back-action noise squeezing by a qubit-coupled nanoresonator. *Nano Lett.*, 10(10):3990–3994, 2010.

[25] D. Rugar and P. Grütter. Mechanical parametric amplification and thermomechanical noise squeezing. *Phys. Rev. Lett.*, 67(6):699–702, 1991.

[26] M. Blencowe. Quantum electromechanical systems. *Phys. Rep.*, 395:159–222, 2004.

[27] E. Verhagen, S. Deleglise, S. Weis, A. Schliesser, and T. J. Kippenberg. Quantum-coherent coupling of a mechanical oscillator to an optical cavity mode. *Nature*, 482(7383):63–67, 2012.

[28] T. A. Palomaki, J. W. Harlow, J. D. Teufel, R. W. Simmonds, and K. W. Lehnert. Coherent state transfer between itinerant microwave fields and a mechanical oscillator. *Nature*, 495(7440):210–214, 2013.

[29] A. N. Cleland and M. R. Geller. Superconducting qubit storage and entanglement with nanomechanical resonators. *Phys. Rev. Lett.*, 93:070501, 2004.

[30] P. Rabl, S. J. Kolkowitz, F. H. L. Koppens, J. G. E. Harris, P. Zoller, and M. D. Lukin. A quantum spin transducer based on nanoelectromechanical resonator arrays. *Nat Phys*, 6:602 – 608.

[31] J. Bochmann, A. Vainsencher, D.D. Awschalom, and A.N. Cleland. Nanomechanical coupling between microwave and optical photons. *Nature Phys.*, 2013.

[32] R. W. Andrews, R. W. Peterson, T. P. Purdy, K. Cicak, R. W. Simmonds, C. A. Regal, and K. W. Lehnert. Bidirectional and efficient conversion between microwave and optical light. *Nature Physics*, 10:321–326, 2014.

[33] Tobias J. Kippenberg and Kerry J. Vahala. Cavity opto-mechanics. *Opt. Express*, 15(25):17172–17205, 2007.

[34] Markus Aspelmeyer, Pierre Meystre, and Keith Schwab. Quantum optomechanics. *Physics Today*, 65(7):29–35, 2012.

[35] Carlton M. Caves, Kip S. Thorne, Ronald W. P. Drever, Vernon D. Sandberg, and Mark Zimmermann. On the measurement of a weak classical force coupled to a quantum-mechanical oscillator. i. issues of principle. *Rev. Mod. Phys.*, 52(2):341–392, 1980.

[36] V.B. Braginsky and F.Y. Khalili. *Quantum Measurement*. Cambridge, London, 1995.

[37] M. D. LaHaye, J. Suh, P. M. Echternach, K. C. Schwab, and M. L. Roukes. Nanomechanical measurements of a superconducting qubit. *Nature*, 459(7249):960–964, 2009.

[38] M. R. Vanner, J. Hofer, G. D. Cole, and M. Aspelmeyer. Cooling-by-measurement and mechanical state tomography via pulsed optomechanics. *Nature Communications*, 4(3295), 2013.

[39] A. Schliesser, O. Arcizet, R. Riviere, G. Anetsberger, and T. J. Kippenberg. Resolved-sideband cooling and position measurement of a micromechanical oscillator close to the heisenberg uncertainty limit. *Nat. Phys.*, 5:509–514, 2009.

[40] J. Chan, T. P. M. Alegre, A. H. Safavi-Naeini, J. T. Hill, A. Krause, S. Gröblacher, M. Aspelmeyer, and O. Painter. Laser cooling of a nanomechanical oscillator into its quantum ground state. *Nature*, 478:89–92, 2011.

[41] A M Jayich, J C Sankey, B M Zwickl, C Yang, J D Thompson, S M Girvin, A A Clerk, F Marquardt, and J G E Harris. Dispersive optomechanics: a membrane inside a cavity. *New Journal of Physics*, 10(9):095008, 2008.

[42] J. D. Teufel, J. W. Harlow, C. A. Regal, and K. W. Lehnert. Dynamical backaction of microwave fields on a nanomechanical oscillator. *Phys. Rev. Lett.*, 101:197203, 2008.

[43] J. D. Teufel, T. Donner, D. Li, J. W. Harlow, M. S. Allman, K. Cicak, A. J. Sirois, J. D. Whittaker, K. W. Lehnert, and R. W. Simmonds. Sideband cooling of micromechanical motion to the quantum ground state. *Nature*, 475:359–363, 2011.

[44] André Xuereb, Claudiu Genes, and Aurélien Dantan. Strong coupling and long-range collective interactions in optomechanical arrays. *Phys. Rev. Lett.*, 109:223601, 2012.

[45] Max Ludwig, Björn Kubala, and Florian Marquardt. The optomechanical instability in the quantum regime. *New Journal of Physics*, 10(9):095013, 2008.

[46] A. A. Clerk, F. Marquardt, and K. Jacobs. Back-action evasion and squeezing of a mechanical resonator using a cavity detector. *New J. Phys.*, 10(9):095010, 2008.

[47] Pierre Verlot, Alexandros Tavernarakis, Chiara Molinelli, Aurélien Kuhn, Thomas Antoni, Slawomir Gras, Tristan Briant, Pierre-Francois Cohadon, Antoine Heidmann, Laurent Pinard, Christophe Michel, Raffaele Flaminio, Michaël Bahriz, Olivier Le Traon, Izo Abram, Alexios Beveratos, Rémy Braive, Isabelle Sagnes, and Isabelle Robert-Philip. Towards the experimental demonstration of quantum radiation pressure noise. *Comptes Rendus Physique*, 12(9–10):826–836, 2011.

[48] J. Suh, A. J. Weinstein, C. U. Lei, E. E. Wollman, S. K. Steinke, P. Meystre, A. A. Clerk, and K. C. Schwab. Mechanically detecting and avoiding the quantum fluctuations of a microwave field. *Science*, 344(6189):1262–1265, 2014.

[49] A A Gangat, T M Stace, and G J Milburn. Phonon number quantum jumps in an optomechanical system. *New J. Phys.*, 13(4):043024, 2011.

[50] Michael R. Vanner. Selective linear or quadratic optomechanical coupling via measurement. *Phys. Rev. X*, 1:021011, 2011.

[51] S Basiri-Esfahani, U Akram, and G J Milburn. Phonon number measurements using single photon opto-mechanics. *New Journal of Physics*, 14(8):085017, 2012.

[52] Shimon Kolkowitz, Ania C. Bleszynski Jayich, Quirin P. Unterreithmeier, Steven D. Bennett, Peter Rabl, J. G. E. Harris, and Mikhail D. Lukin. Coherent sensing of a mechanical resonator with a single-spin qubit. *Science*, 335(6076):1603–1606, 2012.

[53] Robert G. Knobel and Andrew N. Cleland. Nanometre-scale displacement sensing using a single electron transistor. *Nature*, 424(6946):291–293, 2003.

[54] A. N. Cleland, J. S. Aldridge, D. C. Driscoll, and A. C. Gossard. Nanomechanical displacement sensing using a quantum point contact. *Applied Physics Letters*, 81(9), 2002.

[55] Yuma Okazaki, Imran Mahboob, Koji Onomitsu, Satoshi Sasaki, and Hiroshi Yamaguchi. Quantum point contact displacement transducer for a mechanical resonator at sub-kelvin temperatures. *Applied Physics Letters*, 103(19):–, 2013.

[56] I. Mahboob and H. Yamaguchi. Bit storage and bit flip operations in an electromechanical oscillator. *Nat. Nano.*, 3:275–279, 2008.

[57] R. Almog, S. Zaitsev, O. Shtempluck, and E. Buks. Noise squeezing in a nanomechanical duffing resonator. *Phys. Rev. Lett.*, 98(7):078103, 2007.

[58] Mika A. Sillanpää, Raphaël Khan, Tero T. Heikkilä, and Pertti J. Hakonen. Macroscopic quantum tunneling in nanoelectromechanical systems. *Phys. Rev. B*, 84:195433, 2011.

[59] Kurt Jacobs, Pavel Lougovski, and Miles Blencowe. Continuous measurement of the energy eigenstates of a nanomechanical resonator without a nondemolition probe. *Phys. Rev. Lett.*, 98:147201, 2007.

[60] Quirin P. Unterreithmeier, Eva M. Weig, and Jorg P. Kotthaus. Universal transduction scheme for nanomechanical systems based on dielectric forces. *Nature*, 458:1001, 2009.

[61] H. Okamoto, A. Gourgout, C-Y. Chang, K. Onomitsu, I. Mahboob, E.Y. Chang, and H. Yamaguchi. Coherent phonon manipulation in coupled mechanical resonators. *Nature Phys.*, 2013.

[62] T. Faust, J. Rieger, M.J. Seitner, J.P. Kotthaus, and E.M. Weig. Coherent control of a classical nanomechanical two-level system. *Nature Phys.*, 9:485–488, 2013.

[63] T. Niemczyk, F. Deppe, H. Huebl, E. P. Menzel, F. Hocke, M. J. Schwarz, J. J. Garcia-Ripoll, D. Zueco, T. Hummer, E. Solano, A. Marx, and R. Gross. Circuit quantum electrodynamics in the ultrastrong-coupling regime. *Nat Phys*, 6(10):772–776, 2010.

[64] D. I. Schuster, A. A. Houck, J. A. Schreier, A. Wallraff, J. M. Gambetta, A. Blais, L. Frunzio, J. Majer, B. Johnson, M. H. Devoret, S. M. Girvin, and R. J. Schoelkopf. Resolving photon number states in a superconducting circuit. *Nature*, 445(7127):515–518, 2007.

[65] Suresh Sridaran and Sunil A. Bhave. Electrostatic actuation of silicon optomechanical resonators. *Opt. Exp.*, 19(10):9020–9026, 2011.

[66] S Rips, M Kiffner, I Wilson-Rae, and M J Hartmann. Steady-state negative wigner functions of nonlinear nanomechanical oscillators. *New Journal of Physics*, 14(2):023042, 2012.

[67] Kwan H. Lee, Terry G. McRae, Glen I. Harris, Joachim Knittel, and Warwick P. Bowen. Cooling and control of a cavity optoelectromechanical system. *Phys. Rev. Lett.*, 104(12):123604, 2010.

[68] M. Winger, T. D. Blasius, T. P. Mayer Alegre, A. H. Safavi-Naeini, S. Meenehan, J. Cohen, S. Stobbe, and O. Painter. A chip-scale integrated cavity-electro-optomechanics platform. *Opt. Express*, 19(25):24905–24921, 2011.

[69] C A Regal and K W Lehnert. From cavity electromechanics to cavity optomechanics. *Journal of Physics: Conference Series*, 264(1):012025, 2011.

[70] J. S. Neergaard-Nielsen, B. Melholt Nielsen, C. Hettich, K. Mølmer, and E. S. Polzik. Generation of a superposition of odd photon number states for quantum information networks. *Phys. Rev. Lett.*, 97:083604, 2006.

[71] W. P. Bowen, R. Schnabel, P. K. Lam, and T. C. Ralph. Experimental investigation of criteria for continuous variable entanglement. *Phys. Rev. Lett.*, 90:043601, 2003.

[72] Animesh Datta and Guifre Vidal. Role of entanglement and correlations in mixed-state quantum computation. *Phys. Rev. A*, 75:042310, 2007.

[73] A. Einstein, B. Podolsky, and N. Rosen. Can quantum-mechanical description of physical reality be considered complete? *Phys. Rev.*, 47:777–780, 1935.

[74] M. D. Reid, P. D. Drummond, W. P. Bowen, E. G. Cavalcanti, P. K. Lam, H. A. Bachor, U. L. Andersen, and G. Leuchs. The einstein-podolsky-rosen paradox: From concepts to applications. *Rev. Mod. Phys.*, 81:1727–1751, 2009.

[75] Z. Y. Ou, S. F. Pereira, H. J. Kimble, and K. C. Peng. Realization of the einstein-podolsky-rosen paradox for continuous variables. *Phys. Rev. Lett.*, 68:3663–3666, 1992.

[76] Samuel L. Braunstein and Peter van Loock. Quantum information with continuous variables. *Rev. Mod. Phys.*, 77:513–577, 2005.

[77] R. Simon. Peres-horodecki separability criterion for continuous variable systems. *Phys. Rev. Lett.*, 84:2726–2729, 2000.

[78] Lu-Ming Duan, G. Giedke, J. I. Cirac, and P. Zoller. Inseparability criterion for continuous variable systems. *Phys. Rev. Lett.*, 84:2722–2725, 2000.

[79] Ryszard Horodecki, Paweł Horodecki, Michał Horodecki, and Karol Horodecki. Quantum entanglement. *Rev. Mod. Phys.*, 81:865–942, 2009.

[80] W. P. Bowen, R. Schnabel, P. K. Lam, and T. C. Ralph. Experimental characterization of continuous-variable entanglement. *Phys. Rev. A*, 69:012304, 2004.

[81] M. D. Reid. The einstein-podolsky-rosen paradox and entanglement 1: Signatures of epr correlations for continuous variables. *arXiv*, [quant-ph] 0112038, 2001.

[82] A. C. Doherty, A. Szorkovszky, G.I. Harris, and W.P. Bowen. A simplified discussion of the stochastic master equation approach to quantum feedback control of an oscillator. *Phil. Trans. R. Soc. A*, 370(1979), 2012.

[83] C.W. Gardiner and P. Zoller. *Quantum Noise*. Springer, Berlin, 2004.

[84] Daniel T. Gillespie. The mathematics of brownian motion and johnson noise. *American Journal of Physics*, 64(3), 1996.

[85] A. C. Doherty and K. Jacobs. Feedback control of quantum systems using continuous state estimation. *Phys. Rev.*, 60:2700–2711, 1999.

[86] Kurt Jacobs and Daniel A. Steck. A straightforward introduction to continuous quantum measurement. *Contemp. Phys.*, 47(5):279–303, 2006.

[87] Howard M. Wiseman and Gerard J. Milburn. *Quantum Measurement and Control*. Cambridge University Press, Cambridge, 1999.

[88] A. H. Safavi-Naeini, T. P. Mayer Alegre, J. Chan, M. Eichenfield, M. Winger, Q. Lin, J. T. Hill, D. E. Chang, and O. Painter. Electromagnetically induced transparency and slow light with optomechanics. *Nature*, 472(7341):69–73, 2011.

[89] H. M. Wiseman and G. J. Milburn. Squeezing via feedback. *Phys. Rev.*, 49(2):1350–1366, 1994.

[90] R. J. Sewell, M. Napolitano, N. Behbood, G. Colangelo, and M. W. Mitchell. Certified quantum non-demolition measurement of a macroscopic material system. *Nat. Photon*, 7:517–520, 2013.

[91] J. B. Hertzberg, T. Rocheleau, T. Ndukum, M. Savva, A. A. Clerk, and K. C. Schwab. Back-action-evading measurements of nanomechanical motion. *Nat. Phys.*, 6(3):213, 2010.

[92] Paul G. Kwiat, Klaus Mattle, Harald Weinfurter, Anton Zeilinger, Alexander V. Sergienko, and Yanhua Shih. New high-intensity source of polarization-entangled photon pairs. *Phys. Rev. Lett.*, 75:4337–4341, 1995.

[93] G. Breitenbach, S. Schiller, and J. Mlynek. Measurement of the quantum states of squeezed light. *Nature*, 387(6632):471–475, 1997.

[94] Kimberly L. Turner, Scott A. Miller, Peter G. Hartwell, Noel C. MacDonald, Steven H. Strogatz, and Scott G. Adams. Five parametric resonances in a microelectromechanical system. *Nature*, 396(6707):149–152, 1998.

[95] Dustin W. Carr, Stephane Evoy, Lidija Sekaric, H. G. Craighead, and J. M. Parpia. Parametric amplification in a torsional microresonator. *Applied Physics Letters*, 77(10), 2000.

[96] C. M. Wilson, T. Duty, M. Sandberg, F. Persson, V. Shumeiko, and P. Delsing. Photon generation in an electromagnetic cavity with a time-dependent boundary. *Phys. Rev. Lett.*, 105:233907, 2010.

[97] Erik A. Tholn, Adem Ergl, Evelyn M. Doherty, Frank M. Weber, Fabien Grgis, and David B. Haviland. Nonlinearities and parametric amplification in superconducting coplanar waveguide resonators. *Applied Physics Letters*, 90(25), 2007.

[98] M. J. Collett and C. W. Gardiner. Squeezing of intracavity and traveling-wave light fields produced in parametric amplification. *Phys. Rev.*, 30(3):1386–1391, 1984.

[99] A. D. O'Connell, M. Hofheinz, M. Ansmann, Radoslaw C. Bialczak, M. Lenander, Erik Lucero, M. Neeley, D. Sank, H. Wang, M. Weides, J. Wenner, John M. Martinis, and A. N. Cleland. Quantum ground state and single-phonon control of a mechanical resonator. *Nature*, 464:697, 2010.

[100] A. Vinante and P. Falferi. Feedback-enhanced parametric squeezing of mechanical motion. *Phys. Rev. Lett.*, 111:207203, 2013.

[101] X.-Y. Lü, J.-Q. Liao, L. Tian, and F. Nori. Steady-state Mechanical Squeezing in an Optomechanical System via Duffing Nonlinearity. *arXiv*, [quant-ph] 1403.0049, 2014.

[102] H. J. Carmichael, G. J. Milburn, and D. F. Walls. Squeezing in a detuned parametric amplifier. *J. Phys.*, 17(2):469, 1984.

[103] Michael V. Requa. *PhD thesis: Parametric Resonance in Microcantilevers with Application in Mass Sensing.* University of California, Santa Barbara, 2006.

[104] Vasant Natarajan, Frank DiFilippo, and David E. Pritchard. Classical squeezing of an oscillator for subthermal noise operation. *Phys. Rev. Lett.*, 74:2855–2858, 1995.

[105] J. Mertz, O. Marti, and J. Mlynek. Regulation of a microcantilever response by force feedback. *Appl. Phys. Lett.*, 62(19):2344–2346, 1993.

[106] David Vitali, Stefano Mancini, Luciano Ribichini, and Paolo Tombesi. Mirror quiescence and high-sensitivity position measurements with feedback. *Phys. Rev. A*, 65:063803, 2002.

[107] D.M. Weld and A. Kapitulnik. Feedback control and characterization of a microcantilever using optical radiation pressure. *Appl. Phys. Lett.*, 89(16):164102–164102, 2006.

[108] A Schliesser, G Anetsberger, R Rivi?re, O Arcizet, and T J Kippenberg. High-sensitivity monitoring of micromechanical vibration using optical whispering gallery mode resonators. *New Journal of Physics*, 10(9):095015, 2008.

[109] Simon Groblacher, Klemens Hammerer, Michael R. Vanner, and Markus Aspelmeyer. Observation of strong coupling between a micromechanical resonator and an optical cavity field. *Nature*, 460(7256):724–727, 2009.

[110] R. B. Karabalin, X. L. Feng, and M. L. Roukes. Parametric nanomechanical amplification at very high frequency. *Nano Lett.*, 9(9):3116–3123, 2009.

[111] Johannes Rieger, Thomas Faust, Maximilian J. Seitner, Jörg P. Kotthaus, and Eva M. Weig. Frequency and q factor control of nanomechanical resonators. *Applied Physics Letters*, 101(10), 2012.

[112] B. H. Schneider, S. Etaki, H. S. J. van der Zant, and G. A. Steele. Coupling carbon nanotube mechanics to a superconducting circuit. *Sci. Rep*, 2:599, 2012.

[113] J. Suh, M. D. Shaw, H. G. LeDuc, A. J. Weinstein, and K. C. Schwab. Thermally induced parametric instability in a back-action evading measurement of a micromechanical quadrature near the zero-point level. *Nano Letters*, 12(12):6260–6265, 2012.

[114] M. J. Woolley and A. A. Clerk. Two-mode back-action-evading measurements in cavity optomechanics. *Phys. Rev. A*, 87:063846, 2013.

[115] T. P. Purdy, R. W. Peterson, and C. A. Regal. Observation of radiation pressure shot noise on a macroscopic object. *Science*, 339(6121):801–804, 2013.

[116] Simon Gröblacher, Jeff T. Hill, Amir H. Safavi-Naeini, Jasper Chan, and Oskar Painter. Highly efficient coupling from an optical fiber to a nanoscale silicon optomechanical cavity. *Appl. Phys. Lett.*, 103(18), 2013.

[117] A. Naik, O. Buu, M. D. LaHaye, A. D. Armour, A. A. Clerk, M. P. Blencowe, and K. C. Schwab. Cooling a nanomechanical resonator with quantum back-action. *Nature*, 443(7108):193–196, 2006.

[118] Andreas Kronwald, Florian Marquardt, and Aashish A. Clerk. Arbitrarily large steady-state bosonic squeezing via dissipation. *Phys. Rev. A*, 88:063833, 2013.

[119] M. J. Woolley, A. C. Doherty, G. J. Milburn, and K. C. Schwab. Nanomechanical squeezing with detection via a microwave cavity. *Phys. Rev.*, 78(6):062303, 2008.

[120] Florian Marquardt, Joe P. Chen, A. A. Clerk, and S. M. Girvin. Quantum theory of cavity-assisted sideband cooling of mechanical motion. *Phys. Rev. Lett.*, 99:093902, 2007.

[121] S. Mancini and P. Tombesi. High-sensitivity force measurement using entangled probes. *EPL (Europhysics Letters)*, 61(1):8, 2003.

[122] Clemens Gneiting and Klaus Hornberger. Detecting entanglement in spatial interference. *Phys. Rev. Lett.*, 106:210501, 2011.

[123] Johannes Kofler, Mandip Singh, Maximilian Ebner, Michael Keller, Mateusz Kotyrba, and Anton Zeilinger. Einstein-podolsky-rosen correlations from colliding bose-einstein condensates. *Phys. Rev. A*, 86:032115, 2012.

[124] Michael Schmidt, Max Ludwig, and Florian Marquardt. Optomechanical circuits for nanomechanical continuous variable quantum state processing. *New Journal of Physics*, 14(12):125005, 2012.

[125] Stefano Mancini, Vittorio Giovannetti, David Vitali, and Paolo Tombesi. Entangling macroscopic oscillators exploiting radiation pressure. *Phys. Rev. Lett.*, 88:120401, 2002.

[126] M. Paternostro, D. Vitali, S. Gigan, M. S. Kim, C. Brukner, J. Eisert, and M. Aspelmeyer. Creating and probing multipartite macroscopic entanglement with light. *Phys. Rev. Lett.*, 99:250401, 2007.

[127] H. Seok, L. F. Buchmann, E. M. Wright, and P. Meystre. Multimode strong-coupling quantum optomechanics. *Phys. Rev. A*, 88:063850, 2013.

[128] Ying-Dan Wang and Aashish A. Clerk. Reservoir-engineered entanglement in optomechanical systems. *Phys. Rev. Lett.*, 110:253601, 2013.

[129] Huatang Tan, Gaoxiang Li, and P. Meystre. Dissipation-driven two-mode mechanical squeezed states in optomechanical systems. *Phys. Rev. A*, 87:033829, 2013.

[130] Jing Zhang, Kunchi Peng, and Samuel L. Braunstein. Quantum-state transfer from light to macroscopic oscillators. *Phys. Rev. A*, 68:013808, 2003.

[131] M. Pinard, A. Dantan, D. Vitali, O. Arcizet, T. Briant, and A. Heidmann. Entangling movable mirrors in a double-cavity system. *EPL (Europhysics Letters)*, 72(5):747, 2005.

[132] M. Abdi, S. Pirandola, P. Tombesi, and D. Vitali. Entanglement swapping with local certification: Application to remote micromechanical resonators. *Phys. Rev. Lett.*, 109:143601, 2012.

[133] L Tian, M S Allman, and R W Simmonds. Parametric coupling between macroscopic quantum resonators. *New Journal of Physics*, 10(11):115001, 2008.

[134] Fernando Galve, Leonardo A. Pachón, and David Zueco. Bringing entanglement to the high temperature limit. *Phys. Rev. Lett.*, 105, 2010.

[135] M. P. Blencowe and M. N. Wybourne. Quantum squeezing of mechanical motion for micron-sized cantilevers. *Physica*, 280:555–556, 2000.

[136] A. Heidmann, R. J. Horowicz, S. Reynaud, E. Giacobino, C. Fabre, and G. Camy. Observation of quantum noise reduction on twin laser beams. *Phys. Rev. Lett.*, 59:2555–2557, 1987.

[137] M. R. Vanner, I. Pikovski, G. D. Cole, M. S. Kim, Č. Brukner, K. Hammerer, G. J. Milburn, and M. Aspelmeyer. Pulsed quantum optomechanics. *Proc. Nat. Acad. Sci. USA*, 108:16182–16187, 2011.

[138] Mankei Tsang and Carlton M. Caves. Evading quantum mechanics: Engineering a classical subsystem within a quantum environment. *Phys. Rev. X*, 2:031016, 2012.

[139] GM D'Ariano, Matteo GA Paris, and Massimiliano F Sacchi. Quantum tomography. *Advances in Imaging and Electron Physics*, 128:206–309, 2003.

[140] K. Vogel and H. Risken. Determination of quasiprobability distributions in terms of probability distributions for the rotated quadrature phase. *Phys. Rev. A*, 40:2847–2849, 1989.

[141] Sze M. Tan. An inverse problem approach to optical homodyne tomography. *Journal of Modern Optics*, 44(11-12):2233–2259, 1997.

[142] Swati Singh and Pierre Meystre. Atomic probe wigner tomography of a nanomechanical system. *Phys. Rev. A*, 81:041804, 2010.

[143] D. Leibfried, R. Blatt, C. Monroe, and D. Wineland. Quantum dynamics of single trapped ions. *Rev. Mod. Phys.*, 75:281–324, 2003.

[144] O. Romero-Isart, A. C. Pflanzer, M. L. Juan, R. Quidant, N. Kiesel, M. Aspelmeyer, and J. I. Cirac. Optically levitating dielectrics in the quantum regime: Theory and protocols. *Phys. Rev. A*, 83:013803, 2011.

[145] H M Wiseman. Quantum trajectories and quantum measurement theory. *Quantum and Semiclassical Optics: Journal of the European Optical Society Part B*, 8(1):205, 1996.

[146] Jean Dalibard, Yvan Castin, and Klaus Mølmer. Wave-function approach to dissipative processes in quantum optics. *Phys. Rev. Lett.*, 68:580–583, 1992.

[147] K. Jacobs and P. L. Knight. Linear quantum trajectories: Applications to continuous projection measurements. *Phys. Rev. A*, 57:2301–2310, 1998.

[148] Peter Goetsch, Robert Graham, and Fritz Haake. Microscopic foundation of a finite-temperature stochastic schrödinger equation. *Quantum and Semiclassical Optics: Journal of the European Optical Society Part B*, 8(1):157, 1996.

[149] Peter Goetsch and Robert Graham. Linear stochastic wave equations for continuously measured quantum systems. *Phys. Rev. A*, 50:5242–5255, 1994.

[150] Jay Gambetta and H M Wiseman. Stochastic simulations of conditional states of partially observed systems, quantum and classical. *Journal of Optics B: Quantum and Semiclassical Optics*, 7(10):S250, 2005.

[151] Jr. T. Dankel. On the distribution of the integrated square of the ornstein–uhlenbeck process. *SIAM Journal on Applied Mathematics*, 51(2):568–574, 1991.

[152] Jeremy Stein and Elias Stein. Stock price distributions with stochastic volatility: An analytic approach. *Review of Financial Studies*, 4:727–752, 1991.

[153] Sze M Tan. A computational toolbox for quantum and atomic optics. *Journal of Optics B: Quantum and Semiclassical Optics*, 1(4):424, 1999.

[154] J. K. Breslin and G. J. Milburn. Conditional variance reduction by measurements on correlated field modes. *Phys. Rev. A*, 55:1430–1436, 1997.

[155] H. J. R. Westra, M. Poot, H. S. J. van der Zant, and W. J. Venstra. Nonlinear modal interactions in clamped-clamped mechanical resonators. *Phys. Rev. Lett.*, 105:117205, 2010.

[156] I. Mahboob, K. Nishiguchi, A. Fujiwara, and H. Yamaguchi. Phonon lasing in an electromechanical resonator. *Phys. Rev. Lett.*, 110:127202, 2013.

[157] Nicolai B. Grosse, Warwick P. Bowen, Kirk McKenzie, and Ping Koy Lam. Harmonic entanglement with second-order nonlinearity. *Phys. Rev. Lett.*, 96:063601, 2006.

Appendix A

Derivation of conditional squeezing angle

With the steady-state and $C = 0$ conditions, the quadratic equations (4.45-4.46) can be expressed as

$$2\eta\mu V_{Y\alpha}^2 + (\gamma - \chi\sin(2\alpha_1))V_{Y\alpha} = 2\eta\mu V_{X\alpha}^2 + (\gamma + \chi\sin(2\alpha_1))V_{X\alpha} = \gamma V_T \ . \tag{A.1}$$

Rearranging the first equality and using Eq. (4.50) gives a new equation for the antisqueezing angle

$$2\eta\mu(V_{X\alpha} + V_{Y\alpha}) = \Delta\tan(2\alpha_1) - \gamma \ , \tag{A.2}$$

which as expected, reduces to the unconditional result Eq. (4.38) when $\eta\mu = 0$. We would like a form in terms of system parameters only, for which we can rearrange Eq. (A.1) again to remove α_1, leaving a relation between the two quadratures

$$4V_{Y\alpha}V_{X\alpha}\left(\eta\mu + \frac{\gamma}{V_{Y\alpha} + V_{X\alpha}}\right) = \gamma V_T \ . \tag{A.3}$$

Using Eqs (4.50), (A.2) and (A.3), we can obtain an expression containing only a function of α_1, the thermal variance V_T and other parameters. The general form of α_1 is now the solution to the equation

$$\left(\Delta^2\tan^2(2\alpha_1) - \gamma^2\right)\left(1 - \frac{\chi^2}{\Delta^2}\cos^2(2\alpha_1)\right) = 8\eta\mu\gamma V_T \ , \tag{A.4}$$

or written in terms of SNR,

$$\Delta^2\tan^2(2\alpha_1) - \chi^2\sin^2(2\alpha_1) + \frac{\chi^2\gamma^2}{\Delta^2}\cos^2(2\alpha_1) = \gamma^2(1 + 4\mathrm{SNR}) \ . \tag{A.5}$$

From examining the above, we see that the antisqueezing angle increases from the unconditional angle α_0 at $\mathrm{SNR} = 0$ up to $\pi/4$ in the limit $\mathrm{SNR} \gg 1$. We can solve analytically by multiplying through by $\cos^2(2\alpha_1)$ and transforming sine to cosine, then solving a quadratic equation, resulting in

$$\cos 2\alpha_1 = \frac{\Delta}{\chi_{th}}\left(\frac{\chi_{th}^2 + \chi^2 + 4\gamma^2\mathrm{SNR} - \sqrt{(\chi_{th}^2 - \chi^2)^2 + 8(\chi_{th}^2 + \chi^2)\gamma^2\mathrm{SNR} + 16\gamma^4\mathrm{SNR}^2}}{2\chi^2}\right)^{\frac{1}{2}} \tag{A.6}$$

Appendix B

Post-processing of steady-state measurements

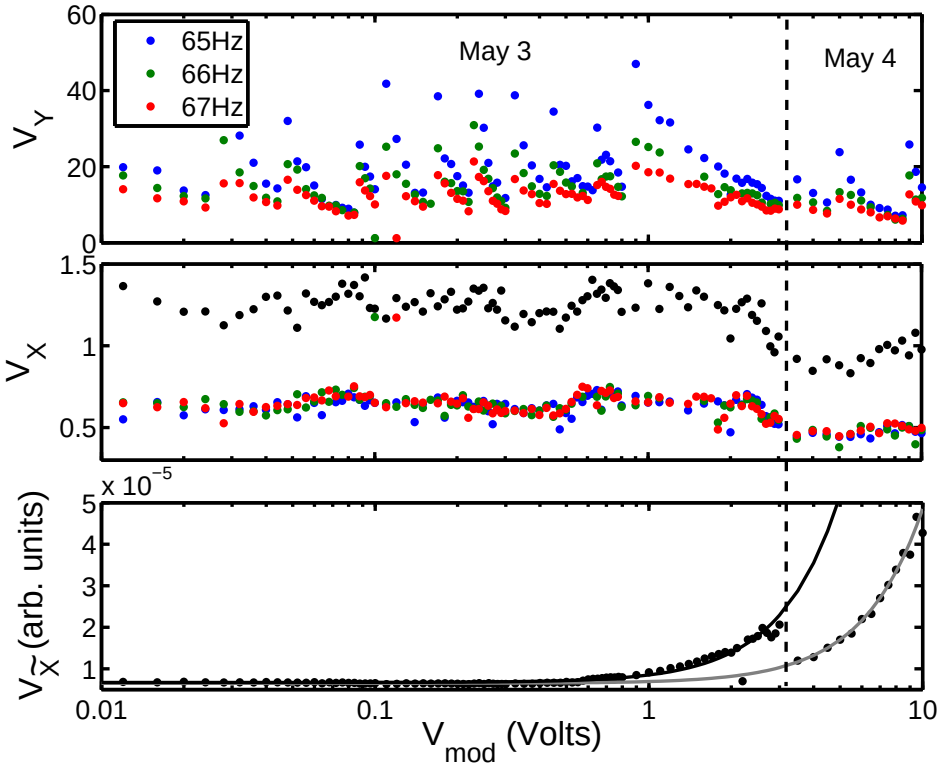

Figure B.1: Unconditional variances of steady-state data with increasing SNR of the low-fidelity measurement. Black circles indicate data taken with the parametric drive off, while different coloured circles indicate a different nominally detuned drive. The top panel is the variance of the maximally amplified quadrature, while the middle panel contains the undriven and maximally squeezed variances. The bottom panel is the undriven variance of the low-fidelity data, with solid lines used to fit the SNR to the square of the modulation voltage.

Figure B.1 shows the unconditional variances of the data (that is, the variances of the

unfiltered data) taken during the steady-state measurements. At each SNR of the low-fidelity measurement, the lock-in outputs are recorded once in the absence of driving, and three times with the parametric drive on, with detunings 1Hz apart. Multiple detunings were used to account for frequency drift away from threshold during the measurements. The DC voltage was tuned periodically to bring the cantilever frequency back towards threshold, as can be seen in Fig. B.1. While the detunings in the figure are clearly only nominal, the real detuning could be inferred from the convolution frequency Ω in the previous undriven case. Detunings nearest to a frequency of $\Delta = 63$Hz were then chosen, corresponding to an amplified variance of $10.5V_T$. The shaded bands in Figure 5.11 reflect the resulting uncertainty in detuning.

The SNR could be determined from the variance of the low-fidelity lock-in measurements. Monotonicity was preserved by fitting this variance as $V_{\tilde{X}} = \beta V_{\mathrm{mod}}^2 + V_{\mathrm{shot}}$, where V_{mod} was the peak-to-peak modulation voltage used to produce the sideband. Two fits were used to account for the re-locking and realignment after the relative fibre position and hence reflected optical power drifted overnight.

Each set of four time traces from the lock-in amplifier outputs was processed in the following way.

1. Import datasets and adjust scales to correspond to mV.

2. In the undriven case, rotate the low-fidelity quadratures to maximise the correlation with the high-fidelity quadratures. In the driven case, rotate each set of quadratures to maximise the Y quadrature variance.

3. Calculate filter parameter estimates based on the undriven SNR $= \mathrm{Var}(\tilde{X})/V_{\mathrm{shot}} - 1$ and estimated drive parameters, using the results of Section 4.8.

4. Divide each time series into 21 windows of 1500 points.

5. For each adjacent pair of windows, run MATLAB optimisation function `fminsearch` to minimise the residual variance over the second window. The estimate is calculated by convolving the signal (two window lengths) with the filter function truncated to one window length. In the driven case, the variance is optimised over $g_1, g_2, \Gamma, \Omega, \psi, \alpha$, where α is a quadrature rotation angle and the other parameters are defined in Eq. (5.11). In the undriven case, the same filter is used, with the restrictions $\phi = 0$ and $g_1 = g_2$. All parameters except g_i are constrained to a finite range using sigmoid functions.

6. If `fminsearch` converges for at least one pair of windows, average the parameters obtained over all converged window pairs.

7. Repeat step 5 for the entire waveforms to calculate the conditional variance

8. If the optimisation over the entire waveforms converged, repeat step 5 for the Y quadrature, keeping α fixed.

The resulting conditional variances, using the detuning closest to 63Hz for each SNR, are shown in Figures 5.10 and 5.11, in good agreement with theory, as are the optimised filter parameters shown in Figure 5.12.

Appendix C

Effective QND measurement

C.1 Derivation of effective measurement strength and purity

The general solution for the conditional variances $V_{X\alpha}, V_{Y\alpha}$ when the quadrature phase space is optimally rotated is given in Section 4.7. We can use these solutions, including the squeezing angle α to re-obtain V_X and C, and thus calculate g.

$$V_X = \frac{1}{2}(V_{Y\alpha} + V_{X\alpha}) - \frac{1}{2}(V_{Y\alpha} - V_{X\alpha})\cos(2\alpha) \tag{C.1}$$

$$V_Y = \frac{1}{2}(V_{Y\alpha} + V_{X\alpha}) + \frac{1}{2}(V_{Y\alpha} - V_{X\alpha})\cos(2\alpha) \tag{C.2}$$

$$C = \frac{1}{2}(V_{Y\alpha} - V_{X\alpha})\sin(2\alpha) \tag{C.3}$$

Substituting $\Delta = \chi$ into Eq. (4.50) so that

$$V_{Y\alpha} + V_{X\alpha} = \frac{V_{Y\alpha} - V_{X\alpha}}{\cos(2\alpha)} \tag{C.4}$$

we end up, via simple trigonometry, with

$$g = \frac{C}{V_X} = \cot(2\alpha) \tag{C.5}$$

so

$$\frac{\mu_{\text{eff}}}{\mu} = 1 + g^2 = \frac{1}{\sin^2(2\alpha)} \tag{C.6}$$

An explicit general solution for $\cos(2\alpha)$ is given by Eq. (4.51). The effective measurement strength is then easily derived as

$$\frac{\mu_{\text{eff}}}{\mu} = \frac{2(1+\chi'^2)}{1 + \sqrt{(1+4\text{SNR})^2 + 16\chi'^2\text{SNR}} - 4\text{SNR}} \tag{C.7}$$

where $\chi' = \chi/\gamma$ is the normalised parametric drive strength and $\text{SNR} = \eta\mu(2N + 2N_{BA} + 1)/\gamma$ defines the signal-to-noise ratio for the thermal noise.

Equation (C.5) can also be used to find a simple expression for the state purity. Substituting this into Eq. (A.2) with $\Delta = \chi$ gives

$$2\eta\mu(V_{X\alpha} + V_{Y\alpha}) = \chi/g - \gamma \,, \tag{C.8}$$

Now substituting this into Eq. (A.3) and rearranging produces

$$\frac{1}{4V_{X\alpha}V_{Y\alpha}} = \frac{\eta}{1+\gamma(2N+1)/\mu}\left(1 + \frac{2}{\chi'/g - 1}\right) \,. \tag{C.9}$$

The left hand side of the above equation is equal to the purity, since by definition the covariance of the optimal quadratures X_α and Y_α is zero.

C.2 Effective filter width

The relevant timescale of a measurement can be illustrated by the filter parameters — specifically, the filter width — that produce the optimal position estimates from the noisy time-series measurements. These parameters are found by Fourier transforming and solving the conditional equations of motion, then transforming back to the time domain. The exponential decay that specifies the filter width contains the rate

$$\Gamma = \gamma + 2\eta\mu(V_X + V_Y) \tag{C.10}$$

This sum of variances is identical to that for the optimal quadratures (see Eqs (C.1-C.2)) and so Eq. (C.8) can be used to give

$$\frac{\Gamma}{\gamma} = \frac{\chi'}{g} \tag{C.11}$$

The filter width then blows up as g deviates from χ' and approaches 0. This effect exactly coincides with the enhancement factor μ_{eff}/μ dropping from $1 + \chi'^2$ back to 1, and the amplification becoming redundant. After some algebra, the filter width can be rewritten in terms of experimental parameters as

$$\frac{\Gamma}{\gamma} = \sqrt{(1 + 4\text{SNR} + \sqrt{(1+4\text{SNR})^2 + 16\chi'^2\text{SNR}})/2} \tag{C.12}$$

We can see that when $\chi' = 0$, the standard expression is recovered

$$\frac{\Gamma}{\gamma} = \sqrt{1 + 4\text{SNR}} \tag{C.13}$$

If instead, we let it be non-zero but restrict ourselves to the ultraweak measurement case in which the amplified peak is still obscured under the measurement noise ($\text{SNR}(1+\chi'^2) \ll 1$ where $\chi' \gg 1$), we can expand the inner square root to give

$$\frac{\Gamma}{\gamma} \approx \sqrt{1 + 4\text{SNR}(1+\chi'^2)} \tag{C.14}$$

which has exactly the same form, but with SNR effectively enhanced by the amplification factor. However, as this approximation breaks down, the filter widens more slowly as a function of this enhanced SNR. In the opposite limit $\mathrm{SNR}(1+\chi'^2) \gg 1$, we obtain

$$\frac{\Gamma}{\gamma} \approx \sqrt[4]{\chi'^2 \mathrm{SNR}} \tag{C.15}$$

This is due to the fact that the unconditional Y spectrum only contains a filtered version of the X spectrum (as given by Eq. (4.21)), and hence contains the most accurate X information within a narrow band around the peak. As this peak rises above the noise floor, the measurement fidelity does not scale in the same way as for a direct, high-fidelity measurement of the X quadrature.